



**Republic of Iraq  
Ministry of Higher  
Education  
and Scientific Research  
University of Diyala  
College of Science  
Department of Physics**



# **Influence of Nanostructured Films Deposition on the Protection of High Temperature Metallic Corrosion**

A thesis

Submitted to the Council of the College of Science  
University of Diyala in Partial Fulfillment of Requirements  
for the Degree of Doctor of Philosophy in Physics Sciences

By

**Adnan Ali Muhammad**

B.Sc. 1993

M.Sc. 2016

Supervised By

**Prof. Dr.  
Ziad T. Khodair**

**Prof. Dr.  
Anees A. Khadom**

2020 A.D.

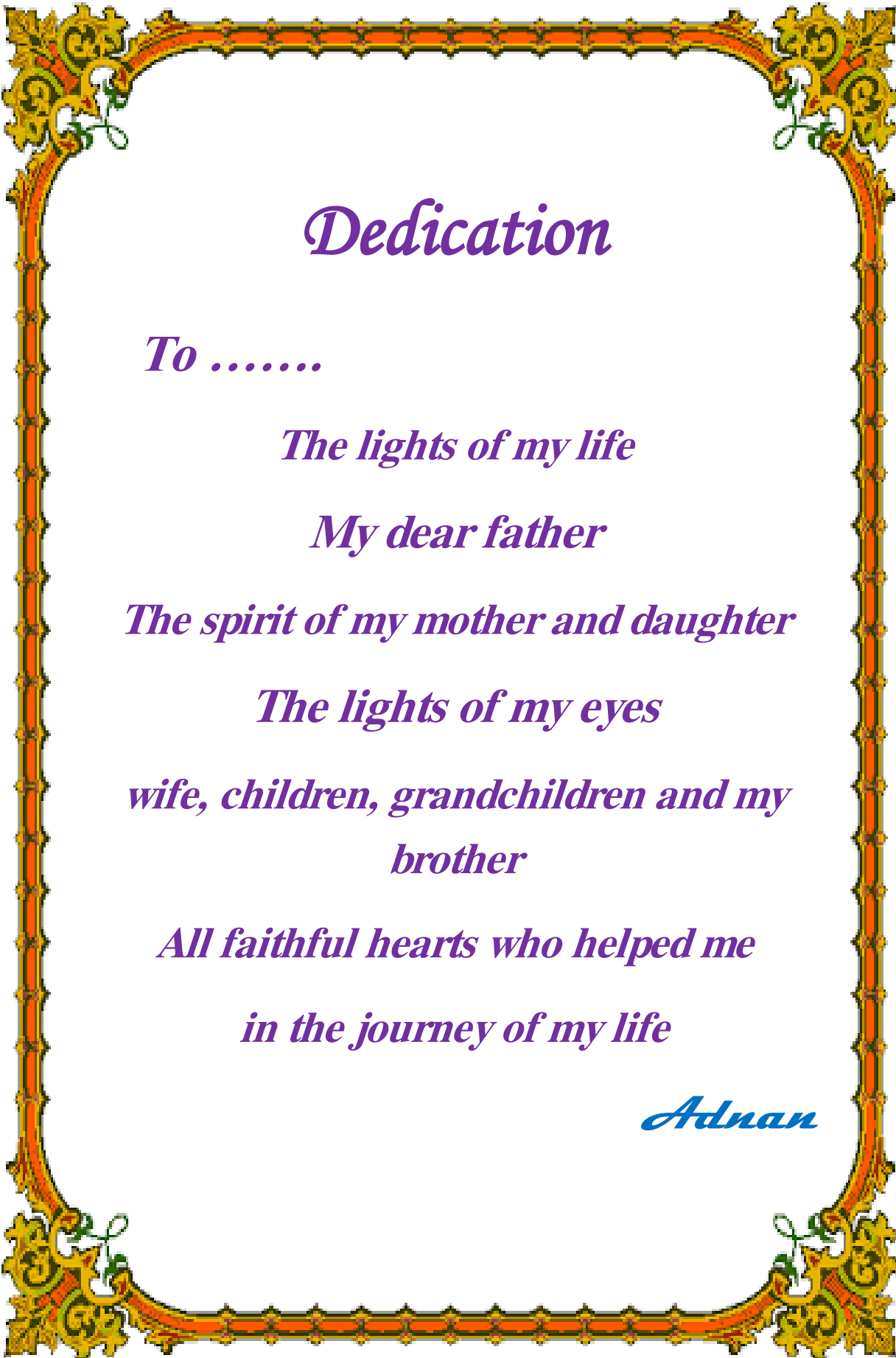
1442 A.H.

بِسْمِ اللّٰهِ الرَّحْمٰنِ الرَّحِیْمِ

وَسْأَلُونَكَ عَنِ الرُّوحِ قُلِ الرُّوحُ مِنْ أَمْرِ رَبِّي وَمَا أُوتِيتُمْ مِّنَ

الْعِلْمِ إِلَّا قَلِيلًا ۝٨٥

صَدَقَ اللّٰهُ الْعَظِیْمُ  
سورة الاسراء



# *Dedication*

*To .....*

*The lights of my life*

*My dear father*

*The spirit of my mother and daughter*

*The lights of my eyes*

*wife, children, grandchildren and my  
brother*

*All faithful hearts who helped me*

*in the journey of my life*

*Adnan*

## Acknowledgement

First of I would like to offer the bulk of thanks and gratitude to the Almighty *Allah*, whose Grace enabled me to continue this work and overcome all difficulties and our prophet *Muhammad* (peace and blessings of Allah be upon him) who invites us to science and knowledge.

I would like to express my sincere appreciation and deep gratitude to my supervisors, **Prof. Dr. Ziad T. Khodair** and **Prof. Dr. Anees A. Khadom** for suggesting the topic of this thesis, guidance, suggestions and continuous encouragement throughout the research work.

Special thanks are extended to the University of Diyala, College of Science, specially the dean of College of Science, **Prof. Dr. Tahseen H. Mubarak** for his kind cooperation and constant support.

I would like to express my deep gratitude to **Prof. Dr. Nabeel Ali Bakr** and **Prof. Dr. Sabah Anwer Salman** and all my professors for their generous cooperation, encouragement and continued support throughout the period of Doctor's study in the Department of Physics, College of Sciences, Diyala University.

I would like to express my deep gratitude to the Dean of the College of Engineering, University of Diyala, as well as to the head of the Chemical Engineering Department for their assistance in completing the

practical experiments. Also, my thanks and appreciation to (**Engineer Mohannad**), the Chemical Engineering Department Laboratory Officer, for helping me throughout my lab life.

I am also very indebted to (**Prof. Dr. Adel K. Mahmoud**), The Head of the Department of Materials Engineering - College of Engineering - Diyala University for his continuous encouragement and providing scientific advice to me.

I would also like to thank the staff of the Library of College of Science (Adnan and Raafat), who continued to provide excellent service, tireless support and scientific resources to all students.

I do not forget to thank **Assist. Prof Ali Asjodi** (Energy and Materials Research Center, Tehran- Iran), to help me to coat the samples.

My greatest indebtedness goes to my **Father, Wife, Children, my brother and all my cousins** for their valuable advice, and to my Friends (**Muhammad Nayef, Hussein, Raad, Muhammad Ihsan, Shaimaa, Ahmed Shano and Sufian**) for their endless support.

Finally, my special thanks to my friends (**Mr. Ismail Q. Mari, Mr. Hamza M. Kalash and the assistant lecturer Wathiq A. Khalifa**) for their encouragement throughout my studies.

*Adnan*

2020

## Scientific Amendment

I certify that the thesis entitled "**Influence of Nanostructured Films Deposition on the Protection of High Temperature Metallic Corrosion**" presented by (**Adnan Ali Mohammed**) has been evaluated scientifically, therefore, it is suitable for debate by examining committee.



Signature:

**Name: : Dr. Mustafa Ahmed Rajab**

Degree: Assistant Professor

Address: Technical Institute of Baqubah

Middle Technical University

Date: / / 2020

## Linguistic Amendment

I certify that the thesis entitled "**Influence of Nanostructured Films Deposition on the Protection of High Temperature Metallic Corrosion**" presented by (**Adnan Ali Mohammed**)" has been corrected linguistically, therefore, it is suitable for debate by examining committee.

Signature:



**Name: : Dr. Laith Abdul Latif Majeed**

Degree: Assistant Professor

Address: College of Science

University of Diyala

Date: / / 2020

## Scientific Amendment

I certify that the thesis entitled "**Influence of Nanostructured Films Deposition on the Protection of High Temperature Metallic Corrosion**" presented by (**Adnan Ali Mohammed**) has been evaluated scientifically, therefore, it is suitable for debate by examining committee.



Signature:

**Name: : Dr. Mustafa Ahmed Rajab**

Degree: Assistant Professor

Address: Technical Institute of Baqubah

Middle Technical University

Date: / / 2020

## Examination Committee Certification

We certify that we have read this thesis, entitled "**Influence of Nanostructured Films Deposition on the Protection of High Temperature Metallic Corrosion**" and, as an examining committee, we examined the student (**Adnan Ali Mohammed**) on its content, and in what is related to it, and that in our opinion it meets the standard of a thesis for the Degree of **Doctor of Philosophy (Ph.D.) in Physics Sciences**.

Signature: N.A. Bakr  
Name: **Prof. Dr. Nabeel A. Bakr**  
Address: University of Diyala  
Date: / / 2020  
**Chairman**

Signature: Ahseen  
Name: **Prof. Dr. Tahseen H. Mubarak**  
Address: University of Diyala  
Date: / / 2020  
**Member**

Signature: Nidhal  
Name: **Prof. Dr. Nidhal N. Jandow**  
Address: Al-Mustansiriyah University  
Date: / / 2020  
**Member**

Signature: Shihab  
Name: **Prof. Dr. Shihab A. Zaidan**  
University of Technology  
Date: 2 / 11 / 2020  
**Member**

Signature: Abdulameed  
Name: **Assist. Prof. Dr. Abdulameed R. Mahdi**  
University of Baghdad  
Date: / / 2020  
**Member**

Signature: Ziad  
Name: **Prof. Dr. Ziad T. Khodair**  
University of Diyala  
Date: / / 11 / 2020  
**Supervisor**

Signature: Anees  
Name: **Prof. Dr. Anees A. Khadom**  
University of Diyala  
Date: / / 2020  
**Supervisor**

Approved by the Council of the College of Science  
(The Dean)

Signature: Ahseen  
Name: **Prof. Dr. Tahseen H. Mubarak**  
Date: / / 2020

## Published Research Articles

1. Adnan A. Mohammed, Ziad T. Khodair , Anees A. Khadom, " Preparation, Characterization and Application of Al<sub>2</sub>O<sub>3</sub> Nanoparticles for the Protection of Boiler Steel Tubes from High Temperature Corrosion", *Ceramics International*, Vol. 46, pp. 26945–269552, 2020
2. Adnan A. Mohammed, Ziad T. Khodair , Anees A. Khadom, "Preparation and investigation of the structural properties of  $\alpha$ -Al<sub>2</sub>O<sub>3</sub> nanoparticles using the Sol-Gel method", *Chemical Data Collections*, Vol. 29, pp.1-8, 2020,

## Abstract

In this study,  $\alpha$ -Al<sub>2</sub>O<sub>3</sub> nanoparticles were successfully prepared at room temperature using Sol-Gel method. X-Ray Diffraction (XRD) of the nanoparticles that were prepared showed that they had a polycrystalline structure. The average crystallite size of the nanoparticles was estimated by Scherrer's method and Williamson Hall analysis, and it was observed that its magnitude was (33.9 and 27.7 nm), respectively. Field Emission Scanning Electron Microscopy (FESEM) images of the prepared nanoparticles showed that the grains had heterogeneous sizes, irregular shapes, spherical and semi-spherical shapes, and the FESEM images showed that the average grain size of  $\alpha$ -Al<sub>2</sub>O<sub>3</sub> was approximately (29 nm).

Transmission electron microscopy (TEM) images of the  $\alpha$ -Al<sub>2</sub>O<sub>3</sub> prepared nanoparticles after granulation agglomerate, and the shape of the particles within the agglomerations is almost spherical, and the prepared granules are within the nanoscale.

Low carbon steel samples are coated with two layers, NiCrAlY powder as the bonding layer and the upper layer is the  $\alpha$ -Al<sub>2</sub>O<sub>3</sub> nanoparticles, using plasma spray technique. FESEM images of the coated sample surface showed it was homogeneous and does not contain voids or cracks. This proves that the plasma spray coating has high coating quality. It is shown that the thickness of the binding layer is about (100 ± 10 μm), while the thickness of the top layer was about (37 ± 5 μm).

The uncoated and coated low carbon steel samples were studied and analyzed after being tested at temperatures (600, 700, 800 and 900 °C) at constant time period of (20 hours) at the absence and presence of corrosion medium consisting of (57wt% V<sub>2</sub>O<sub>5</sub> and 43 wt% Na<sub>2</sub>SO<sub>4</sub>).

XRD diffraction patterns for coated samples without ash after the oxidation test showed that there are no diffraction peaks other than the peaks of the elements (O) and (Al). But in the case of ash there were new peaks of other compounds such as vanadium compounds.

FESEM for the coated samples without ash showed that there was no effect of temperature on the surface of the samples and that no cracks or corrosion were observed in the coating layer. This is consistent with the photographs of the samples after the test, where the color of the samples is unchanged neither in the case of the coated samples nor in the presence of ash. FESEM reported images show a significant effect on the surface of the samples due to the interaction of the ash compounds with the aluminum nanoparticles at high temperatures, as cracks and pores were observed due to the melting of the ash components and their interaction with the coating layer.

FESEM cross-section images of samples after coating in the presence of ash at (600 and 900 °C) also showed the presence of cracks between the bonding layer and the substrate.

Hot corrosion results showed that the corrosion rate increased with increasing temperature and fuel ash. Where it was found that the lowest corrosion rate is for uncoated samples and without ash, and the highest corrosion rate is for uncoated samples was the presence of ash. The efficiency of the coating was studied for samples coated with and without ash, as it was between (44-84%) for samples coated without ash. As for the samples coated with ash, the efficiency ranges were between (84-88%). The activation energy of the samples was also calculated. It has high values without coating, and activation energy decreased in the presence of ash. As for coated samples, the activation energy was high for samples without ash and decreased with ash.

## List of Contents

Item no.	Subjects	Page no.
<b>Chapter One</b> <b>Introduction and Basic Concepts</b>		
1.1	Introduction	1
1.2	Classification of Corrosion	2
1.2.1	Corrosion dependent on the nature of the reaction	2
1.2.2	Corrosion dependent on the nature of the medium	2
1.2.3	Corrosion dependent on the shape and area of the corrosion region	3
1.3	Hot Corrosion	5
1.4	Thermal Barrier Coatings (TBCs)	6
1.5	Thermal Spray Methods	7
1.5.1	Flame Spraying	8
1.5.2	High Velocity Oxy-fuel Spraying (HVOF)	8
1.5.3	Wire Arc Spraying	8
1.5.4	Vacuum Plasma Spraying (VPS).	8
1.5.5	Air Plasma Spraying (APS)	9
1.6	Nanomaterials	9
1.6.1	Classification of Nanomaterials	10
1.6.2	Synthesis of Nanomaterial	11
1.7	Sol-Gel Method	12

1.7.1	Applications of the Sol-Gel	13
1.7.2	Advantages of Sol-Gel Method	13
1.7.3	Disadvantages of Sol-Gel Method	14
1.8	Low carbon steel	14
1.9	Aluminum Oxide ( $Al_2O_3$ )	16
1.9.1	Aluminum oxide ceramic applications.	17
1.10	Nickel Chromium Aluminum Yttrium alloy	18
1.10.1	Applications of NiCrAlY alloy	19
1.11	Previous Studies.	19
1.12	Objectives of the study	27
<b>Chapter Two</b>		
<b>Theoretical Background</b>		
2.1	Introduction	28
2.2	Mechanism of Hot Corrosion	28
2.3	Deposition Mechanisms	30
2.4	Thermal Barrier Coatings and Thermal Grown Oxide	32
2.5	Basic conditions for the coating layer	34
2.5.1	Corrosion Resistance	34
2.5.2	Erosion Resistance	34
2.5.3	Thermal Stability	35
2.5.4	Mechanical Toughness	35
2.5.5	Adhesion	35
2.6	The Forming Mechanism of Thermal Spray Coatings	36

2.7	Preparation methods and roughing the substrate surface	38
2.7.1	Grit Blasted Method	49
2.7.2	Rough Threading	40
2.7.3	Groove Method	40
2.7.4	Arc Methods of Preparation	40
2-8	Structure Properties	41
2.9	Structural Parameters	42
2.9.1	Lattice constants ( $a_0$ , $b_0$ , $c_0$ ) of hexagonal structure	42
2.9.2	Crystallite average size ( $D_{av}$ )	42
2.9.3	Dislocation density	43
2.9.4	Texture Coefficient (TC)	44
2.9.5	Specific Surface Area (SSA)	44
2.9.6	Factors affecting X-ray diffraction	45
2.10	Mechanical properties	46
2.10.1	Surface Hardness Test	46
2.10.2	Vickers Hardness Test	47
2.11	Corrosion Rate	49
2.11.1	A Method of Weight Loss	49
2.11.2	Coating Efficiency (% IE)	49
2.11.3	Activation Energy	50
2.12	Field Emission Scanning Electron Microscope (FESEM)	51
2.13	Transmission electron microscopy (TEM)	53

2.14	Energy Dispersive Spectroscopy (EDS)	54
<b>Chapter Three Experimental Work</b>		
3.1	Introduction	55
3.2	Chemicals and Raw Materials	55
3.3	Preparation of $\alpha$ -Aluminum Oxide Nanoparticles	55
3.3.1	Preparation of the solution	58
3.3.2	Drying stage	58
3.3.3	The Annealing Stage and the Calcination	59
3.4	Coating process of samples	59
3.4.1	Preparation of low carbon steel samples	60
3.4.2	Granulation of Alumina Nanoparticles	62
3.4.3	Coating samples	61
3.5	Plasma spray device	61
3.5.1	Plasma Torch	64
3.5.2	Powder Feeder	65
3.5.3	Control Unit	65
3.5.4	Cooling Water System	65
3.6	High Temperature Corrosion Test	66
3.6.1	Ash preparation	66
3.6.2	Preparation of the pickling solution	66
3.6.3	Oxidation Test For Samples Without Ash	67
3.6.4	Oxidation Test For Samples With Ash	67

3.7	Characterizations Techniques	67
3.7.1	Structural Measurements	67
3.7.2	Transmission Electron Microscopy (TEM)	68
3.7.3	Field Emission Scanning Electron Microscopy (FESEM)	68
3.8	Hardness Test	69
3.9	Corrosion Measurements	69
<b>Chapter Four Results and Discussion</b>		
4.1	Introduction	70
4.2	Structural Properties of the $\alpha$ -Al <sub>2</sub> O <sub>3</sub> prepared by Sol-Gel method	70
4.2.1	XRD Analysis of $\alpha$ -Al <sub>2</sub> O <sub>3</sub> nanoparticles	70
4.2.2	Calculation of interplanar spacing ( $d_{hkl}$ )	72
4.2.3	The lattice constants ( $a_o, c_o$ )	72
4.2.4	The crystallite size ( $D_{av}$ )	72
4.2.5	Dislocation Density ( $\delta$ )	75
4.2.6	Texture coefficient $T_c (hkl)$	75
4.2.7	Specific Surface Area (SSA)	75
4.3	Morphological analysis of the $\alpha$ -Al <sub>2</sub> O <sub>3</sub> prepared by Sol-Gel method	77
4.3.1	FESEM Analysis of the $\alpha$ -Al <sub>2</sub> O <sub>3</sub> nanoparticles	77
4.3.2	Analysis element (EDS) of the $\alpha$ -Al <sub>2</sub> O <sub>3</sub> nanoparticles.	78
4.3.3	TEM analysis of the $\alpha$ -Al <sub>2</sub> O <sub>3</sub> nanoparticles	79
4.4	Analysis of NiCrAlY Powder	79
4.4.1	XRD Analysis of NiCrAlY Powder	79

4.4.2	FESEM of the NiCrAlY Powder.	80
4.5	Analysis of results of low carbon steel samples before coating and testing process	81
4.5.1	XRD Analysis of low carbon steel samples	81
4.5.2	FESEM of low carbon steel samples before coating and testing	81
4.5.3	Analysis element (EDS) of low carbon steel samples surface before coating and testing	82
4.6	Analysis the results of samples after coating and before testing	83
4.6.1	XRD analysis the results of samples after coating and before testing	84
4.6.2	Calculation of interplanar spacing ( $d_{hkl}$ ) of the samples after coating and before testing	84
4.6.3	The crystallite size ( $D_{av}$ )	86
4.6.4	Dislocation Density ( $\delta$ )	86
4.6.5	Texture coefficient $T_{c(hkl)}$	86
4.6.6	Specific Surface Area (SSA)	87
4.6.7	FESEM of the samples after coating and before testing	87
4.6.8	EDS of the samples after coating and before testing	89
4.6.9	Vickers hardness for the surface of the samples before and after coating	90
4.7	Analysis the results of the samples after Oxidation test	90
4.7.1	FESEM and EDS of the samples without coating and without ash after oxidation test results	90
4.7.2	FESEM and EDS of the samples without coating and with ash after oxidation test results.	93
4.7.3	XRD of the samples with coating and without ash after oxidation test results	96
4.7.4	Calculation of interplanar spacing ( $d_{hkl}$ ) of the samples with coating and without ash after oxidation test results.	97

4.7.5	The crystallite size ( $D_{av}$ ) of the samples with coating and without ash after oxidation test results.	97
4.7.6	Dislocation Density ( $\delta$ )	98
4.7.7	Texture coefficient $T_{c(hkl)}$	98
4.7.8	Specific Surface Area (SSA)	98
4.7.9	FESEM of the samples with coating and without ash after oxidation test results	101
4.7.10	Analysis element (EDS) of the samples with coating and without ash after testing	103
4.7.11	XRD of the samples with coating and with ash after oxidation test results	104
4.7.12	FESEM and EDS of the samples with coating and with ash after oxidation test results.	106
4.8	Corrosion Measurements	110
4.8.1	Corrosion rate measurements	110
4.8.2	Coating Efficiency (% IEC)	111
4.8.3	Activation energy ( $E_a$ )	112
4.9	Conclusions	115
4.10	Future Work	116
	References	117

## List of Tables

No.	Title	Page No.
1.1	Chemical, Physical, and Mechanical properties of aluminum oxide	17
1.2	Some properties of NiCrAlY alloy	19
2.1	Low melting point for some vanadium and sodium compounds	29
3.1	Physical and chemical properties of the materials used in the present study	56
3.2	Chemical compositions of low carbon steel 304L	60
3.3	Parameters of plasma spraying	63
4.1	Some of the results obtained from X-ray diffraction and its comparison with the international card (00-010-0173).	74
4.2	Structural parameters of the $\alpha$ -Al <sub>2</sub> O <sub>3</sub> nanoparticles	76
4.3	Some of the results obtained from X-ray diffraction of the samples with coating and without ash before and after oxidation test	85
4.4	Vickers hardness for the surface of the samples before and after coating	89
4.5	Some parameters of the results obtained from X-ray diffraction of the samples with coating and without ash before and after oxidation test	99
4.6	Corrosion rate and coating efficiency data at different condition.	113
4.7	Activation energy at different conditions	114

## List of Figures

No.	Title	Page No.
1.1	Uniform Corrosion	3
1.2	Pitting Corrosion	4
1.3	Crevice Corrosion	5
1.4	Erosion Corrosion	5
1.5	The classification of thermal spraying operations	9
1.6	Classification of Nanomaterials	11
1.7	Top-down and bottom-up approach for synthesis of nanoparticles	12
1.8	Sol-Gel method	13
1.9	The unit cell of $\alpha$ -Al <sub>2</sub> O <sub>3</sub>	17
2.1	Deposition Rate of Particles in a Boiler Furnace	31
2.2	Scheme of TBC barrier coating construction layers and individual sub layers	33
2.3	Schematic illustration of the factors contributing to failure mechanisms of TBCs	34
2.4	Scheme for the formation of a thermal spray paint	36
2.5	Collision of the drop with the base	37
2.6	Shapes of drops upon impact	38
2.7	The effect of surface protrusions on tear flow rupture	39
2.8	The crystal levels of Bragg's Law	42
2.9	Schematic of Vickers hardness test method	48
2.10	Arrhenius plots	51
2.11	Images under the same conditions by, a: SEM, b: FESEM	52

3.1	Schematic diagram of the preparation of $\alpha$ -Al <sub>2</sub> O <sub>3</sub> nanoparticles	57
3.2	Schematic diagram of coating process and characterization techniques for samples	62
3.3	Image of the plasma spray device	63
3.4	Schematic Diagram of the Plasma Spray Process	64
4.1	X-ray diffraction patterns for $\alpha$ -Al <sub>2</sub> O <sub>3</sub> nanoparticles	71
4.2	ICDD card number (00-010-0173) of $\alpha$ -Al <sub>2</sub> O <sub>3</sub> nanoparticles	71
4.3	The W-H analysis of $\alpha$ -Al <sub>2</sub> O <sub>3</sub> nanoparticles	73
4.4	FESEM images of $\alpha$ -Al <sub>2</sub> O <sub>3</sub> nanoparticles	77
4.5	The average grain size FESEM image of $\alpha$ -Al <sub>2</sub> O <sub>3</sub>	78
4.6	EDS of the prepared $\alpha$ -Al <sub>2</sub> O <sub>3</sub> nanoparticles	78
4.7	TEM of the prepared $\alpha$ -Al <sub>2</sub> O <sub>3</sub> powder after granulation	89
4.8	X-ray diffraction patterns for NiCrAlY Powder	80
4.9	FESEM of NiCrAlY alloy powder	80
4.10	X-ray diffraction patterns for low carbon steel	81
4.11	FESEM of the low carbon steel samples surface before coating and testing	82
4.12	EDS of the low carbon steel samples surface before coating and testing	83
4.13	XRD for $\alpha$ -Al <sub>2</sub> O <sub>3</sub> nanoparticles and of the samples after coating and before testing	84
4.14	Cross section of the sample with coating before testing	88
4.15	FESEM of the sample with coating before testing	88
4.16	(EDS) of samples after coating and before testing	89
4.17	Images of samples before testing and after testing	91
4.18	FESEM images of the samples without coating and without ash after testing at 600 °C	92
4.19	FESEM images of the samples without coating and without ash after testing at 900 °C	92

4.20	(EDS) of samples before coating and after testing at (600°C) and (900°C).	93
4.21	FESEM images of the samples without coating and with ash after testing at 600 °C	94
4.22	FESEM images of the samples without coating and with ash after testing at 900 °C	95
4.23	EDS of the samples without coating and with Ash at (600 °C) and (b) (900 °C)	95
4.24	XRD patterns of $\alpha$ -Al <sub>2</sub> O <sub>3</sub> powder , of the sample with coating before testing and for samples with coating and without ash after	97
4.25	The W-H analysis of the samples surface with coating and without ash after testing	100
4.26	FESEM images of the samples with coating and without ash after testing at 600 °C	102
4.27	FESEM images of the samples with coating and without ash after testing at 700 °C	102
4.28	FESEM images of the samples with coating and without ash after testing at 800 °C	103
4.29	FESEM images of the samples with coating and without ash after testing at 900 °C	103
4.30	Cross-Section images of the samples after coating and testing and without ash at 600 °C and 900 °C	103
4.31	EDS of the samples with coating and without Ash after testing at 600 °C and 900 °C	104
4.32	XRD patterns of sample with coating before testing samples with coating in presence of fuel ash after testing at 600, and 700 °C	105
4.33	XRD patterns of sample with coating before testing samples with coating in presence of fuel ash after testing at 800, and 900 °C	106
4.34	FESEM images of the samples with coating and with ash after testing at 600 °C	107
4.35	FESEM images of the samples with coating and with ash after testing at 700 °C	107
4.36	FESEM images of the samples with coating and with ash after testing at 800 °C	108
4.37	FESEM images of the samples with coating and with ash after testing at 900 °C	108
4.38	FESEM cross section images of the samples with coating and with ash after testing at 600 °C and 900 °C	109

4.39	EDS of the samples with coating and with Ash after testing at 600 °C and 900 °C	110
4.40	Corrosion rate as a function of temperature	111
4.41	Coating Efficiency as a function of temperature	112
4.42	Arrhenius plots for oxidation of the samples	114

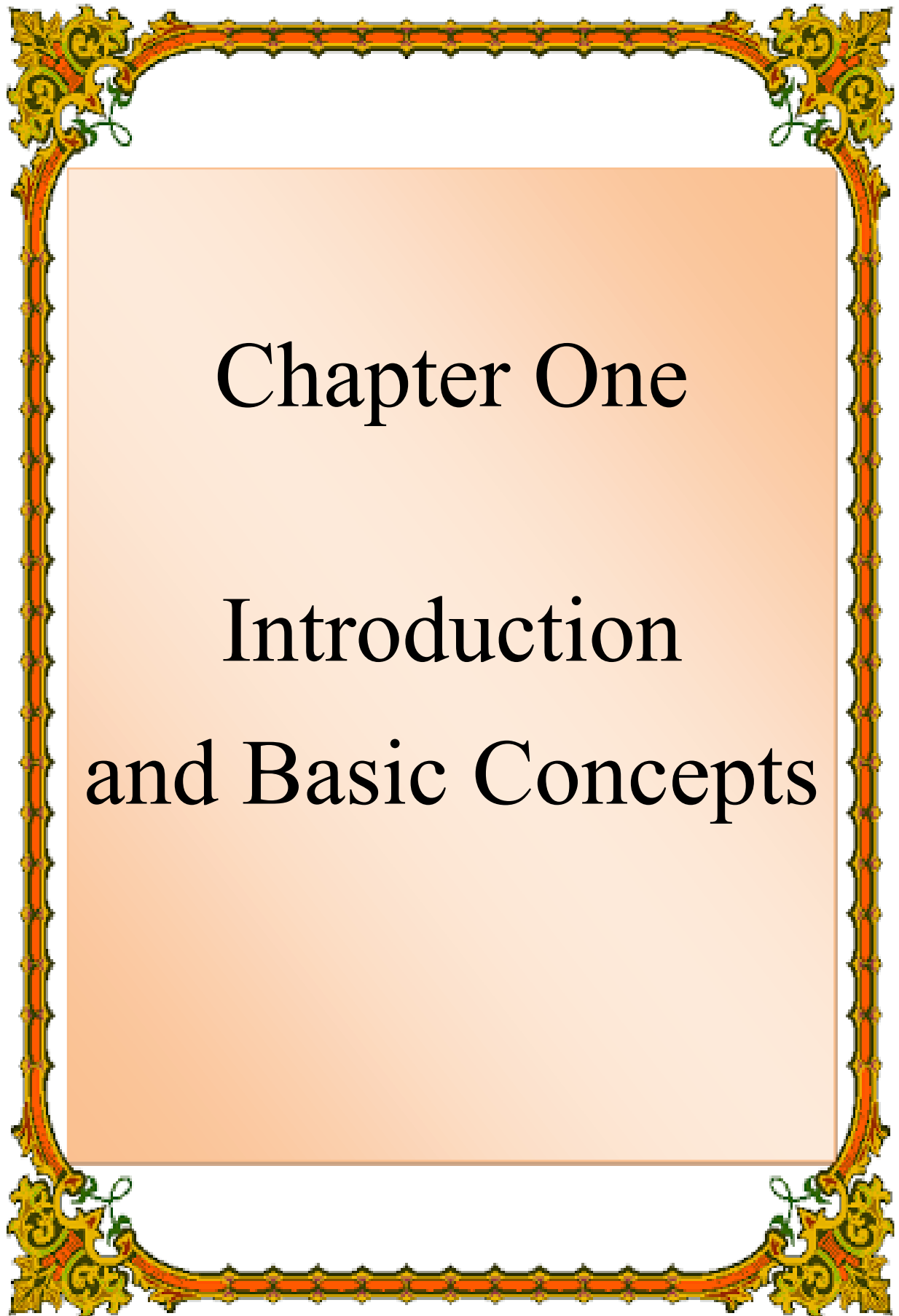
## List of Symbols

Symbol	Meaning	Unit
$\theta_B$	Bragg's diffraction angle	Degree
$\lambda$	wavelength	Å
$d_{hkl}$	Interplanar Spacing	Å
$hkl$	Miller Indices	_____
$D_{av}$	Average Crystallite Size	nm
$a_o, b_o, c_o$	Lattice Constant	Å
$K$	Shape Factor	_____
FWHM( $\beta$ )	Full Width at Half Maximum	rad
$\beta_{hkl}$	Total full width at half maximum	rad
$\beta_D$	Full width due to crystallite size	rad
$\beta_S$	Full width due to micro strain	rad
$S$	Micro strain	%
$\delta$	Dislocation density	lines/nm <sup>-2</sup>
$T_C$	Texture Coefficient	_____
$N^l$	Number of peaks evident in the diffraction pattern	_____
SSA	Specific surface area	m <sup>2</sup> /g
$S_v$	Surface Density	nm <sup>-1</sup>
$\rho$	Material Density	g.m <sup>-3</sup>
$C_R$	Corrosion rate	g/m <sup>2</sup> .day

% IE	Coating efficiency	%
$C_R^0$	corrosion rates in absence of coating layers	$\text{g/m}^2 \cdot \text{day}$
$C_R^1$	corrosion rates in presence of coating layers	$\text{g/m}^2 \cdot \text{day}$
$E_a$	Activation energy	$\text{kJ} \cdot \text{mol}^{-1}$
$M$	The Molar concentration	$\text{mol/L}$
$M_{\text{wt}}$	Molecular weight	$\text{g/mol}$
$W_t$	weight	$\text{g}$

## List of Abbreviations

Symbol	Meaning
TBCs	Thermal barrier coatings
HVOF	High Velocity Oxy-fuel Spraying
VPS	Vacuum Plasma Spraying
APS	Air Plasma Spraying
0D	Zero Dimensions
1D	One Dimensions
2D	Two Dimensions
3D	Three Dimensions
CSN	Chromia, Spinel and Nickel oxide
ALD	Atomic Layer Deposition
TEM	Transmission Electron Microscopy
SEM	scanning electron microscopy
FESEM	Field Emission Scanning Electron Microscope
EDS	Energy Dispersive Spectroscopy
HTHC	High Temperature Hot Corrosion
LTHC	Low Temperature Hot Corrosion
TGO	Thermally Growth Oxide
XRD	X-ray diffraction
W.H	Williamson-Hall
V. H. N	Vickers hardness number
PVA	Poly Vinyl Alcohol



# Chapter One

## Introduction and Basic Concepts

## 1.1 Introduction

Mechanical components operating in high temperature environments such as power plants, gas turbines, industrial waste incinerators, internal combustion engine, etc. Fail due to corrosion at high temperatures [1].

In hot corrosion, metals and alloys degrade at higher rates of air oxidation[2]. Super alloys are considered for applications at high temperatures, yet it is hard to reach the requirements of high temperature tolerance and high corrosion resistance [3]. Hot corrosion is a big problem for steam boiler tubes that operate at high temperatures and high pressure, because when burning heavy fuels, they will produce ash containing a large proportion of vanadium oxides and sodium sulfate, which have a low melting point [4].

So a system that can provide surface protection against corrosion at high temperatures is needed. Recently, researchers have paid great attention to the ceramic coatings such as  $\alpha$ -Al<sub>2</sub>O<sub>3</sub> nanopowders, because the nano oxide coating with plasma technology has higher hardness, wear resistance and porosity values are lower when compared to conventional powder coatings [5-6]. The main advantages of spray plasma are the ability to achieve high temperatures (typically up to 15,000 K) and high speeds (between 100m / s and 2500 m / s of plasma flow, when ceramic powders are inserted into the plasma stream, they are instantly melted and accelerated to spray the coating layer [7-8]. Thermal barrier coatings (TBCs) are designed to minimize the intensity of thermal transients and reduce the temperature of the substrate [9]. One of the most important thermal barriers used to protect against hot corrosion is  $\alpha$ -Al<sub>2</sub>O<sub>3</sub> nanoparticles because they have a high melting point and are not affected by chemical environments [10].

## 1.2 Classification of Corrosion

Corrosion of equipment and tools in factories, and even household appliances is classified into several categories according to the following:

### 1.2.1 Corrosion dependent on the nature of the reaction

Corrosion is classified according to the nature of the reaction into two main categories:

#### 1. Chemical Corrosion

This type of corrosion is caused by gases and fumes at high temperatures, for example, the common chemical corrosion of nickel that is included in the components of the stainless steel alloy [11].

#### 2. Electro-Chemical Corrosion

This kind of corrosion happens because of a chemical reaction between the medium and minerals and is accompanied by the transfer of the electrons. The occurrence of electrochemical corrosion requires electrolytic solutions transporting the ions where the combined effect between the metal and the solution occurs [12].

### 1.2.2 Corrosion dependent on the nature of the medium

Corrosion can be divided into two parts, according to the nature of the environment:

#### 1. Wet Corrosion

It is corrosion, which requires the occurrence of a liquid medium, which occurs as a result of the presence of a real electrochemical interaction between both the affected metal and the surrounding medium. This process occurs when it is immersed in the corrosive medium [13].

## 2. Dry Corrosion

This type occurs as a result of an interaction between the metal, gases or fumes without there being a liquid phase, this type of corrosion does not require the presence of any aqueous solution or any liquid phase. Mostly, dry corrosion occurs at high temperatures [14].

### 1.2.3 Corrosion dependent on the shape and area of the corrosion region

This classification depends on the ratio of the eroded area compared to the total area of the sample and calculating the effect of each of them according to the following:

#### 1- Uniform Corrosion

Corrosion occurs regularly in large areas of metal, i.e. one thickness, due to a chemical or electrochemical reaction through the metal to the underlying medium. It is one of the simplest wear styles, because it can be identified and expected before it happens. Uniform corrosion is not of great technological importance as it is known and expected, and this type of corrosion is avoided by choosing a suitable metal for the medium or increasing the thickness of the system to make life longer, and there are other ways to protect the metal such as coating and cathodic protection and adding corrosion inhibitors [15], as shown in Figure 1.1.



Figure 1.1: Uniform Corrosion [16].

## 2- Pitting Corrosion

Corrosion by pitting is the process of forming pits or holes in the form of local corrosion as a result of changing the metal's ability to protect in small places on the surface of the metal. Corrosion by Pitting is more dangerous than any other type of erosion, due to the difficulty in predicting it before it occurs and cannot be measured, and the difference in depth of the pits that are often covered by the products of corrosion and other materials. Figure 1.2 shows this type of corrosion [17].



Figure 1.2: Pitting Corrosion [17].

## 3- Crevice Corrosion

Crevice corrosion is localized corrosion that occurs when there are gaps in the metal, or between it and its adhesives such as rivets and gaskets between tubes and other mineral and non-metallic materials in the presence of a corrosive medium and partial stagnation within the gap [18], as shown in the Figure 1.3.



Figure 1.3: Crevice Corrosion [16].

#### 4- Erosion Corrosion

Erosion corrosion is the process of accelerating the breakdown of a metal by the relative movement between the corrosive fluid and the surface of the metal. The speed of movement is often required to be strong enough to either sculpt the metal as dissolved ions or create solid corrosion products that are mechanically scraped by the fluid flow [19], as shown in the Figure 1.4.



Figure 1.4: Erosion Corrosion [16].

### 1.3 Hot Corrosion

Hot corrosion occurs at high temperatures and is similar to the oxidation process, but it occurs when there are pollutants other than oxygen, and this corrosion occurs in boilers and gas turbines (marine, air, industrial). The

cause of hot corrosion is that the fuel contains many polluting elements and when burned, they turn into ashes, causing corrosion of the metal and thus reducing its life.

The key impurities in fuels are (sodium, vanadium, and sulphur), these are volatile, settling gaseous substances on surfaces and tubes facing flame where different fuses are the most important compound of sodium vanady vanadntas ( $\text{Na}_2\text{O} \cdot \text{V}_2\text{O}_4 \cdot 5\text{V}_2\text{O}_5$ ), it is deposited on the boiler heaters surface and, its melting point is relatively low  $550^\circ\text{C}$  [21]. Hot corrosion reduction is the subject of most research while using corrosion-resistant alloys. The treatment is done by removing sodium and vanadium from the fuel by using inorganic surface coatings or by developing chemical additives that hinder or prevent most of the ash from depositing on the surface of metals [22-23].

#### 1.4 Thermal Barrier Coatings (TBCs)

Ceramic materials are used as thermal barrier coating materials (TBC), because they have low thermal conductivity [24-25]. The most important ceramic materials such as  $\text{Al}_2\text{O}_3$ ,  $\text{TiO}_2$ , and YSZ (yttria stabilized zirconia) or consist of a mixture of ceramic materials such us  $\text{SrZrO}_3$ ,  $\text{CaO/MgO} + \text{ZrO}_2$ ,  $\text{CeO}_2 + \text{YSZ}$ ,  $\text{Y}_2\text{O}_3 + \text{HfO}_2$ ,  $\text{La}_2\text{Zr}_2\text{O}_7$ ,  $\text{La}_2\text{Ce}_2\text{O}_7$ , and  $\text{LaMgAl}_{11}\text{O}_{19}$  [26].

The choice of TBC materials is limited to some basic requirements, such as high melting point, no phase shift between room temperature, operating temperature, low thermal conductivity, chemical inertness, thermal expansion matching with the metallic substrate, good adhesion to the metallic substrate and low sintering rate of the porous microstructure [27].

The effects of nanostructures on coatings have been studied recently and major change compared with micron size variables was observed. The most commonly used nanoparticles in coatings are  $\text{SiO}_2$ ,  $\text{TiO}_2$ ,  $\text{ZnO}$ ,  $\text{Al}_2\text{O}_3$ , and  $\text{CaCO}_3$ .

The applications of nanoparticles depend particularly for the properties inherent in them. Nano-alumina and nano-silica for example were used to strengthen the scratching of the covering corrosion and abrasion resistance [27].

The improved properties are the result of a much larger surface to volume ratio of nanomaterial's [28]. In general, the TBC natural system consists of a ceramic top layer and a metal bond coat MCrAlY (M = Nickel or Cobalt, Chromium, Aluminum and Yttrium) on the substrate. The MCrAlY layer can provide good thermal expansion match and adhesion between the ceramic top layer and substrate as well as protect the substrate from further oxidation and hot corrosion [29].

## 1.5 Thermal Spray Methods

Thermal spray consists of pouring a material (mostly powder or wire) and dropping it as molten particles on the substrate. When affecting the substrate, the molten particles will flatten and solidify very quickly [30].

Adhesion is primarily mechanical for this reason, the MCrAlY spray-painted coating is often given a heat treatment post-curing to get a good adherence [31]. All thermal spraying operations are linear, meaning that the parts directly in the spray [32]. Figure 1.5 shows the classification of thermal spraying operations [30].

The following technologies can be generally categorized into thermal spraying methods:

### 1.5.1 Flame Spraying

This process consists of the acetylene oxygen mixture via a nozzle, and the ignition flame is ignited. The layer of powder or wire fed in the flames, the deposit was accelerated and dropped onto the substrate. The temperature of the combustion flame is limited to 3000 °C, and the speed of the gas molecule is relatively small [33].

### 1.5.2 High Velocity Oxy-fuel Spraying (HVOF)

This method involves the combustion of fuel gas with high-pressure oxygen, which produces high-speed flame powder coating materials on the substrate. This technology will manufacture high-quality coatings for gas turbine applications [34].

### 1.5.3 Wire Arc Spraying

Spray with wire arc is a type of thermal spray, This method involves the creation of molten particulate matter at the ends of two wires consumed by heating resistance. Instead a compressed air plane shreds, the material and drops it onto the substrate. This method is limited to the spraying of lead wires, those are fairly cheap and can attain high rainfall levels [35].

### 1.5.4 Vacuum Plasma Spraying (VPS)

This method has many advantages over the spraying of an air plasma. Air quality related issues in plasma planes are removed, the plane with plasma is longer than the air and can cross (400-600 ms<sup>-1</sup>), particle velocities resulting in extremely pure deposits and density. Another feature is paint adhesion [36].

### 1.5.5 Air Plasma Spraying (APS)

A DC arc is used in air plasma spraying, between a central inert cathode and an annular copper anode. To form a high-temperature plasma an inert gas is fed into the arc. The material is fed into the plasma and excreted onto the ground at a high pace [37]. This method was used in this work.

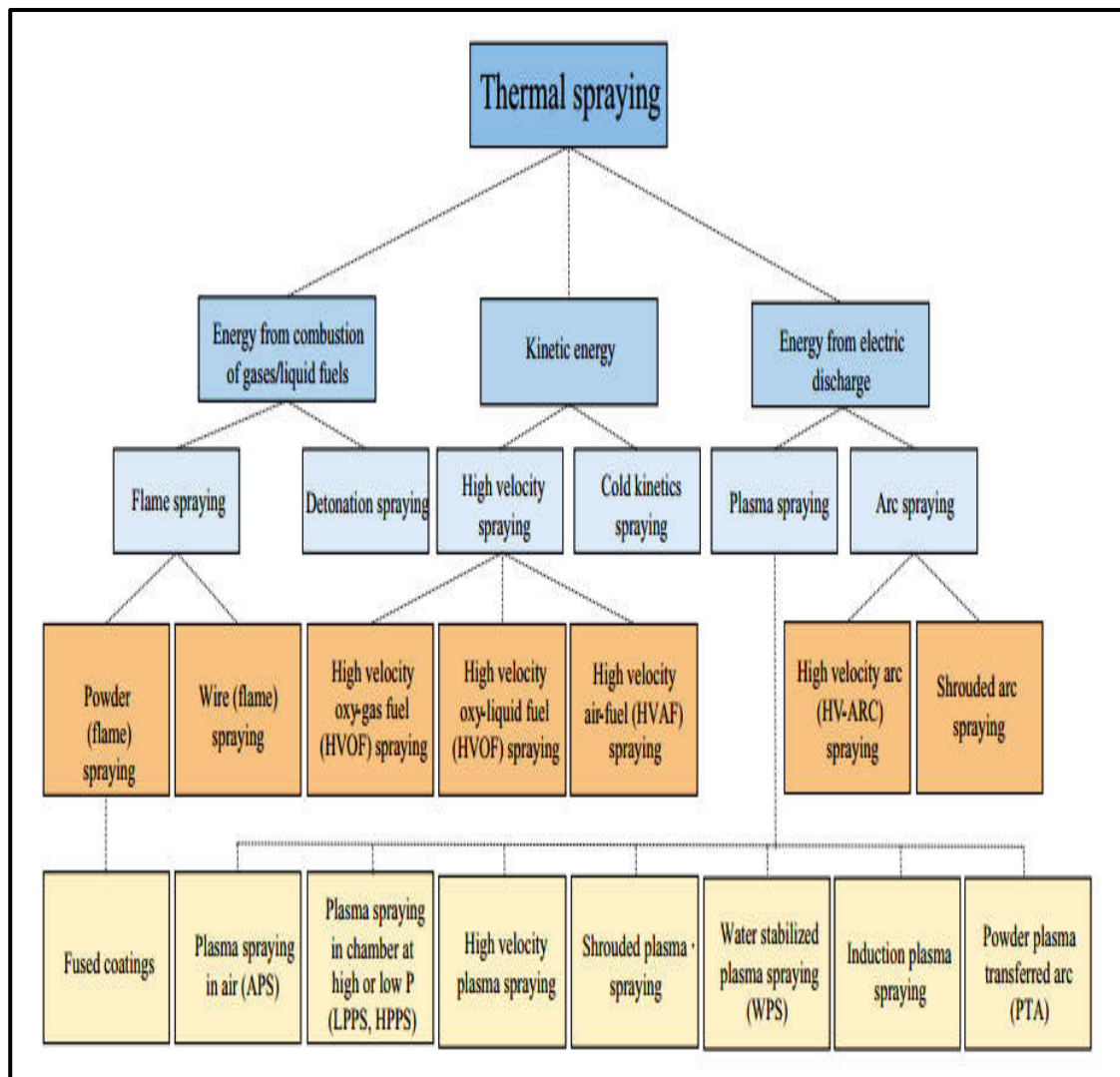


Figure 1.5: The classification of thermal spraying operations [30].

## 1.6 Nanomaterials

Nanotechnology has become at the forefront of the most important and exciting areas in the field of physics and other sciences, it has given great hope to scientific revolutions in the near future that will change the

direction of technology in many applications. Nanomaterials can be defined as those advanced materials that dimensions range from (1–100 nm) [38]. Nanoparticles possess unique properties due to their important mechanical and physical properties that may lead to new and exciting applications. Significant progress has been made in various aspects of the nanomaterial composition.

The focus is now shifting from synthesis to manufacturing useful structures and coatings with greater wear and corrosion resistance [39].

The properties of materials change very much according to their nanoparticles. Compounds consisting of granules in the size of nano whether ceramics or metals, are much stronger than their counterparts in the larger size [40].

### **1.6.1 Classification of Nanomaterials**

Nanomaterials can be classified according to their dimensions into four types [40]:

#### **1- Zero-dimension (0- D)**

Substances of all dimensions within the nanoscale (no dimensions, or 0-D, are smaller than 100 nm). An example of this is nanoparticles [41].

#### **2. One dimension (1-D)**

One dimension of nanostructure in these nanostructures would be beyond the range of nanometers. for example (Nanowire and Nanotubes ) [41].

#### **3. Two dimensional (2-D)**

There are two dimensions in this type of nanomaterial outside the range of nanometers. These involve various types of nano films, such as coatings and thin multilayer films, nanowalls or nano-sheets.

#### 4. Three Dimensional(3-D)

All of these measurements are outside nano meter scale. Which involve, bulk materials that consist of individual blocks within the range of nanometers (1-100 nm)[41]. Figure 1.6, shows the types of nanomaterials.

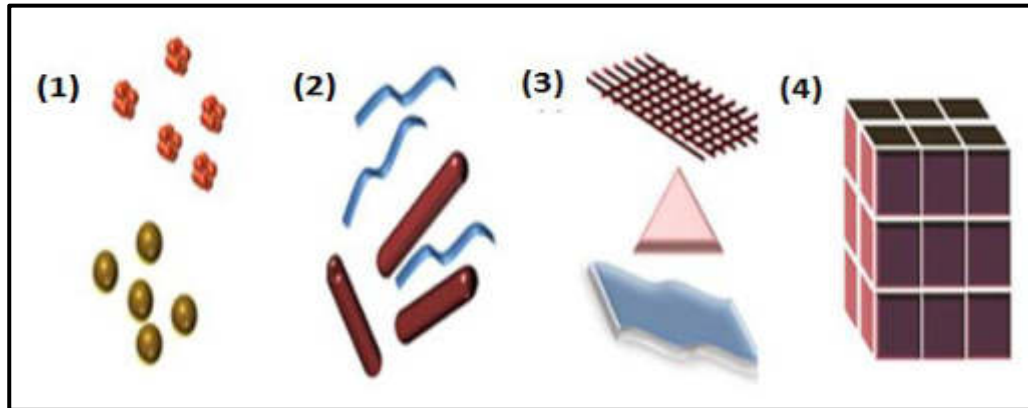


Figure 1.6: Schematic illustration classification of nanomaterials  
(1) 0D spheres and clusters, (2) 1D Nano fibers, Wires, and Rods,  
(3) 2D Films, Plates, and Networks, (4) 3D Nanomaterials [42].

#### 1.6.2 Synthesis of Nanomaterial

There are many techniques for synthesis of nanomaterials that are divided into two main parts: One of them starts from top to bottom, where the original (large) material is gradually broken down until it reaches the nanoscale, and this is done through various processes including drilling, optical cutting and grinding, it was possible to obtain nanocomposites with important electronic applications, while the second technique begins from Bottom-Up, that is, unlike the first technology, as the nanomaterial is built from atoms and molecules in an orderly manner until we reach the required nanoscale size, and this technique includes often chemical techniques, characterized by the small size of the resulting materials, and obtaining strong bonds [43-45]. Figure 1.7 shows the most important methods used to prepare nanomaterials.

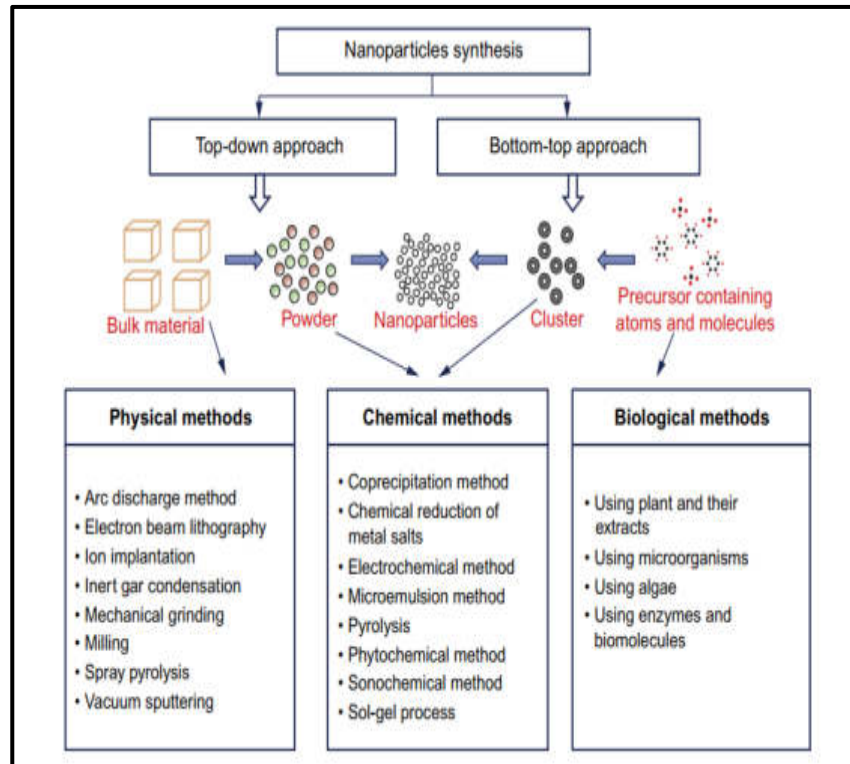


Figure 1.7: Schematic illustration of top-down and bottom-up Approach for synthesis of nanoparticles [46].

## 1.7 Sol–Gel Method

Sol-gel is an important method for both the preparation of metal oxides and mixed oxide compounds. This approach has the advantage of controlling the structural and surface properties of the prepared materials [47]. The Sol-gel process essentially takes several steps to obtain the final oxide of metal, which is, the hydrolysis process, condensation and drying process [48]. Metal oxide formation requires varying successive phases. The precursor mineral precursors, for example, undergo rapid hydrolysis to create a metal hydroxide solution, instant condensation resulting in the formation of 3D gels followed. After that, the obtained gel undergoes drying process. The Sol-gel method can be classified into two methods, such as the aqueous and non-aqueous sol-gel method that depends on the nature of the solvent used [48]. Figure 1.8 shows the reaction pathway to produce the nanoparticles by the Sol-Gel method.

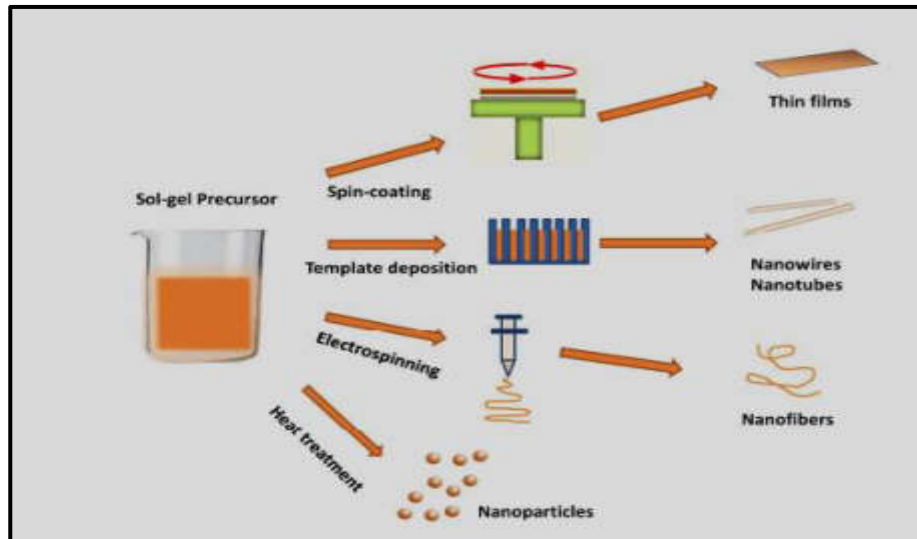


Figure 1.8: Schematic illustration of sol-gel method [49].

### 1.7.1 Applications of the Sol-Gel

Despite the limited sol-gel technique, the sophistication of the sol-gel systems enables the synthesis of several different structures for many applications, and paves the way for the development of different materials, including:

1. It provides an alternative way to produce ceramic and glass [47].
2. Introduces new methods to synthesis fine powders [47].
3. The ability to manufacture exceptionally pure metal oxides led to its use of optical components like lenses and optical fibers [48].
4. Films and coatings represent the first commercial use of sol-gel Processing [48].

### 1.7.2 Advantages of Sol-Gel Method

1. The composition can be precisely controlled.
2. The degree of homogeneity is high.
3. The temperature is low during preparation.
4. Viscosity is easy to control, by an appropriate choice of solvents [47].

5. The coating can be obtained with a large area of thickness and required composition.
6. It is used for the deposition of coatings on the surfaces of the substrate by a single dipping process [51].
7. The homogeneity of the reaction products and the microstructure can be controlled.
8. Nanoscale products can be obtained.
9. Its cost is low and requires no complicated equipment [52].

### **1.7.3 Disadvantages of Sol-Gel Method**

1. Toxic solvents are sometimes used.
2. Raw materials are expensive and take a long time to process and dry [51].
3. Problems with changing dimensions in condensation and contraction Related [52].

## **1.8 Low carbon steel**

Low carbon steel is a type of steel that has a small percentage of carbon which ranges from 0.05% to 0.3%. Its low carbon content makes it more flexibility and ductile than other types of steel, because of its high flexibility, it is ideal for applications[53] . It is less prone to corrosion than other types of steel due to its low carbon content. Stainless steel is generally used in chemical industries and power plants.

Examples of these devices include petroleum reactors, heat exchangers, tubes and pipes, many items used in the pulp and chemical industries and several parts of furnaces and fossil-fuel power station boilers [54].

Austenitic, ferritic and martensitic are the three primary types of stainless. Its microstructure or primary crystal phase, determines these three types of steel [55].

### **1. Austenitic:**

Austenitic steel is the starting point for austenite (FCC crystal). Those are alloys which contain nickel and chromium, and occasionally, nitrogen and manganese, most common stainless steel most likely is the type 304 that contains (18-20 %) chromium and 8-10% nickel. This type was used in our study[56].

### **2. Ferritic:**

This form has a high percentage of chromium, when compared to other forms, this results in ferrite stability, and is not subject to hardening either. The group's most common forms of alloys are alloy (430), that characterizes strong air-resistance to corrosion, therefore It is commonly used in auto production decorative elements and in plants for oxidation of ammonia and in the manufacture of household food items. Because of the high percentage of chromium, the two forms (422) and (446) are distinguished by sulfur resistance [57].

### **3. Martensitic:**

This group is named after it, because it has competence to form a martensite, when it is quickly cooled from the state where its composition is located, it is called Austenite, i.e. from high temperatures.

The alloys of this group are distinguished by their containment of carbon and have low magnetism and weld ability, moderate wear resistance, as the corrosion resistance of this group's alloys is lower than the alloys of the second and third groups, and their tensile and hardness resistance is high so

they are used for purposes that require tensile and hardness resistance High resistance and relatively moderate corrosion resistance [58].

## 1.9 Aluminum Oxide ( $\text{Al}_2\text{O}_3$ )

Aluminum oxide is a chemical compound of the formula  $\text{Al}_2\text{O}_3$ , also called alumina. It is found in several phases that differ from each other in the crystalline structure, physical and chemical properties in addition to its various applications. Aluminum oxide (alumina) has unique properties that made it one of the most important engineering materials in the late twentieth century, including: chemical stability, very high melting temperature, and high hardness, which allowed its use in many areas, especially in the manufacture of ceramics, refinement and optics (due to the transparency of its films). It also acts as a mediator in some chemical reactions. Bauxite (aluminum hydroxide)  $\text{Al}(\text{OH})_3$  is the main raw material obtain alumina. It also contains the percentage of alumina (40- 68) % as well as with varying proportions of impurities ( $\text{Fe}_2\text{O}_3$ ,  $\text{SiO}_2$ ,  $\text{TiO}_2$ ) that are commonly used in various applications in ceramics and refractories [59-61]. Table 1.1 shows some of the chemical, mechanical and physical properties of oxide in aluminum [62]. The most significant aluminum oxide phases include:

1- **Alpha-alumina phase:** This phase is formed after heat treatment to bohemite  $\text{AlO}(\text{OH})$  at  $1000^\circ\text{C}$ . This is a stable, thermodynamic process, with different characteristics, thermal stability, (the melting point of  $\alpha$ -alumina is around  $(2040^\circ\text{C})$ , strong hardness and stable chemicals. This allows for the use of in the manufacture of ceramics, protective coatings and ceramic shields. This phase was prepared in this work and used to coating of low carbon steel samples [63]. Figure 1.9 shows the unit cell of  $\alpha\text{-Al}_2\text{O}_3$ .

**2-Gamma-Alumina Phase:** It is an unstable phase that converts to ( $\gamma$ -phase) by conducting heat treatment in the range 600–700 ° C. It is used as a medium in chemical reactions, but it is not used at high temperatures because it is converted at the degree of 950 °C to the  $\alpha$ -phase [64].

Table. 1.1 Some, Chemical, Physical, and Mechanical properties of aluminum oxide [62].

Molecular formula	color	Molar mass $\text{g}\cdot\text{mol}^{-1}$	Density $\text{g}/\text{cm}^3$	Melting Point	Boiling point	Hardness MPa	Tensile strength MPa
$\text{Al}_2\text{O}_3$	White	101.96	3.95	2040 °C	2980 °C	137.293	220

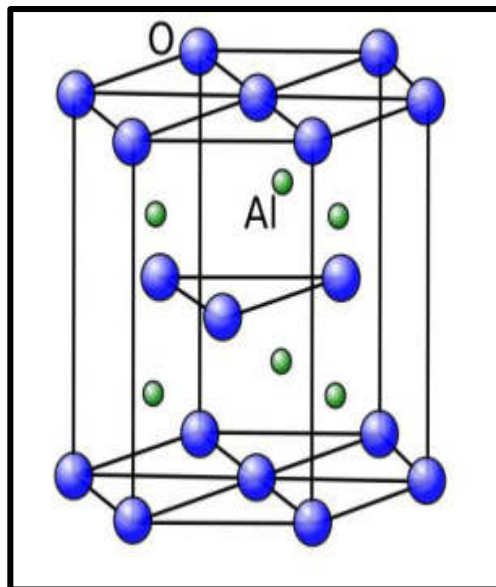


Figure 1.9: The unit cell of  $\alpha$ - $\text{Al}_2\text{O}_3$  [63].

### 1.9.1 Aluminum oxide ceramic applications

Aluminum oxide ceramics are varied and numerous, which reflect their strong mechanical properties, including, chemical inertness and toughness, including the following [65, 66] :

1. Aluminum oxide ceramics are primarily used in areas which are exposed to high temperatures, such as furnaces, due to the high melting temperature and because it is chemically inert.
2. Alumina is used as a protection for heavy and light vehicles due to its high strength and light weight, and is also used in bullet-proof vests as the first layer that stands in the face of a fiery projectile because the high hardness of alumina distorts the head of the projectile.
3. It used to manufacture grinding, cutting and smoothing instruments, due to its cheap price compared to industrial diamonds on the one hand, and because it has a very high hardness that follows the roughness of diamonds on the other hand, as well as its high resistance to corrosion.
4. It is used in many chemical reactions as a catalyst, such as the reactions of dehydration of alcohols to give alkenes.
5. It is used in dental field medical applications and ceramic thigh bone.
6. In electronic applications it is used, as substrate and digital circuit holders. It is also used in the manufacture of thermal caustic used in electronic circuits to weld some parts in it.

### **1.10 Nickel Chromium Aluminum Yttrium alloy**

Nickel Chromium Aluminum Yttrium (NiCrAlY) Alloy is an MCrAlY alloy with high temperature stability and corrosion resistance for thermal spray coatings and other applications.

These materials are used as a binder between the substrate of the coating and the top ceramic layer or alone to resist corrosion at temperatures up to (980 °C - 1050 °C) if the air plasma spray method is used [67]. When using this alloy in coatings, chromium and aluminum will provide protection by forming an oxide layer.

Yttrium improves the adhesion of this oxide layer. As for chromium oxide, it is very useful in resisting hot corrosion and sulfate[68]. Table 1.2 some properties of an NiCrAlY alloy[67].

### 1.10.1 Applications of NiCrAlY alloy

1. NiCrAlY has a low aluminum content and a higher chromium content that may be more suitable for hot corrosive environments.
2. Used as a thermal barrier bond coat and breakable ceramic applications.
3. The coating is applied to steel, nickel, iron, or cobalt substrates to reduce oxidation.
4. It has the ability to resist oxidation and hot corrosion on industrial and aerospace turbine components.
5. It invests in protecting exhaust vents and channels [69,70] .

Table 1.2 Some properties of NiCrAlY alloy[67].

Molecular Formula	color	Molar mass $\text{g}\cdot\text{mol}^{-1}$	Density $\text{g}/\text{cm}^3$	Melting Point $^{\circ}\text{C}$
NiCrAlY	Dull Grey	225.763	7.5	1400

### 1.11 Previous Studies

**Junguo Gao et al. in (2010)** studied the fabrication and high temperature oxidation resistance of  $\text{ZrO}_2/\text{Al}_2\text{O}_3$  micro-laminated coatings on stainless steel by electrolytic deposition. The results showed that  $(\text{ZrO}_2 / \text{Al}_2\text{O}_3)$  coatings possess resistance to oxidation and fragmentation of the stainless steel substrate, and they indicated that the cause of this effect

was associated with the suppression of oxygen diffusion of the multiple closed  $\text{Al}_2\text{O}_3$  layers [71].

**Mirjalili et al. in (2011)** synthesized ultrafine nano  $\alpha$ -alumina particles by sol-gel method. The samples were diagnosed by various methods, those include the Brunauer-Emmet-Teller process, XRD, Thermogravimetry study, DCS, FTIR, SEM and TEM. The results indicated that the addition of sodium dodecylbenzen sodium and bis-2ethylhexyl sulfosuccinate sulfonates not only affects the particle size and shape of the nanoparticles produced but also the degree of aggregation [72].

**Marin et al. in (2011)** AISI 316 stainless steel samples used were coated using ( $\text{Al}_2\text{O}_3$ - $\text{TiO}_2$ ) base atomic layer deposition (ALD). The morphology, structure, and protection against corrosion were then analyzed using different techniques. For a morphological characterization of coatings and substrates, atomic force microscopy (AFM) and scanning electron microscopy (SEM) were used. The corrosion safety obtained on AISI 316 stainless steel by applying nano metric coatings has been shown to be very effective in reducing the current passive region density from ( $10^{-7}$  to less than  $10^{-9}$  A /  $\text{cm}^2$ ) and increasing the possible passive region period from 0.8 to 1.3V before breakdown [73].

**Daroonparvar et al. in (2013)** studied the hot corrosion of yttria stabilized zirconia (YSZ), normal  $\text{Al}_2\text{O}_3$  and YSZ/nano- $\text{Al}_2\text{O}_3$  coatings was studied in the presence of a molten mixture of  $\text{Na}_2\text{SO}_4 + \text{V}_2\text{O}_5$  at 1000 °C. Their results showed the presence of the  $\text{Al}_2\text{O}_3$  nanostructure layer on the conventional YSZ layer that could significantly reduced the salinity of corrosive salts to the YSZ layer during hot corrosion [74].

**Negate et al. in (2014)** studied the three forms of active hot corrosion of the plasma sprayed, normal ceria-stabilized zirconia (CSZ), CSZ / Micro Al<sub>2</sub>O<sub>3</sub>, composite layer and CSZ / Nano Al<sub>2</sub>O<sub>3</sub> layer composite, for which Al<sub>2</sub>O<sub>3</sub> was a CSZ layer topcoat. The analysis indicated that no harm to the surface of the coating layer due to hot corrosion (CSZ / Nano Al<sub>2</sub>O<sub>3</sub>), while a small fraction of the coating layer (CSZ / Micro Al<sub>2</sub>O<sub>3</sub>) occurred compared to the usual (CSZ) layer [75].

**Keyvani et al. in (2014)** compared the stability of the traditional yttria stabilized zirconia (YSZ) coating with the nano sensitive composite (YSZ + Al<sub>2</sub>O<sub>3</sub>) coating. On a nickel-based super alloy (Inconel 738) base using the plasma spray method. Oxidation and hot corrosion were tested at 1100 °C and 1050 °C using Na<sub>2</sub>SO<sub>4</sub> and V<sub>2</sub>O<sub>5</sub> molten salts were performed on the coatings. The results showed that YSZ+Al<sub>2</sub>O<sub>3</sub> structural nano composition layer has better oxidation resistance than conventional YSZ layer. YSZ + Al<sub>2</sub>O<sub>3</sub> nano composite also showed better resistance to hot corrosion test [76].

**Doodman et al. in (2014)** studied the effect of nanostructured alumina thin films were coated on stainless steel by Sol-Gel dip coating method. In order to prevent crack formation. Effects of calcination temperature and withdrawal speed on structural properties were analyzed using XRD and SEM. Topography and thickness of coatings were analyzed by AFM. Effects of the above parameters on anticorrosion performance of coats have been evaluated through electrochemical polarization technique. The results indicated that the optimum calcination temperature to achieve the best corrosion protection was 400 °C. The thickness of one time coating with 1mm/s withdrawal speed was about 146 nm [77].

**Khadom et al. in (2015)** studied the high temperature external corrosion of boiler pipes was evaluated using weight loss technique. . They reported that Samples of low carbon steel were supplied from north of Baghdad thermal station and used in their study. Locally supplied fuel ash was used as corrosion environment. Corrosion rates were determined as a function of time in the absence and presence of fuel ash. The results showed that the corrosion of boiler steel pipes was higher in the presence of fuel ash [78].

**Ismardi et al in (2016)** they prepared the alumina nanoparticles successfully using the Sol- Gol method. They reported that, some properties revealed that the size of the nanoparticles was about 6 nm, while it also had a high crystalline structure. The alumina nanoparticles were used with the base liquid to lower the engine cooling model system temperature. It has been shown that the thermal properties of nanofluids are linearly proportional to the concentration of  $Al_2O_3$  nanoparticles, and the higher concentration in the nanostructure, the less time it takes to reduce the temperature [79].

**Farahmandjou and Golabiyan in (2016)** prepared alumina ceramic nanoparticles by simple sol-gel method. Physicochemical properties were done using X-ray diffraction (XRD), high resolution transmission electron microscopy (HRTEM), field effect scanning electron microscopy (FESEM) and electron dispersive spectroscopy (EDS). The prepared sample had a mean particle size of about 28 nm, estimated on XRD methodology and direct observation of TEM. SEM surface morphology studies depicted grain particles with less agglomeration to the sphere-like shape of nano-sized  $Al_2O_3$  by increasing the temperature of the annealing [80] .

**Rakesh et al. in (2017)** the ASME-SA213-T22 boiler tube coated with carbon nanotubes reinforced with  $\text{Al}_2\text{O}_3$ . Hot corrosion behavior was evaluated at  $900^\circ\text{C}$  in the actual boiler environment. The coating was deposited using plasma spraying technique and Ni-Cr was used as a bonding layer before CNTs- $\text{Al}_2\text{O}_3$  coatings were applied. Hot corrosion studies were carried out on non-encapsulated plasma samples in the actual boiler of the thermal power plant. Corrosion results were analyzed using X-ray diffraction (XRD), scanning electron microscopy, energy-dispersive x-ray analysis (SEM, EDAX) techniques. The study demonstrated that the alumina coating greatly enhanced resistance to corrosion [81].

**Karabaşa et al. in (2017)** studied the hot corrosion behavior of alumina – yttria stabilized zirconia particle composite coatings produced by thermal spraying, for use as a thermal barriers by plasma sprayed coatings have been exposed to 50 wt %  $\text{Na}_2\text{SO}_4$  + 50 wt %  $\text{V}_2\text{O}_5$  corrosive molten salt temperatures at  $1050^\circ\text{C}$  for 60 hours. Their results have shown that the amount of  $\text{YVO}_4$  crystals on the surface of YSZ coatingsd while  $\text{Al}_2\text{O}_3$  increasing in YSZ +  $\text{Al}_2\text{O}_3$  composition, therefore, the hot corrosion resistance of TBC improves with the addition of  $\text{Al}_2\text{O}_3$  [82].

**Rajeh, et al. in (2017)** studied the hot corrosion for the alloys used in high temperature. This study were concluded experiment for two types of steel using in steam boilers. The ordinary oxidation processes conducted for specimens of steel in the temperature (550, 650, 750, 850 and  $950^\circ\text{C}$ ) for different times and then different temperature are used with constant times (3 h). Coating process for specimens by impurities material in the following percentage (67%wt.  $\text{V}_2\text{O}_5$ : 33wt.  $\text{Na}_2\text{SO}_4$ ) were performed. After the oxidation processes for samples were done calculate the change in weight. And then used the inhibitor material (MgO) to decrease the effect of

impurities on the steel samples and the oxidation processes doing and calculated the change in weight, the ratio (3Inhibitor:1Ash) inhibitor give best results [83].

**Najy et al. in (2017)** reported about the hot corrosion occurring in power generation steam boiler tubes (fire side corrosion). Austenitic grade 304 L stainless steel alloy was used for tests on. Synthetic ash has been used as a corrosion setting (33 %  $\text{Na}_2\text{SO}_4$  + 67 %  $\text{V}_2\text{O}_5$ ). Oxidation experiments and corrosion tests were performed at various temperatures (600, 700, 800 and 900 °C) with fixed time (6 h) and fixed temperature with variable time (2 , 4 and 6 h. Hot corrosion testing was done, based on how weight varies. The corrosion check was conducted without using inhibitor and with use of double inhibitor consisting of ( $\text{SiO}_2$ ) mixed with MgO. X-ray diffraction analysis used to classify the corrosion product and SEM testing was used to study the metal oxide layer, the start of corrosion in the steel sample indicating that alkaline (MgO) is the main influence on corrosion inhabitants [84].

**Kadhim et al. in (2018)** studied the chemical corrosion at a high temperature of a super alloy of IN-738 LC coated with zirconia containing 20% wt ceria and 3.6% wt yttria and coated on a medium coating layer of  $\text{Ni}_{24.5}\text{Cr}_6\text{Al}_{10.4}\text{Y}\%$  (Wt) using plasma spraying. The upper surfaces of ceria yttria stabilized zirconia (CYSZ) were covered with a salt mixture consisting of 45 wt%  $\text{Na}_2\text{SO}_4$ -55 wt%  $\text{V}_2\text{O}_5$  and tested at different temperatures from 800 to 1000 ° C and in a time of 1 to 8 hours. Topography of surfaces, roughness, chemical composition, phases, and corrosion products of the top surfaces of the spray layers have been determined using an electronic scanning microscope, an energy differential spectrometer, roughness measuring device, and X-ray diffraction.

XRD analyses of the plasma sprayed coatings after hot corrosion confirmed the phase transformation of non-transformable tetragonal (t') into monoclinic phase, presence of  $YVO_4$  and  $CeVO_4$  products. [85].

**Hamood et al. in (2018)** studied two types of diffusion coated by cementation (Single Aluminized Coating, Thermal Barrier Coating) at (1000 °C) with (2,4,6 h) in the presence of a salt fuse (NaCl). Their results showed that, the thermal barrier coating provided excellent protection for the alloy throughout the exposure period (120 hours due to the improvement in the protective oxidation crust adhesion) ( $\alpha\text{-Al}_2\text{O}_3$  for this epithelial system, followed by the performance of the single coating is aluminum, while the uncoated base alloy collapsed and no resistance appeared during the first sulfur cycles, and the reason for this is likely to be the formation of chloride, oxychloride and dioxide compounds under the oxide cortex, which led to its cracking and failure of the models [86].

**Mainier et al. in (2019)** studied the use of sodium sulfate and vanadium pentoxide in different proportions, using carbon steel coupons in the form of a half cane. At (500, 700 and 800 °C) temperatures and at exposure times (12, 24 and 36 h). their results evaluated for depth of erosion attack and mass loss using confocal microscopy. The results indicated a deeper pitting in the ratio of  $2\text{Na}_2\text{O.V}_2\text{O}_5$  at the three test temperatures. The average fish loss in coupons was 11% at a temperature of 800 °C and within 36 hours [87].

**Singh et al. in (2019)** coated steel (SA213 T-91) with different quantities of ( $\text{Al}_2\text{O}_3$  and  $\text{ZrO}_2$ ) using the plasma spray system to test the behavior of resistance to hot corrosion. Steel-coated samples were tested at

---

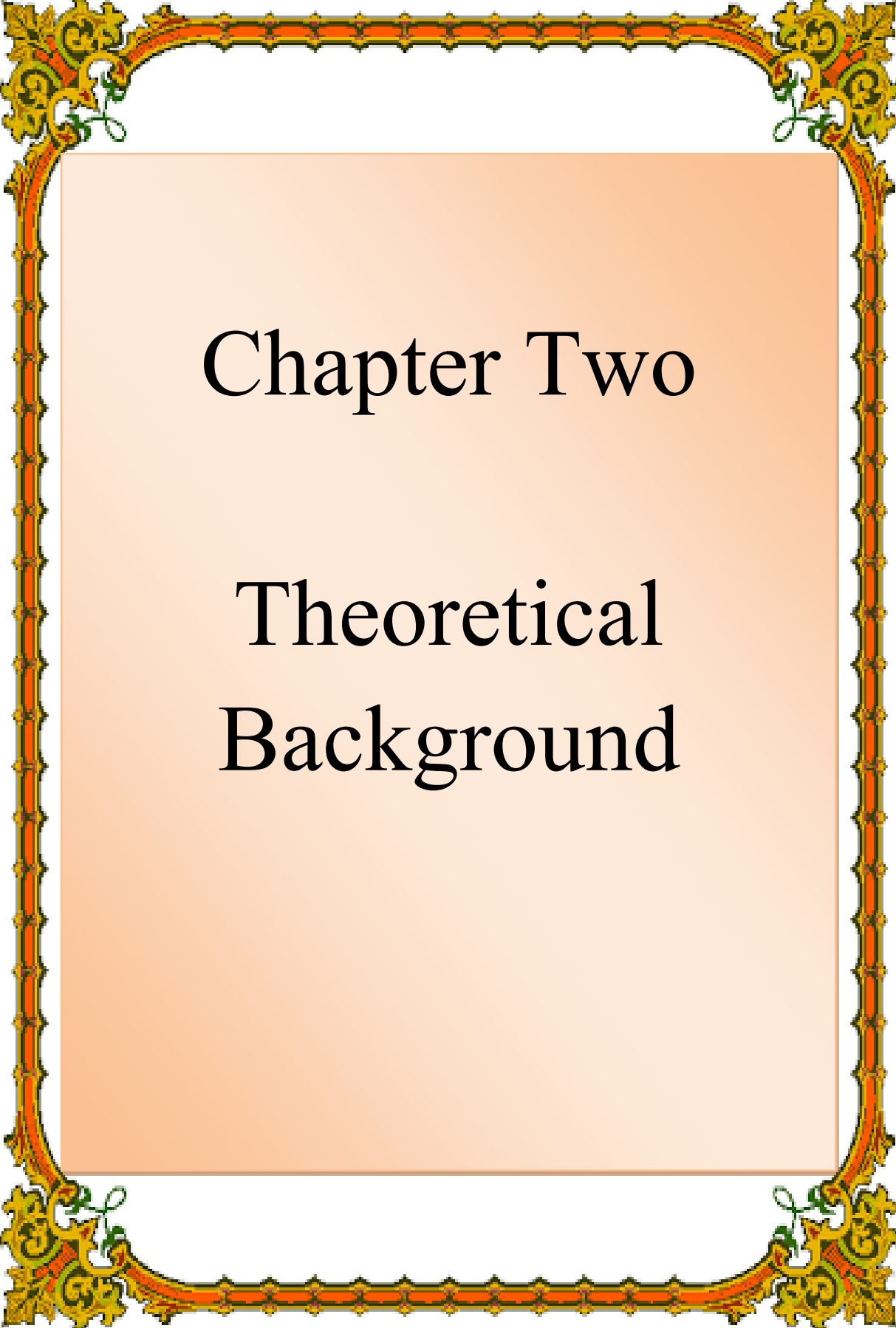
a temperature of 900 ° C inside the furnace for 50 cycles using a molten salt atmosphere of (60 % Na<sub>2</sub>SO<sub>4</sub> - 40 % V<sub>2</sub>O<sub>5</sub>). Every cycle is composed of (1h), heating and refrigeration at room temperature (20min). Their findings were analyzed using visual exam, measurement of weight increases, X-ray diffraction techniques and X-ray spectroscopy (SEM - EDS). The findings showed that brushed steel from T-91 was more vulnerable to hot corrosion compared to samples of coated steel. It was observed that the reinforcements of ZrO<sub>2</sub> in the Al<sub>2</sub>O<sub>3</sub> paint matrix have helped to improve the wear resistance of these coatings. Resistance to corrosion improved with an increased amount of ZrO<sub>2</sub> in the coating matrix [88].

**Praveen and Arjunan, in (2020)** studied the addition of nano-Al<sub>2</sub>O<sub>3</sub> particles to the microstructure and oxidation of (NiCrSiB) fast speed oxy fuel (HVOF) painting on stainless steel substrate (AISI 304) studied. It the correct coating hardness improved from (576 HV to 748 HV) with the addition of 1.4 wt percent of nano-Al<sub>2</sub>O<sub>3</sub> [89].

**Singh et al. in (2020)** coated ASTM-SA213-T-22 steel using the plasma spray process with (100Al<sub>2</sub>O<sub>3</sub>) and (20 TiO<sub>2</sub>-Al<sub>2</sub>O<sub>3</sub>). In a molten salt setting (Na<sub>2</sub>SO<sub>4</sub>- 60 per cent V<sub>2</sub>O<sub>5</sub>), the effect of hot corrosion was studied at 900 °C. Inside the muffle furnace were the bare and coated samples. Each cycle involved heating at ambient temperature for (1 h and 20 min) of cooling. Their tests were analyzed using visual inspection, XRD calculation of mass transition, and an analysis of SEM / EDS. The coated sample showed a mass decrease of 25.41 percent and 67.02 percent relative to the uncoated sample, respectively. Al<sub>2</sub>O<sub>3</sub> TiO<sub>2</sub> coating showed greater adhesion [90].

**1.12 Objectives of the study**

1. Synthesis and diagnosis of alumina ceramic nanoparticles using sol– gel method and study the structural properties.
2. Preparation and deposition of alumina ceramic nanoparticles as a thin film as a second layer over the binding material (NiCrAlY) on the outer surface of the steel surface using the plasma spray method.
3. Studying the surface morphology of the steel surface before and after oxidation test by fuel ash, and before and after coating .
4. Study the effect of high temperature corrosion on uncoated and coated samples with the presence and absence of corrosion medium,
5. Suggesting optimal conditions to reduce the external corrosion process that the steam boiler tubes are exposed to in the thermal electric power plants that operate on heavy fuel.



# Chapter Two

## Theoretical Background

## 2.1 Introduction

This chapter includes the theoretical part of the presents work, including the physical concepts and equations used to explain the results of this study.

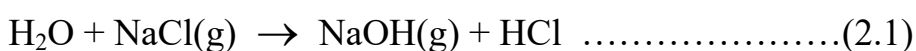
## 2.2 Mechanism of Hot Corrosion

The purpose of the hot corrosion analysis is to learn how metals can rapidly corrode with the surrounding medium at high temperatures, how to regulate the reaction or how to protect the metal from collapse and, finally, how metals are chosen for use in high temperature applications [91]. The strength of the heat purity of the fuel, the air quality required for the combustion process, the composition of the alloys, the composition of the gases, the composition of the sediment and the temperature. Compared with corrosion in the atmosphere, corrosion becomes more severe when the precipitate is in a fluid state [92]. For high-rate corrosion reactions, liquid deposits are usually required on the metal surface [93].

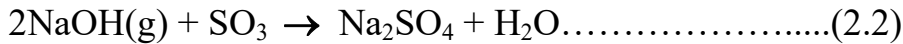
For heavy fuel there are many elements primarily responsible for corrosion and the three most critical elements (sulfur, vanadium, and sodium). Sodium is present in liquid fuels, while sulfur is mainly found in fuel oil and iron.

The most polluting mineral wastes are sulfur, oxygen and alkaline compounds, which also accumulate sediments [95].

$\text{Na}_2\text{SO}_4$  is a common compound in hot corrosion reactions. Sodium is found in either sodium vapor chloride or sodium hydroxide, as shown in the following relationship [96]:



$\text{SO}_3$  can react with sodium hydroxide in fuel gasses to form  $\text{Na}_2\text{SO}_4$ ,  
condensing as:



When porphyries are burned, vanadium oxides ( $\text{VO}$ ,  $\text{V}_2\text{O}_3$ ,  $\text{VO}_2$ , and  $\text{V}_2\text{O}_5$ ) are produced.  $\text{V}_2\text{O}_5$  can mainly be obtained under high temperature and oxidation conditions. Numerous studies have shown that Sodium metavanadate ( $\text{Na}_2\text{O} \cdot \text{V}_2\text{O}_5$ ) is caused by interactions between sodium sulfate and vanadium pentoxide. These compounds dissolve the layer of iron oxide, because it has a weak melting point, then it hits the carbon steel surface itself [97, 98]. The following equations describe sodium sulfate interactions with vanadium pentoxide[99]:



Table (2.1) displays some vanadium with a higher melting point and Sodium compounds which can corrode tubes made of carbon steel[99].

Table 2.1: Low melting point for some vanadium and sodium compounds [87].

Substance	Formula	Melting point ( $^{\circ}\text{C}$ )
Sodium sulfate	$\text{Na}_2\text{SO}_4$	880
Vanadium pentoxide	$\text{V}_2\text{O}_5$	675
Sodium metavanadate	$\text{Na}_2\text{O} \cdot \text{V}_2\text{O}_5$	630
Sodium pyrovanadate	$2\text{Na}_2\text{O} \cdot \text{V}_2\text{O}_5$	640
Sodium orthovanadate	$3\text{Na}_2\text{O} \cdot \text{V}_2\text{O}_5$	858
Ferric Oxide	$\text{Fe}_2\text{O}_3$	1565
Ferric orthovanadate	$\text{Fe}_2\text{O}_3 \cdot \text{V}_2\text{O}_5$	855
Ferric metavanadate	$2\text{Fe}_2\text{O}_3 \cdot 2\text{V}_2\text{O}_5$	860

---

Two types of hot corrosion may be distinguished according to temperature [100] :

1. **Hot corrosion at high temperatures** is also called, (HTHC) (High Temperature Hot Corrosion). This corrosion occurs at a temperature range (800-1000 °C). It is accelerated due to the process of oxidation that occurs as a result of exposure to combustion gases. (HTHC) occurs as a result of sodium salt reaction in the air that enters the fuel with contaminants to form sodium sulfate, and it may form ( $V_2O_5$ ) compound, then the material ( $Na_2SO_4$  and  $V_2O_5$ ) will be deposited as a liquid precipitate along the alloy surface and this precipitator with molecular pressure ( $SO_2 / SO_3$ ) formed as a result of burning gases will cause the oxide protective layer to melt and prevent its formation again..
2. **High corrosion at low temperatures**, (Low Temperature Hot Corrosion) (LTHC). This corrosion occurs when the gas turbine machines are running at low capacity and at a temperature range (600-800 °C). That is, at a temperature below the melting point of sodium sulfate (840 °C), as in this small degree it condenses on the surface, a liquid compound such as ( $Na_2SO_4 + NiSO_4$ ) which is less than (575 °C) melting point and penetrates into the oxide layer on the surface, leading to the formation of some sites by clicking and thus to the start of hot corrosion.

### 2.3 Deposition Mechanisms

Due to higher temperatures deposits will accumulate on the surface of the metal to four physical methods [101]:

1. **Molecular Diffusion:** Diffusion occurs when the molecules are less than 100 nanometers, and the molecules act as gas molecules.

2. **Brownian motion**, In this case, the particle size is between (0.1-1 micrometer) and the particles take a random path when pushed by the gas molecules.
3. **Turbulent diffusion**, This form occurs when the particles are between (1 to 10  $\mu\text{m}$ ) and enter the undulating region directly across the surface, taking the kinetic energy from the gas streams and allowing it to pass through the thin layer adjacent to the surface area.
4. **Initial impaction**, in this case, particles greater than (10 $\mu\text{m}$ ) enter the boundary or turbulent field as they gain kinetic energy from the main flow of gas, or take an independent path that does not depend on the direction of the gas spread.

Figure 1.2 shows the particle furnace boiler precipitation rate when the velocity of the gas flow is around (30 m / s). Particles with a size of (0.1-1 micrometer) are the least suitable for precipitation. Accumulation of ash deposits in order to form a mass of deposits depends not only on the particle size but also on the particle adhesion power. Unlike ( $\text{SiO}_2$ ) it is more suitable for hard surface adhesion since it does not melt, it can have a high surface viscosity.

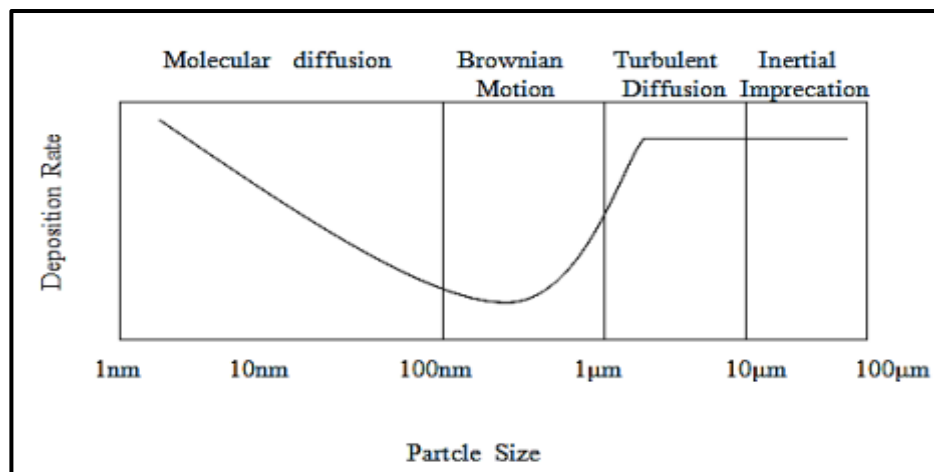


Figure 2.1: The precipitation rate of particles in a steam boiler [101].

---

## 2.4 Thermal Barrier Coatings and Thermal Grown Oxide

The thermal barrier coatings (TBC) system is composed of a layer of ceramic top and a layer of metal bonding on the top of the substrates. The MCrAlY layer provides a good match between the ceramic top layer and the sublayer for the thermal expansion and also protects the bottom layer from oxidation and hot corrosion. The transportation of oxygen through the upper layer to the bonding layer may occur at elevated temperatures through micro cracks and pinholes interconnected within the upper layer [102]. Thus, an oxidizing layer may form between the bonding layer and the upper layer called the thermally grown oxide (TGO). Due to growth of TGO layer during oxidation, the (TGO) layer plays an significant part in TBC failure. During the oxidation process, the thickness of TGO, accompanied by stress development, may increase at the front of the bond layer. This stress causes loosening of the coating at the bonding layer interface [103, 104]. Studies have also shown that TBC stress increases with an increase in the TGO layer. The thicker TGO layer therefore has more pressure than the thinner layer [105, 106]. Studies have shown that the TBC system with an MCrAlY bond layer and a double ceramic layer ( $\text{Al}_2\text{O}_3$  / YSZ), when exposed to high temperatures, will form,  $(\text{Ni} (\text{Cr}, \text{Al})_2\text{O}_4$  (as spinel) and NiO) when it is exposed to high temperatures of up to 1000 °C [105, 106]. Previous studies have shown that these two oxides ( $\text{Al}_2\text{O}_3$  / YSZ) are ideal locations for cores to start cracks, this results in the top layer of the coating isolated from the bond layer. So the TBC systems' durability is negatively affected by mixed oxides due to the pressure produced by the rapid increase in local volume [105].

Previous studies have also recorded that two-layer TGO ( $\text{Al}_2\text{O}_3$  / Harmful oxides mixed) have the greatest radial pressure, the maximum axial maximum pressure difference is approximately 5 times higher than

the one-layer, TGO ( $\text{Al}_2\text{O}_3$ ), and that the maximum axial maximum pressure difference is around ten times that of a single-layer TGO ( $\text{Al}_2\text{O}_3$ ), hence, two-layer TGO has more pressure than single-layer TGO [105,106].  $(\text{Cr,Al})_2\text{O}_3, \text{Ni}(\text{Cr,Al})_2\text{O}_4$  and  $\text{NiO}$  are called  $(\text{Cr,Al})_2\text{O}_3 \cdot \text{Ni}(\text{Cr,Al})_2\text{O}_4 \cdot \text{NiO}$ , or just abbreviated as, chromia, spinel and nickel oxide (CSN). Studies have proven that CSN formation is the result of superposition heterogeneity in the TBC system during air plasma spraying. It was also noted that  $\text{Ni}(\text{Cr, Al})_2\text{O}_4$  and  $\text{NiO}$  could not be completely removed from the TGO ( $\text{Al}_2\text{O}_3$ ) layer [103-105].

The most important finding of the research mechanism is that the continuous  $\text{Al}_2\text{O}_3$  layer can develop at the interface of the ceramic layer with the bonding layer in TBC systems that are coated with plasma under low oxygen pressure [103]. This continuous but thick  $\text{Al}_2\text{O}_3$  (TGO) coating can act throughout heat treatment as anti-diffusion barrier to CSN formation [106]. Further work is therefore investigated to obtain techniques for producing a thick, during oxidation, continuous and thin layer of alumina on bond layer (NiCrAlY). Figure (2.2) shows a schematic diagram of the TBC coating barrier layer showing individual sub layers [107]. Figure ( 2.3) shows the most significant factors that contribute to the TBC failure [108].

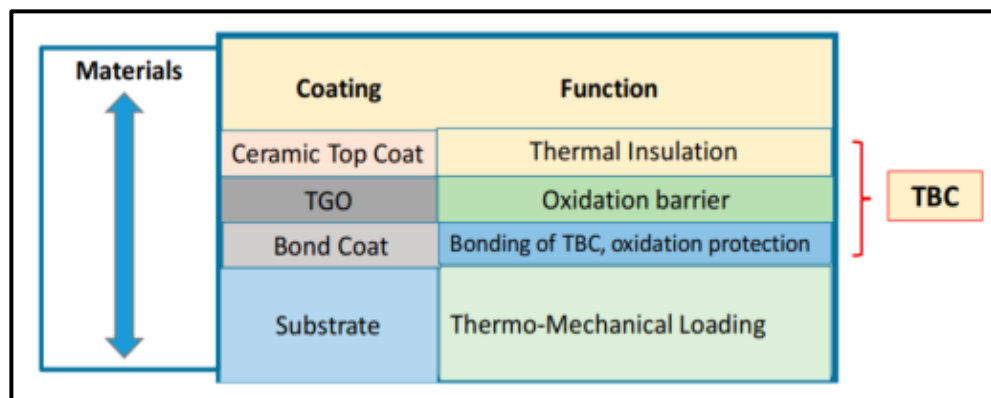


Figure 2.2: Schematic diagram of TBC barrier coating construction layers and individual sub layers [107].

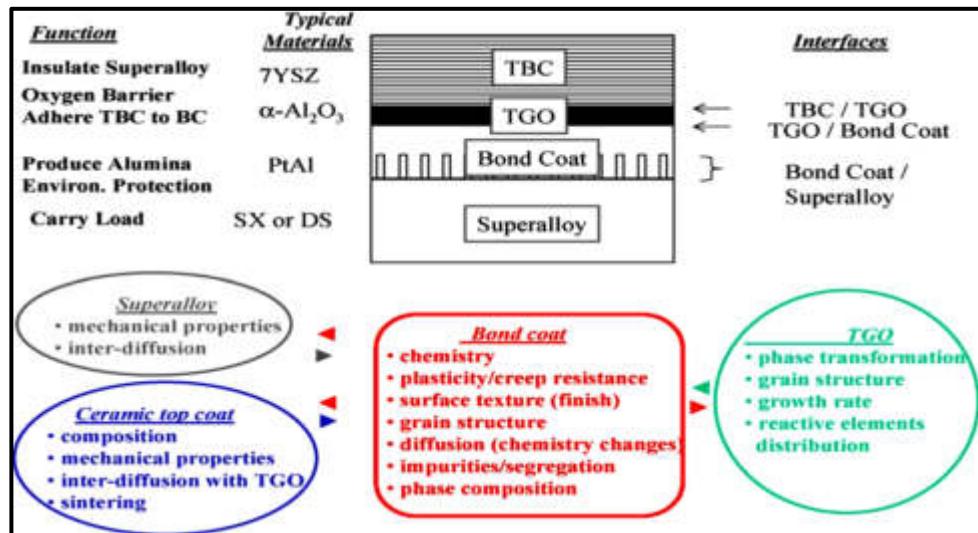


Figure 2.3: Schematic illustration of the factors contributing to failure mechanisms of TBCs [108].

## 2.5 Basic conditions for the coating layer

One of the most important means of technological development in recent decades is the use of different coating methods to make the material resistant to different environmental conditions, and there are many methods and materials used in the coating process, but the choice of any of them depends on a prior knowledge of the behavior and properties of each of them. It must be present in the layer of coating [109, 110]:

### 2.5.1 Corrosion Resistance

Coating elements should be carefully chosen so that they are capable of forming a protective oxidic shell, and these protective shells are  $\text{Al}_2\text{O}_3$  and  $\text{Cr}_2\text{O}_3$ . The  $\text{Al}_2\text{O}_3$  layer is considered to be one of the best oxidation-resistant oxidation layers characterized by low heat conductivity and low spread, and also characterized by its rapid formation in front of the other oxidative cortex. [111].

### 2.5.2 Erosion Resistance

Erosion occurs as a result of collisions with particles or small granules in the fluid (such as gases and liquids) with the surface of the working

component and in order to reduce the resultant damage a strong ductility of the coating layer must be present. Instead, if any shock happens, it may lead to the fracturing of the coating layer, it is desirable that the paint layer be free from any flaws or holes that may be the starting point for corrosion degradation[112].

### **2.5.3 Thermal Stability**

The coating layer must be stable under any of the working conditions in it. Therefore, the coating elements must remain inside the coating layer to reduce its loss as a result of the diffusion process into the alloy, because its diffusion may weaken the required mechanical properties [113].

### **2.5.4 Mechanical Toughness**

The coating layer must be capable of withstanding all stresses that may occur on the surface of the alloy during operation. Because the presence of weak areas or the presence of cracks in the paint leads to a failure of the painted part faster than the other unglazed parts because they will be centers for stress gathering (stress concentration), and these stresses can be created by creeping or thermal fatigue and can be created. The consequence of thermal fatigue is that there is not a very significant difference in the coefficient of thermal expansion between the coating layer and base alloy [114].

### **2.5.5 Adhesion**

Many coating processes, especially diffusion and thermal methods, require the occurrence of a diffusion process between the coating elements and the base alloy, resulting in a good bonding between them, which gives the coating layer the ability to avoid separation from the alloy due to any thermal or mechanical stress. [115].

## 2.6 The Forming Mechanism of Thermal Spray Coatings

The coating characteristics produced by the thermal spraying process are dependent on the exact composition of the coating layer. In order to know the properties of the coating and its development, its precise composition needs to be understood, and this in turn depends on the composition mechanism of the. Hence it is the connection between the coating process information and the coating properties [116]. The coating layers consist of a process of thermal spraying from the collision of the molten drops to the substrate, flattening it and then freezing it, giving a lenticular structure, which is the dominant characteristic of this type of coating. Drops (formerly frozen) that tend to bounce off the base and thus weaken the coating may be observed [116]. Because spraying occurs in the air, a thin oxide layer is formed around the molten drops, and this affects the coating bond [117].

The spraying parameters which affect the coating process must therefore be regulated from the complete dissolution of the coating material, the speed of the droplets, the temperature and the size of the coating material [117]. Figure (2.4) shows the Schematic diagram for forming a thermal spray coating.

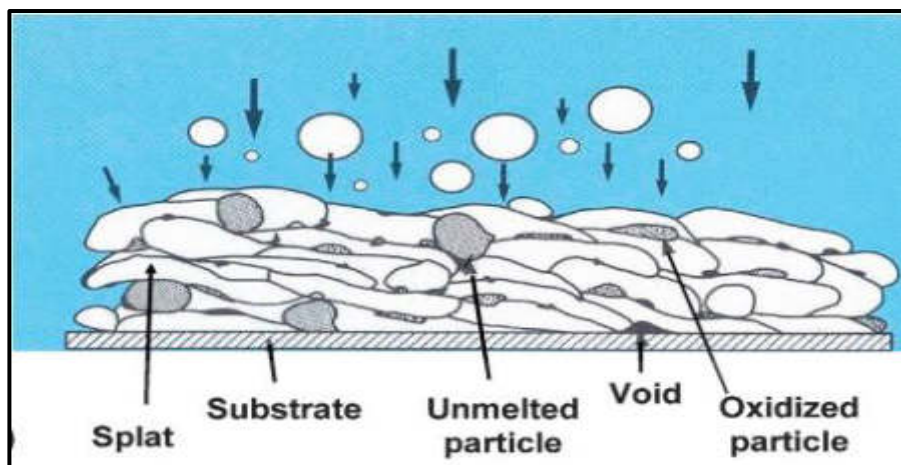


Figure 2.4: Scheme for the formation of a thermal spray coating[117].

Regardless of the oxide fragility, the oxide layer covering the drop will break on the surface when the drop reaches the substrate [117]. With the drops falling continuously on the base and accumulating on top of each other at a rate of up to one million drops each second (depending on the region to be sprayed and the pace of the gun movement), thermal coating layers are formed with a thickness [118]. Figure (2.5) represents the collision of the molten drop with the base.

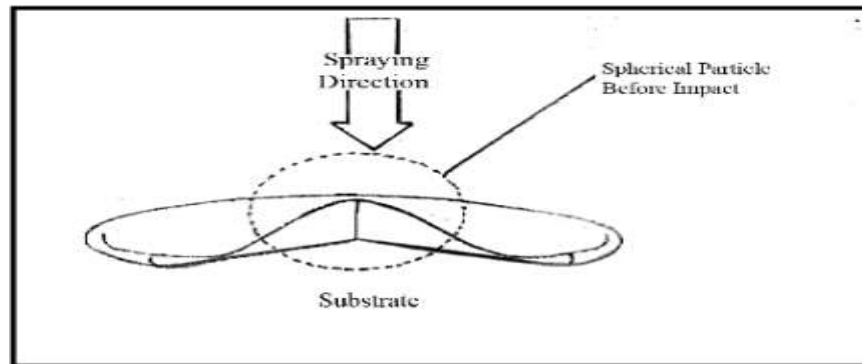


Figure 2.5: Collision of the drop with the base [118].

The process of effect on the base of the drop of the molten coating is summed up by:

As shown in Figure (2.6) when the drop hits the base surface it will flatten and flow in the form of a circular disk. The first drop in contact with the substrate occurs in the heart region (Core region) at the time of collision, then the heat flows to the base and the non-freezing liquid flows from the drop parallel to the surface of the substratum, away from the core and eventually solidifies in the form of an elevated frame [117, 118]. In case the drop collides with the base at a very high speed, the fluid flowing from the core will then be lost, spreading out into several tiny droplets, which means that the drop here takes various forms as shown in figure [119].

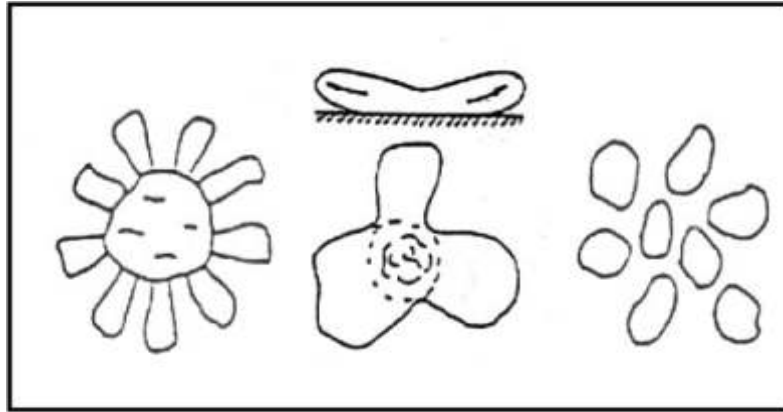


Figure 2.6: Shapes of drops upon impact [119].

## 2.7 Preparation methods and roughing the substrate surface

An important part of any coating process is setting up the substrates. Formatting includes cleaning of samples from impurities, oils and greases, and these impurities represent the residue of roughing processes such as granules suspended on surfaces of the granular process or parts dispersed by grooving and teething.

The cleaning process is carried out using suitable solvents, as well as using ultrasonic cleaning machines. It should also be well dry by using special drying ovens in addition to providing the appropriate roughness to generate a high degree of bonding between the coating and the substrate [120].

Substrate surface roughening is an important step in obtaining a high adhesion coating. The aim of the surface roughening process is to obtain a larger surface area as well as to get rid of the oxide layers, and other contaminants at the surface with the roughing process. Burrs are obtained that tear the formed oxide layer, which helps it to flow easily on the surface, and to obtain foci surrounding the flowing minutes, thus increasing the contact area, and improving the heat transfer that leads to a localized spread increases the adhesion of the coating to the substrate [120].

Figure (2.7) shows the effect of surface protrusions on tearing and flowing of the molten drop.

The greater the contact area between the droplet and substrate surfaces, the greater the possibility of chemical bonds being formed by the transfer of electrons [120].

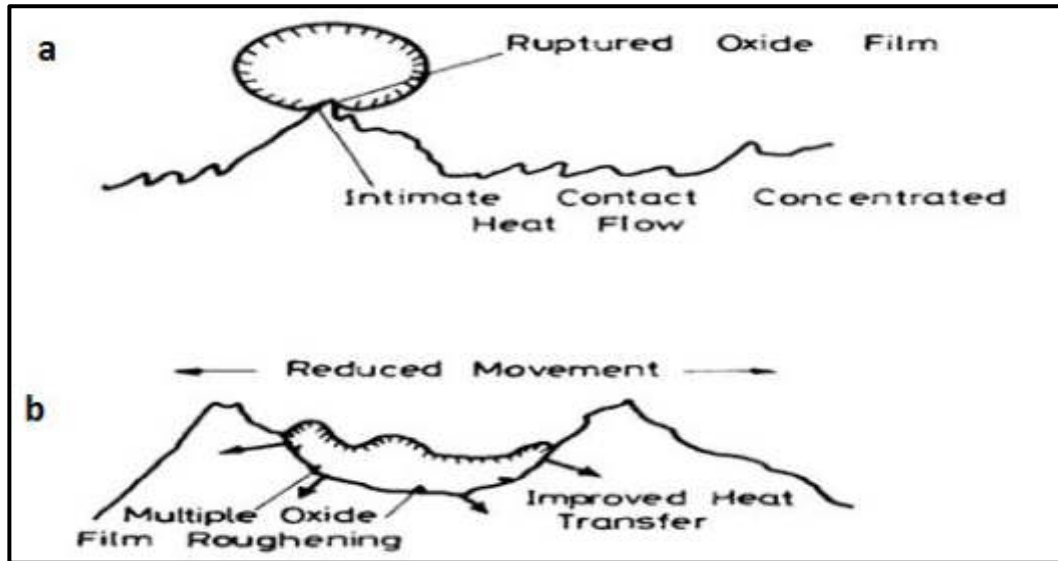


Figure 2.7: The effect of surface protrusions on tear flow rupture[120].

(a): The oxide layer formed on the drop is torn as it collides.

(b): A focus of the rough base protrusions surrounds the flowing drop.

Among the most important methods of roughing are:

### 2.7.1 Grit Blasted Method

It is a common method used for its ease of operation and its low cost. This method is widely used in preparing surfaces of thermal spray samples, especially for large parts.

This method is based on pushing granules with sharp edges, and high hardness such as silicon carbide, aluminum oxide, or Iron slag with compressed air to the substrate to be roughing . This process depends on several factors, the most important of which are the air pressure, the distance between the substrate, and the exit hole of the granules [121].

This method has been adopted in roughing up this research samples for their availability, ease and low costs.

### **2.7.2 Rough Threading**

The principle working of this method is roughing the surface with a sharp object that works on grooves events with a depth of (0.7 - 0.9 mm) and a number of about (10-15) grooves per centimeter, and at a cutting angle ( $50^{\circ}$  -  $70^{\circ}$ ) of cylindrical parts. This method is usually used to create cylindrical substrate, and do not use to configure large slitting rules to slow them down [121].

### **2.7.3 Groove Method**

This method differs from its predecessor by the fact that the streak ends formed in this way are arc-shaped, that is, the probability that cracks will form is weaker. Therefore it can be used to prepare heavy surface surfaces and parts that are subject to high fatigue stresses [120,121].

### **2.7.4 Arc Methods of Preparation**

This method is used to rough the high hardness bases that cannot be roughing by the previous methods. The basis of the work of this method is to shed an electric arc on the surface of the substrate to be roughing. This arc works to melt the base and harden it quickly, thus obtaining an irregular surface.

The process is done by shedding the potential difference on the substrate that is attached to one of the electrodes, and the second end is a brush of copper wire moving quickly on the surface of the substrate, and thus this process results in rough surfaces of the molten metal protrusions [121].

## 2-8 Structure Properties.

X-ray diffraction technology is a fundamental source of reliable knowledge about the crystalline structure, because the general theory of diffraction relies on the phenomenon of interference that occurs when the movement of any wave is spread in a variety of centers and the effect is either constructive or destructive interference. Bragg has succeeded in imposing a simple crystal structure model by which the direction of X-ray diffraction from the crystal can be known after it has fallen on it, and this model states that the different levels of the crystal atoms can reflect X-rays [122, 123]. The mathematical formula is written as follows for Bragg's law [124]:

$$n \lambda = 2 d_{hkl} \sin \theta_B \dots\dots\dots (2-6)$$

where: (n) is positive integer ( diffraction order).

( $\lambda$ ) is the wavelength of the incident X-ray beam.

( $\theta_B$ ) Bragg's diffraction angle of the XRD peak.

(d) the inter planar can be determined.

Bragg's Reflection condition is that the wavelength has miller co-ordinates and fallen rays reflected from a level with miller co-ordinates ( $h k l$ ) smaller or equal to twice the ( $d_{hkl}$ ) between two consecutive crystal levels and, as shown in Figure (2.8), the condition is that [125].

$$\lambda \leq 2d_{hkl} \dots\dots\dots(2-7)$$

Crystalline semiconductors may be distinguished from randomness by studying X-ray diffraction patterns. The diffraction pattern in monocrystalline materials is in the form of strong bright points, and in polycrystalline materials in the form of thin rings with strong, interlaced focused illumination and random materials in the form of rings weak and illuminated, focused [125].

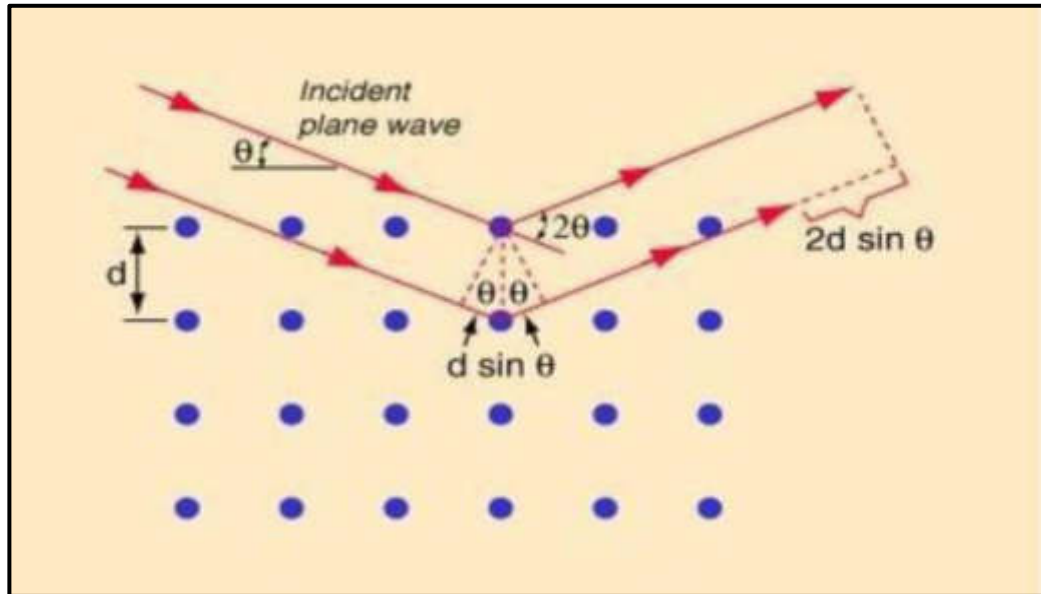


Figure 2.8: The crystal levels of Bragg's Law [125].

## 2.9 Structural Parameters

### 2.9.1 Lattice constants ( $a_o, b_o, c_o$ ) of hexagonal structure.

The hexagonal structure lattice constants ( $a_o = b_o, c_o$ ) can be determined according to the following equation [126]:

$$\frac{1}{d_{hkl}^2} = \frac{4}{3} \left[ \frac{h^2 + hk + k^2}{a_o^2} \right] + \frac{l^2}{c_o^2} \dots\dots\dots(2.8)$$

### 2.9.2 Crystallite average size ( $D_{av}$ )

The average crystallite size may be calculated in two ways:

#### 1. Scherrer method

The average crystallite size of the alumina nanoparticles can be calculated using the scherrer method as follows: [124].

$$D_{av} = \frac{K\lambda}{\beta \cos\theta_B} \dots\dots\dots(2.9)$$

Where  $K$ : is the shape factor ( $K = 0.9$ ),  $\lambda$ : the X-ray wavelength falling on the target,  $\beta$ : Full Width at Half Maximum (FWHM) measured in radians, and  $\theta_B$ : the diffraction angle of Bragg.

## 2. Williamson-Hall method

This measures the crystallite size, which does not depend only on the full width at half maximum, as in the Scherrer method, but also on compliance (Strain), i.e. (FWHM) resulting from crystallite size and strain, as in the following equation [127]:

$$\beta_{hkl} = \beta_D + \beta_S \dots\dots\dots(2.10)$$

$\beta_{hkl}$ : Total full width at half maximum,  $\beta_S$ : Full width due to micro strain), and  $\beta_D$  : Full width due to crystallite size.

From the Scherrer equation it depends on  $(1 / \cos\theta_B)$  whereas the Williamson-Hall equation depends on  $(4S \tan\theta_B)$ , and  $(S \approx \beta_S / \tan\theta_B)$  and when replacing them in equation (2.10) we get:

$$\beta_{hkl} = (K\lambda / D_{av} \cos\theta_B) + 4S \tan\theta_B \dots\dots\dots(2-11)$$

Multiplying a value  $(\cos\theta_B)$  both of sides of this equation:

$$\beta_{hkl} \cos\theta_B = \left( \frac{K\lambda}{D_{av}} \right) + 4S \sin\theta_B \dots\dots\dots(2-12)$$

The crystalline size ( $D_{av}$ ) and the micro- strain can be determined when drawing  $(\cos\theta_B)$  with  $(4\sin\theta_B)$ , for all the resulting peaks and for all the prepared patterns [127].

### 2.9.3 Dislocation density

The dislocation intensity represents the number of dislocation lines in the crystal which cross the area of the unit [128]. It represents the ratio of the total length of all dislocation lines to the crystal size, and also the dislocation density ( $\delta$ ) actually results from the crystalline volume is determined using the following equation : [128,129].

$$\delta = \frac{1}{D_{av}^2} \dots\dots\dots(2.13)$$

### 2.9.4 Texture Coefficient (TC)

In polycrystalline compositions with a so-called Texture Coefficient (TC) the preferential orientation of a specific level within the crystal can be described because its value is higher than one or more confirms that the direction of the crystal growth of the preferred levels (most) is in this direction, but less than one is polycrystalline. Thus, the improvement of the crystalline growth of matter is related to the value of this factor in multiple directions and it was described according to the following relation (Barrett and Massalski) [130].

$$TC_{hkl} = \frac{\frac{I_{hkl}}{I_{0hkl}}}{N^{-1} \sum_n \left[ \frac{I_{hkl}}{I_{0hkl}} \right]} \dots\dots\dots(2.14)$$

$I_{hkl}$ : Practically measured intensity.

$I_{0hkl}$ : The standard intensity found in the (ICCD) card.

$N^{-1}$ : Represents the number of peaks evident in the diffraction pattern.

### 2.9.5 Specific Surface Area (SSA)

Specific surface area can be defined as the area through the mass unit, and its unit of measurement ( $\frac{m^2}{g}$ ) and knowing its value is very important for nanomaterial's because the surface of these materials becomes large relative to their size, and in material science the specific surface area is used to determine the quality of materials and their properties, and also to know the interactions that occur on the surface such as surface smoothing and adsorption [131, 132]. The specific surface area is related to the surface density (surface area through volume unit) by the following relation:

$$SSA = \frac{S_v}{\rho} \dots\dots\dots(2.15)$$

$S_v$ : it's surface density (surface area through volume unit) is defined and can be derived from the following relation:

$$S_v = K_{sv} / D_{av} \dots\dots\dots(2-16)$$

$K_{sv}$ : a fixed quantity called the form factor and equal to (6) in relation to the spherical shape and by substituting the equation (2-16) in the equation (2-15), the relationship can be obtained by measuring the specific Surface Area as follows [133]:

$$SSA = 6 \times 10^3 / D_{av} \cdot \rho \dots\dots\dots(2.17)$$

where is SSA: Specific Surface Area,  $D_{av}$ : Average Crystal size,  $\rho$ : Material Density.

## 2.9.6 Factors affecting X-ray diffraction

There are several variables that affect the materials' structural properties, and therefore a significant change in the X-ray diffraction pattern for them [134]. These factors include:

### 1- Effect of Temperature

Temperature effect is an important factor in determining the crystal structure of polycrystalline materials, especially nanostructures, by raising grain size and decreasing granular boundaries in most cases, this increases the crystallization of the material and the lack of defects within it, and gives the atoms sufficient energy to re-arrange the material within the crystal lattice. The crystallization of the material means a clear increase in the intensity of the vertices attributed to the levels, and it was found during the recent software used for calculations that this increase is accompanied by a decrease in values (FWHM with a deviation to the values), less confirming that temperature plays a role in increasing the distance between

crystalline levels because the relationship between  $(d)$  and  $(\sin\theta_B)$  is reversed as shown in Bragg's law [135].

## 2- The effect of Nanostructures

Recent studies have shown the results of (XRD) that there is a clear difference in the form of diffraction pattern for nanostructures than for bulk materials (especially when we reach very small values for granules that are estimated to be less than (20 nm) [95]. On the contrary, the (XRD) pattern of most nanostructures, such as rods, tubes, wires and other nanoscale structures, has not changed much from what is produced to bulk materials [136].

### 2.10 Mechanical properties

Mechanical properties are the material characteristics that demonstrate the mechanism of their operation and operation based on the loadings and are used to evaluate the material's estimated lifetime and degree of efficiency in the production process. The mechanical properties also assist the materials to be classified and their identity given. Where the mechanical material properties are defined as changeable, not fixed, as they vary due to the surrounding situation, the room temperature changes. For example, causes a change in the properties of mechanical materials, so tests are conducted to determine the properties at a particular temperature [137, 138].

#### 2.10.1 Surface Hardness Test

One of the material's important mechanical properties is surface hardness and is defined as the material's resistance to Indentation, and is also known as the material surface 's resistance to the plastic deformation

resulting from scratching, cutting or penetration. The hardness value gives evidence of the structure's resistance , durability, and cohesion. The importance of hardness is emphasized unless it gives a clear picture of the results of the changes that occur on the material's surface as a result of thermal or chemical treatment of these surfaces. The most important methods used to measure surface hardness [139]:

1. Vickers Hardness
2. Brinell Hardness
3. Rockwell Hardness
4. Shore (A,D) Hardness
5. Shore Scleroscope Hardness
6. Knoop Micro Hardness

### **2.10.2 Vickers Hardness Test**

The Vickers method allows for the measurement of the hardness of thin surface layers resulting from carbonisation, nitridization or treatment. This can also calculate the hardness of highly hardened materials and articles with a cross section in the material being tested, and the low pressure is provided, the hardness is determined by the pressure of the four-phase diamond pyramid at its highest angle of  $136^\circ$  under the impact of the load (5, 10, 20, 30, 50 , 100 or 120 kg), as shown in the figure(2-9) [140]. The resulting impact area is then determined by measuring the diameter by means of a microscope mounted on the device, or that this effect appears magnified on the device screen, where the effect diameter can be accurately measured or the device is given the value of the vickers hardness number directly via a special scale [141]. The number of the Vickers hardness is calculated using the form [142]:

$$\text{Vickers hardness number} = \text{V. H. N} = \frac{2 \cdot P \cdot \sin\left(\frac{\theta}{2}\right)}{D^2} \dots\dots\dots(2.18)$$

$$\text{V. H. N} = 1.854 \times \frac{P}{D^2} \dots\dots\dots(2.19)$$

Where **D**: Impact diameter, **P**: The load of the test.

This approach has the following characteristics [142]:

1. The Vickers number is fixed for a single metal, irrespective of the loads that influence it.
2. Vickers test will achieve an accurate value for the number of hardnesses and a full description of the hardness of the metal being tested using a small tool and small impressive loads. This test can also be used with a small diamond pyramid to determine the hardness of metals that are not suitable for testing by (Brinell) method up to 1.0 mm thickness.
3. This test is used in works requiring accurate mineral tests, regardless of form , size, or hardness, and is an important test in the work of comparison and analysis.

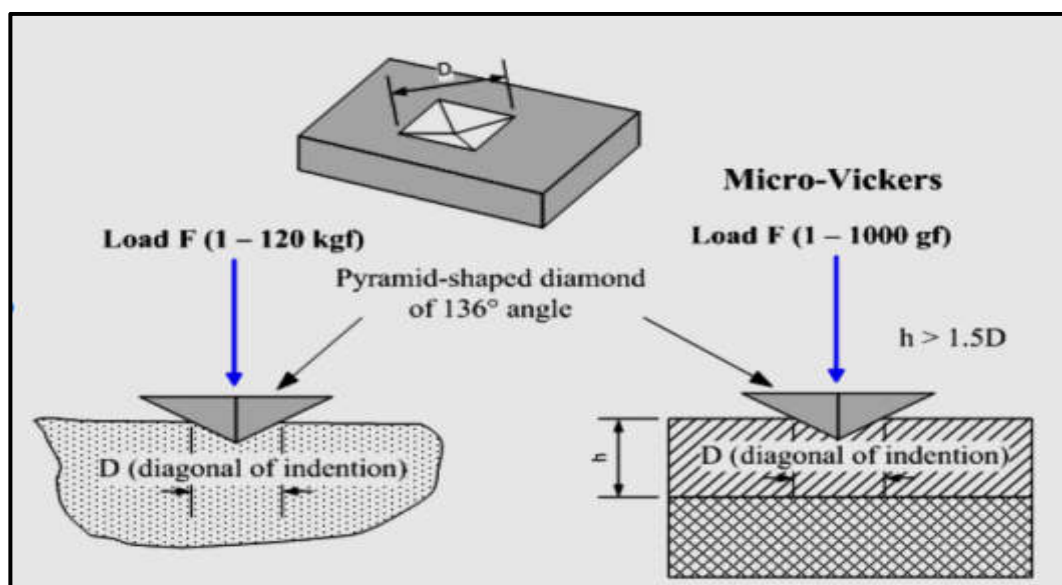


Figure 2.9: Schematic of Vickers hardness test method [142].

## 2.11 Corrosion Rate

The rate of corrosion may be defined as the rate at which the metal is decomposed in a given environment. [143]. Or the amount of annual corrosion in the thickness may be defined. The corrosion rate depends on conditions such as the environment and the type of metal used. There are many methods used for measuring the corrosion rate, such as [144]:

1. Loss of weight per unit area and time of day.
2. Density of corrosion current used for polarization testing.

### 2.11.1 A Method of Weight Loss

The method of weight loss is one of the oldest and most common methods used to calculate the corrosion rate. Corrosion rates are calculated by taking the difference in sample weight before and after exposure to corrosion during the specified time period and the known sample area. [145]. The corrosion rate is determined at different temperatures using the relation [146]:

$$C_R = \frac{\text{Weight loss (g)}}{\text{Area (m}^2\text{)} \times \text{Time (day)}} \dots\dots\dots(2.20)$$

$C_R$ : corrosion rate ( $\text{g/m}^2 \cdot \text{day}$ ), and  $\text{gmd}$  symbol. Other units can be used to measure the corrosion rate, such as  $\text{mpy}$  (milli- inch per year),  $\text{mdd}$  ( milligrams per square dicimeter per day), etc.

### 2.11.2 Coating Efficiency (% IE)

The coating efficiency of a specific sample is calculated in order to know the performance of coating and shall be calculated from the following relation [147]:

$$\%IE = \frac{C_R^o - C_R^I}{C_R^o} \times 100 \quad \dots\dots\dots(2.21)$$

$C_R^o$ : Corrosion rates when no coating layers are present.

$C_R^I$ : Corrosion rates where coating layers are present.

### 2.11.3 Activation Energy

The term (Activation Energy) denotes the minimum amount of energy required to cause a chemical reaction. It is referred to as  $E_a$ , and is measured using a kJ / mol scale. In 1889 the Swedish scientist (Svanet Arrhenius) was coined. The time path for chemical reactions explains the activation energy (Chemical Kinetics)[148]. This equation gives the reaction rate a constant magnitude and its dependence on temperature. The activation energy of the corrosion process at high temperature can be measured using the Arrhenius equation [149]:

$$CR = A \text{ Exp} \left( \frac{-E_a}{RT} \right) \dots\dots\dots(2.22)$$

The linear Eq-form. (2.22) Available as:

$$\ln CR = \ln A - \frac{E_a}{RT} \dots\dots\dots(2.23)$$

A: is the frequency factor.

R: is a gas constant =  $8.314 \text{ J} \cdot \text{K}^{-1} \cdot \text{mol}^{-1}$ .

$E_a$ : is the activation energy.

T: is the absolute temperature.

It is possible to plot Eq 2.23 as the natural wear rate logarithm  $\ln (CR)$  versus reciprocity at absolute temperature ( $1 / T$ ) as shown in Figure (2.10). Arrhenius equations line slopes and intercepts can be used to approximate the values of the activation energy ( $E_a$ ) and frequency factors (A) respectively.

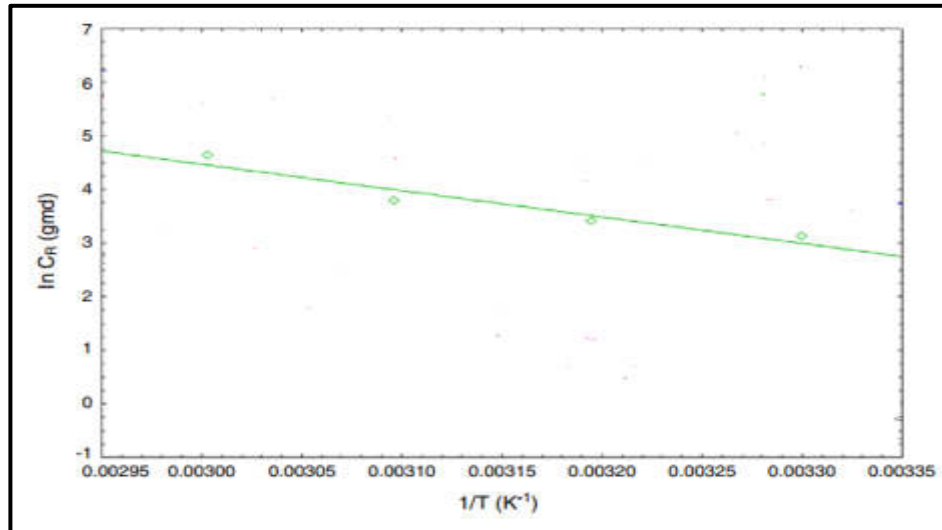


Figure 2.10: Arrhenius plots [147].

## 2.12 Field Emission Scanning Electron Microscope (FESEM)

Nanotechnology led the development of a modern electron microscope, requiring not only greater accuracy, but more sample details too [150, 151].

FESEM, is a tool for the imaging of surfaces in high resolution. It uses imaging electrons as frequently as visible light is used in optical microscopy. One of FESEM's major advantages is that it has a magnifying power ( $> 500KX$ ) [152]. The resulting images are in black and white colors from this electronic microscope, since they are not based on light waves, but instead use electrons. Some of the most important advantages of FESEM is that higher resolution imaging can be done than SEM with very low acceleration voltage, as shown in Figure (2.11) [150]. It increases the detection of very fine surface structures, sensitive materials to electron beams, and non-conductive materials. Using a high-energy electron beam, FESEM visualizes the sample surface by point scanning. Electrons interact with the sample atoms to generate signals that include surface terrain information, structure information and other properties.

The electron gun is designed to provide a large and steady current in a narrow beam. There are two types of emission sources: heat emitters, and ground emitters. The principal distinction between (SEM) and (FESEM) is the emitter type [153].

Typical Major Applications (FESEM) [150- 153]:

1. Microscopic measurement feature.
2. Evaluations of corrosion.
3. Measurements of striations for high-cycle fatigue fractures.
4. Evaluations of coating.
5. Characterization of very fine features of the specimen.
6. Characterization of fractures for polymers, and very small materials.
7. Examination of pollution of the soil.
8. Examination of small part material.
9. Analysis of laser and welded resistance.
10. Printed, integrated analysis of the circuits.
11. Studies of a microstructure.

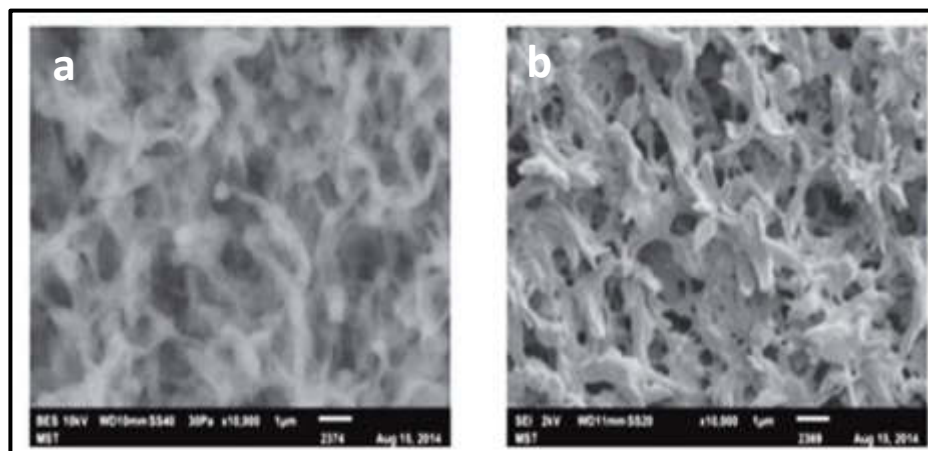


Figure 2.11: Images under the same conditions by, a: SEM, b: FESEM [153].

---

## 2.13 Transmission Electron Microscopy ( TEM)

Transmission electron microscopy (TEM) is a tool that uses an electron beam to analyze and test samples at a time while a scanning electron microscope examines the sample surface and characterizes its surface properties. The transmission microscope is distinguished by the ability to penetrate the sample which located in the electron beam direction from the electron radiation source. It is above the location at which the sample was placed and accessed [150, 154], and this system works by generating electrons by heat emission where an accelerating voltage varying between (60-100 KeV) is applied and the accelerated electrons have energy regulated by the user as needed. The electron beam will then pass through the column of the vacuum microscope, a group of electromagnetic lenses along this column is focused on this beam, by blocking the dispersed electrons, the control holes along this column often control electron beam width. The electronic beam then enters the sample, resulting in an interaction between these electrons and the surface of the sample, where a portion of the falling beam called the effective beam, an electronic beam without deviation, is conducted and electronic bundles scattered and deviated from the atoms and molecules of the sample [150]. Using electromagnetic lenses and control holes, the electronic beam is then amplified, and obtained and projected as an image on a fluorescent monitor.

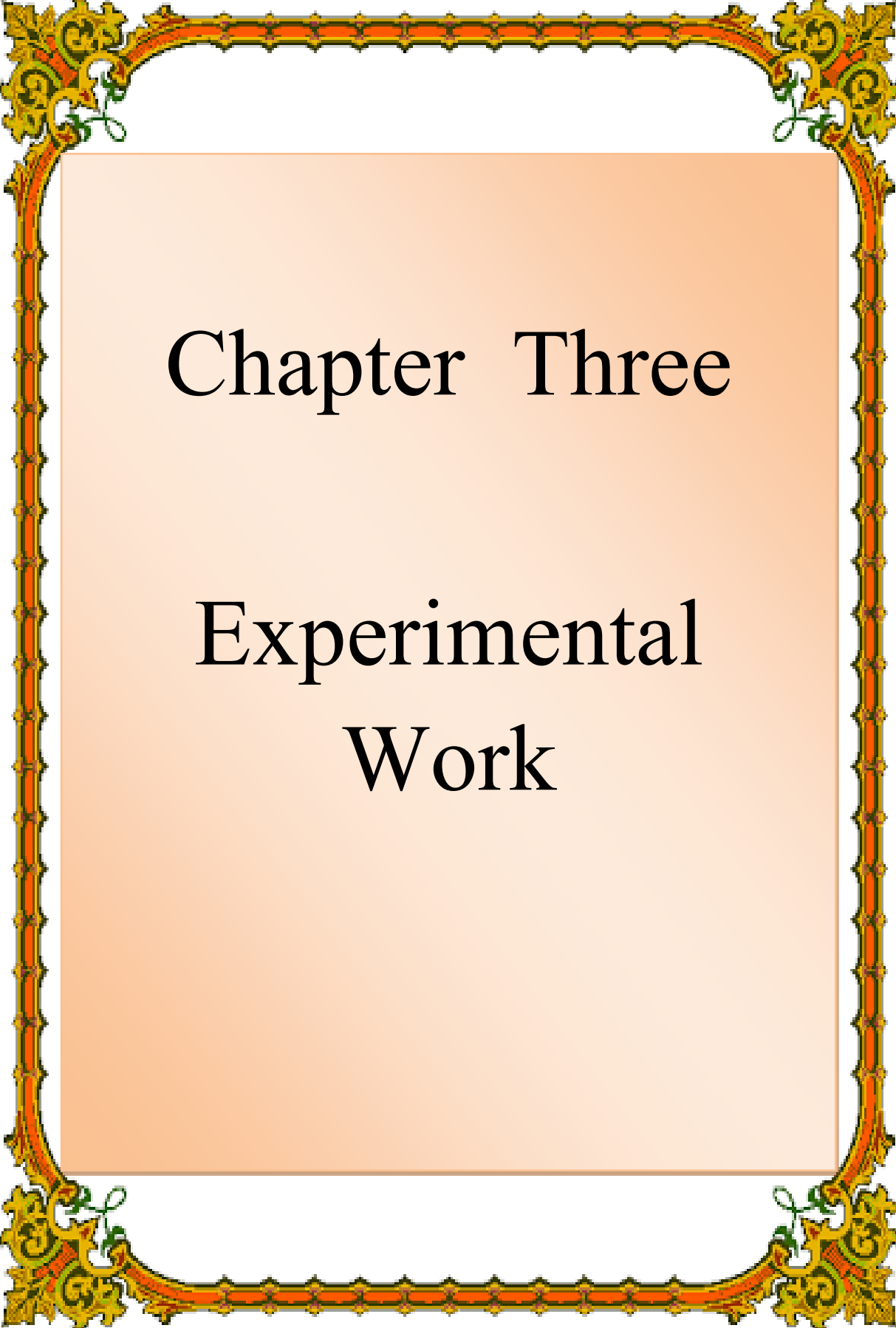
The resulting picture includes dark areas and luminous regions, depending on the type of sample and the type of elements found within, where the dark areas suggest that the electrons did not enter the screen from these areas, and this is due to absorption from the atoms of these regions or broad dispersion, and this means that the sample tends to contain heavy atomic elements (large atomic numbers) in those dark regions. As for the bright areas, they indicate that large numbers of electrons arrive in these

regions, Which means that the electrons did not suffer from any absorption or large dispersion of the atoms in those regions, suggesting that the sample in those areas appearing in the light contains elements of their atom light (possesses Small atomic numbers).

### **2.14 Energy Dispersive Spectroscopy (EDS)**

Energy Dispersive Spectroscopy is an analytical method used to analyze elements to determine the chemical properties of materials, and is one of the X-ray spectroscopy types.

The theory of this technique relies on the assumption that X-rays arising from the reciprocal influence of charged particles, such as a beam of electrons with the sample material, are distinct from the corresponding elements in the sample, such that the composition can be determined [155]. In other words, because each element has its own distinct atomic structure, the X-ray spectrum has a series of distinct peaks. The atoms must be irritated first to obtain the distinctive x-rays of matter. This is achieved by tossing matter with an electron beam, such as a scanning electron microscope, or an x-ray projector, as in the X-ray brilliance [156]. As a result, an electron is released from the internal atomic orbitals, and as a result of an electronic vacancy filling higher atomic orbitals an excitation and instability occurs. As electrons move from the highest atomic orbitals to the lowest, they emit X-rays with energy that corresponds to the difference in energy between the atomic orbitals. This energy difference is unique to all chemical elements [157].



# Chapter Three

## Experimental Work

### 3.1 Introduction

This chapter provides a description of the materials, equipment and devices used in the current analysis, since this chapter provides four main themes:-

1. Preparation of  $\alpha$ -Al<sub>2</sub>O<sub>3</sub> nanoparticles, using Sol-Gel Method.
2. Preparation and coating of low carbon steel samples with two layers of coating, the first is a binder, and the second is  $\alpha$ -Al<sub>2</sub>O<sub>3</sub> nanoparticles, using the Plasma Spray Method.
3. Study the effect of high temperatures on non-coated and coated samples with the presence and absence of corrosive medium (V<sub>2</sub>O<sub>5</sub> + Na<sub>2</sub>SO<sub>4</sub>).
4. Study the structural properties of nanoparticles and the topography of the surface of the coated and uncoated samples, as well as the corrosion rate.

### 3.2 Chemicals and Raw Materials

Materials used in the current study to synthesis  $\alpha$ -Al<sub>2</sub>O<sub>3</sub> nanoparticles and used in the coated process for samples are shown in Table (3.1).

### 3.3 Preparation of $\alpha$ -Al<sub>2</sub>O<sub>3</sub> Nanoparticles

Aluminum oxide nanoparticles have been prepared using Sol-Gel method. Figure (3.1) shows a chart of the steps used in the practical aspect of preparing the nanoparticles.

Table (3.1) Physical and chemical properties of the materials used in the present study

Materials	Chemical formula	Purity ratio %	Molar Mass g/mole	The supplied company	Producing Country
Aluminum Nitrate 9 hydrate	$\text{Al}(\text{NO}_3)_3 \cdot 9\text{H}_2\text{O}$	97	375.13	BDH	England
Ethanol	$\text{C}_2\text{H}_5\text{OH}$	99	46.07	CHEM-LAP	Belgium
Poly (vinyl alcohol) PVA	$\text{C}_2\text{H}_4\text{O}$	99	44.05	Sigma-Aldrich	Germany
Vanadium pentoxide	$\text{V}_2\text{O}_5$	99.9	181.88	India Mart	India
Sodium sulfate	$\text{Na}_2\text{SO}_4$	99.2	142.04	India Mart	India
Nickel Chromium Aluminum Yttrium Alloy	NiCrAlY Amdry - 962	—	225.76	Oerlikon Metco	USA
Ferrous carbonate	$\text{FeCO}_3$	98.7	115.85	Ltd. New Delhi Co	India
Acetone	$(\text{CH}_3)_2\text{CO}$	99.7	58.08	Romil	England

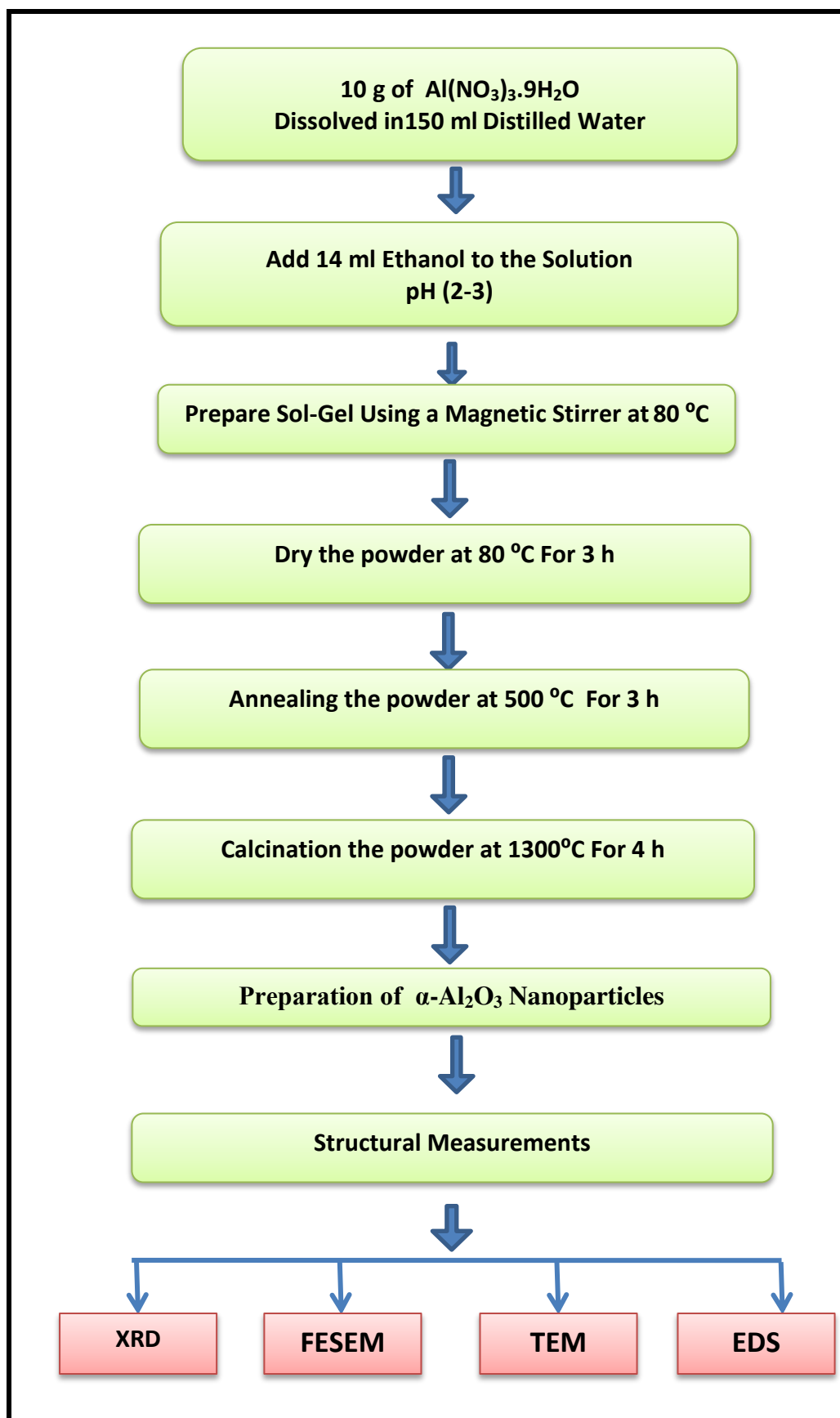


Figure 3.1 : Schematic diagram of the preparation of  $\alpha$ - $\text{Al}_2\text{O}_3$  nanoparticles

### 3.3.1 Prepare the solution

The solution was prepared with a concentration of 0.18 M, where 10 g of  $\text{Al}(\text{NO}_3)_3 \cdot 9\text{H}_2\text{O}$  was completely dissolved in 150 ml of distilled water [80]. To obtain the required weight to be dissolved within the previous standard, the following relation was used [158].

$$M = \frac{W_t}{M_{wt}} * \frac{1000}{V} \dots\dots\dots(3.1)$$

Where, M: (The molar concentration),  $M_{wt}$  : ( material's molecular weight), V: (Volume distilled water) and  $W_t$  : (The weight).

Material weight was measured by a sensitive electronic balance type (Genex Laborites) of American origin, with a four-digit sensitivity ( $10^{-4}$  g) . The solution was mixed well at room temperature using a magnetic stirrer of Korean origin, Then 14 ml of ethanol solution was added drop by drop to the solution and the temperature of the solution gradually increased to 80 °C and fixed to this degree. We notice that the color of the solution changes from orange to dark brown, and that the pH ranges between 2 and 3. Then leave the solution on the magnetic stirrer for (40- 45) min, to evaporate the liquid gradually until the solution turns into a (Gel) [80].

### 3.3.2 Drying stage

After obtaining the Gel, it was dried at 80 °C for 3 hours, using the drying oven made by the (German Company Memmer). After that it was left to cool to room temperature, then a dry white powder was obtained. After this stage the powder was ground and turned into a very fine powder and sifted through a sieve tool with dimensions of (75 mesh size).

---

### 3.3.3 The Annealing Stage and the Calcination

After the drying of the powder, the annealing stage was achieved by placing the resulting powder inside automatic oven with time and temperature control (max. 1200 °C) and made by the Korean company (LAB TECH), at a temperature of 500 °C for a period of 3 hours, in order to get rid of all water molecules and other liquids. After that, was left the powder inside the oven to cool gradually. The resulting powder was ( $\gamma$ - Al<sub>2</sub>O<sub>3</sub>). In order to obtain ( $\alpha$ -Al<sub>2</sub>O<sub>3</sub>) nanoparticles, the powder was calcined at a temperature of 1300 °C for a period of 4 hours [1], using an automatic furnace produced by (LAC) of Czech origin (maximum temperature of 1600 °C), after that the powder was left inside the oven to cool gradually. Then the resulting powder is placed inside a glass tube to study its structural and morphological properties using a (XRD, TEM and FESEM techniques).

### 3.4 Coating process for samples

The TBC system consists of two layers, the first is a bond layer which is (NiCrAlY) powder and the second layer consists of ( $\alpha$ -Al<sub>2</sub>O<sub>3</sub>) nanoparticles prepared as a top layer and the coating is done with plasma spray technique.

Figure (3-2) shows a chart of the steps used in the coating process of samples.

#### 3.4.1 Preparation of low carbon steel samples

Low carbon steel (304L) was used in this study. The chemical composition tests were conducted at the Central Organization for Standardization and Quality Control - Ministry of Planning (Table 3.2).

Samples were cut using a metallurgical sample cutter with a surface area of  $8.4 \text{ cm}^2$  and shape dimensions of  $(3 \times 1 \times 0.3 \text{ cm})$  length, width and thickness, respectively. These samples were abraded using sand paper (Emery Papers) 220, 400, 800, 1000, and 1500  $\mu\text{m}$ . The samples were then washed using (distilled water, acetone, and alcohol). After that, the samples were dried in the oven at  $(50 \text{ }^\circ\text{C})$  for half an hour, and held in the desiccator until they were used. Before each check, an electronic balance weighed a sample to the fourth decimal of grams and measurements calculated by vernier to the second decimal position of millimeters.

**Table 3.2: Chemical compositions of low carbon steel 304L.**

Element	C	Cr	Ni	Mn	P	Mo	Si	Cu	Co	Fe
Wt. %	0.032	17.7	9.45	1.18	0.033	0.34	0.075	0.221	0.125	Balance

### 3.4.2 Granulation of Alumina Nanoparticles

A big problem presented during the production of nano ceramic coating that cannot be fed directly into the air plasma spray system, because it has a high surface area, low mass and small inertia. Nanopowders stick to the walls of the feeding system and make it difficult to move them toward the plasma torch. To solve this problem, the granulation process must be performed for the nanoparticles. To perform this process, 10 g of polyalynyl alcohol (PVA) was dissolved in 100 ml of distilled water using a magnetic stirred device for about 25 minutes at a temperature of  $40 \text{ }^\circ\text{C}$  until the PVA was completely dissolved, then the alumina nanopowders was gradually added to the solution for 15 min until the product is

dispersed. After granulation, the product was dried for 12 hours at 200 °C. Then the product was ready for use in spraying plasma spray system [75].

### **3.4.3 Coating samples**

In order to obtain good adhesion to the coating, the substrates were roughened by sandblast which consists of alumina particles of 300 μm, pressure of 5 bars, and the distance between a jet of sand and the samples was 30 cm. The coating process is done by the plasma device (METCO Gun Type:3MB), made in United states of America and it is located in the laboratories of the Energy and Materials Research Center- Tehran –Iran, as shown in Figure (3.3).

During the spraying process, the angle of the plasma spray gun was always perpendicular to the substrate. Table 3.3 shows the parameters of plasma spraying process.

### **3.5 Plasma spray device**

The plasma spraying technique is basically spraying molten material on surface to supply the coating. Where injection of the powder into a very hot plasma flame, as shown in Figure (3.4) [159]. The plasma spray device consists of the following parts[160]:-

1. Plasma Torch.
2. Powder Feeder.
3. Power Supply.
- 4- Control unit.
5. Plasma Gas and Carrier Gas Supply.
6. Cooling Water System.

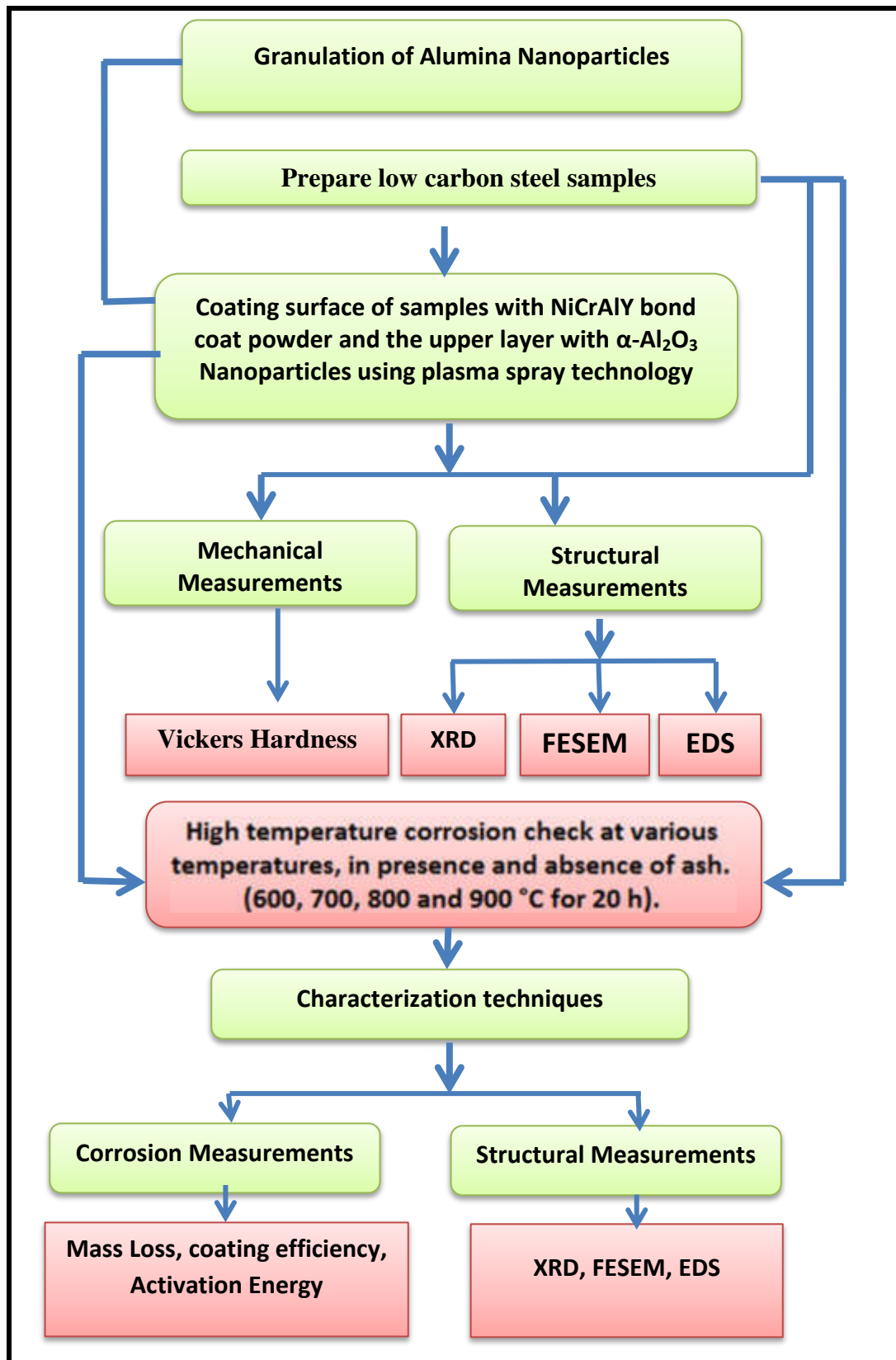


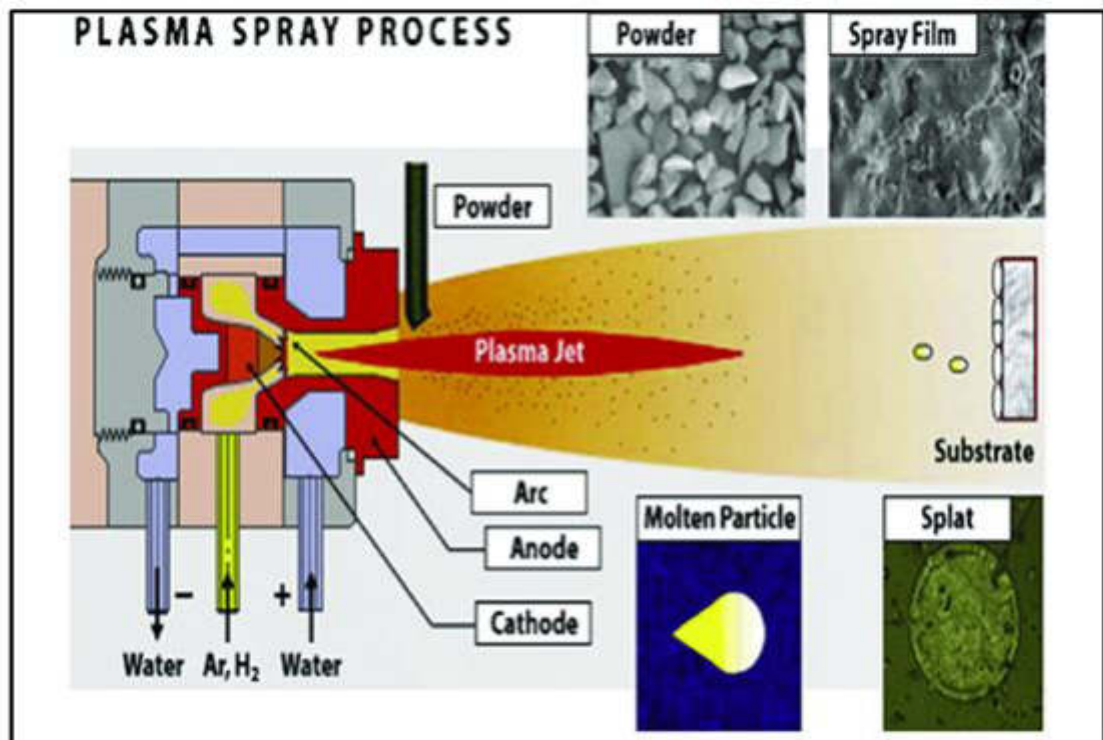
Fig. 3.2 :Schematic diagram of Coating process and Characterization techniques for samples.

**Table 3.3: Parameters of plasma spraying.**

Parameter	Bond coat NiCrAlY	Top coat $\alpha$ -Al <sub>2</sub> O <sub>3</sub>
Primary gas, Ar (ℓ/s)	85	80
Secondary gas, H <sub>2</sub> (ℓ/s)	15	15
Current(A)	450	500
Voltage (V)	50	55
Powder feed rate(g/min)	45	35
Spray distance (cm)	12	8
Thicknesses (μm)	100±10	40 ± 5



Figure 3.3: Photograph of the plasma spray system.



3.4 Schematic Diagram of the Plasma Spray Process [159]

### 3.5.1 Plasma Torch

Plasma torch or plasma jet, is the main instrument that converts electrical energy into heat energy and mixes the coating materials with the plasma flame. It consists of a copper anode and a tungsten cathode.

The plasma consists of an inert gas, argon gas, which is the main gas with hydrogen gas as the secondary gas, and a high-frequency electric arc is dropped between the nozzle and the electrode when the gas flows around the cathode and through the anode that is produced in the shape of a narrow nozzle, which ionizes the gas [160].

The degree of ionization increases with the increase in the arc current. This leads to an increase in energy, expansion of the gas, and an increase in its speed. Argon was used as the most preferred primary plasma gas, since plasma formation is the easy and appears to be less violent towards electrode and nozzle because it is an inert gas.

### **3.5.2 Powder Feeder**

Powder feed is the method of inserting powder into the flame at the required rate without any obstacles. The process of transferring the powder to the flame gun is not a simple process, but in reality it requires a great deal of knowing, in order to obtain a distribution of the size of the powder molecule used to spray the plasma in a way so that the moisture of the powder that may cause agglomeration should be avoided, and there are many techniques for feeding the materials.

A volumetric powder feeder technique was used in this study. In this technique, the powder stored in a conical chamber is dropped into a rotating disk through a small, adjustable opening.

This technique is considered the typical positive type because it guarantees the smooth volumetric flow of the powder, it can control the flow rate and requires a small speed for the carrier gas. As the speed of the disk increases, the flow rate of the powder will increase.

### **3.5.3 Control Unit**

The control unit is one of the main parts of the plasma spray device, as the operation and stopping of the plasma system is quickly controlled from the remote spraying position as well as controlling the operation and stopping of the powder feeding. It can also control the flow of plasma gas (argon and hydrogen). The control unit is located in the bucket switch and acts as an emergency switch.

### **3.5.4 Cooling Water System**

The plasma gas which is inserted through the cathode in the plasma spraying process, is heated by the plasma arc and the plasma torch comes

out of the anode as its temperature reaches 10,000 K , and this requires a cooling system to cool the anode while working. Therefore, the cooling system surrounds the anode and uses water for this purpose, which is entered through an external source as shown in Figure (3.4) [159].

### **3.6 High Temperature Corrosion Test**

Corrosion tests for uncoated and coated samples with and without of ash, at various temperatures (600, 700, 800 and 900 °C) for 20 hours were carried out. Where the process of oxidation was done in four steps:

- 1.sample without coating and without ash.**
- 2.sample without coating and with ash.**
- 3.sample with coating and without ash.**
- 4.sample with coating and with ash.**

#### **3.6.1 Ash preparation**

Ash of heavy fuel is composed of ( $V_2O_5$  and  $Na_2SO_4$ ) where it was mixed with (57 wt%  $V_2O_5$  and 43 wt%  $Na_2SO_4$ ) with a weight of 5.7 g of ( $V_2O_5$ ) and 4.3 g of ( $Na_2SO_4$ ) by a sensitive electronic balance type, with a four-digit sensitivity ( $10^{-4}$  g) . These materials are mixed and grinded with a mortar and then mixed with acetone; the surface of the uncoated and coated samples was covered with the mixture for 20 minutes until the samples were acetone free.

#### **3.6.2 Preparation of the pickling solution**

Preparation process of the pickling solution was done with (120 ml) distilled water, 30 ml hydrochloric acid (HCl), and 10 g ferrous carbonate ( $FeCO_3$ ). Then the solution was placed in the electric mixer for

(10-15) min. A pickling solution does not strike the metal but dissolves and eliminates the product's corrosion layer [78].

### **3.6.3 Oxidation Test For Samples Without Ash**

Ash-free samples were tested for coated and uncoated samples by inserting them into an electric oven at different temperatures (600, 700, 800, 900 ° C) for (20 h). The samples were removed from the furnace after (24 h, to avoid rapid cooling and cracking. After that, remove corrosion products from the samples via pickling solution, samples are then washed and allowed to dry for half an hour, and again weighed.

### **3.6.4 Oxidation Test For Samples With Ash**

After the surface of the uncoated and coated samples was covered with the mixture of ash, they were tested at different temperatures and for a fixed time as shown in the steps of paragraph (3.5.3).

## **3.7 Characterizations Techniques**

Nanoparticles and samples were characterized by XRD, TEM, FESEM and EDS. Also study the mechanical properties by (Vickers hardness) of the surface of the samples after coating. The corrosion rate and coating efficiency of samples were also studied.

### **3.7.1 Structural Measurements**

X-ray diffraction analysis, has been used to analyze the alumina nanoparticles' crystalline structure, As well as the surface of the coated and uncoated samples before and after the oxidation test. The X-ray diffraction device used in this study was of the type (Shimadzu-6000) of Japanese origin.

The conditions of measurement:

Target ( Cu-K $\alpha$ ),  $\lambda = 1.5406$  nm , V = 40 kV, I = 30 mA  
2 $\theta$ : (10-100°). The device is equipped with a supplement program for it called PCPFWIN and this program is very important because it provides us with the standard ICDD Card, through which the accuracy of the prepared powder is verified. The required structural parameters crystallite size, interplanar spacing and the lattice constants were also calculated according to special equations illustrated in the theoretical part.

### **3.7.2 Transmission electron microscopy (TEM)**

The TEM technique was used to study the alumina nanoparticles prepared by sol-gel method, to show if they were within the nanoscale, and can be used to study the morphology of samples surface coated with a layer of nanoparticles.

The device used in this study is of the type 12AB-Leo, German origin, which is found in the central research laboratory at the University of Mashhad - Iran.

### **3.7.3 Field Emission Scanning Electron Microscopy (FESEM)**

FESEM was used to calculate that the average grain size of  $\alpha$ -Al<sub>2</sub>O<sub>3</sub> nanoparticles, as well as observing the surface topography of the samples before and after the test, and taking photos of the cross section for determining the thickness of both coating layers.

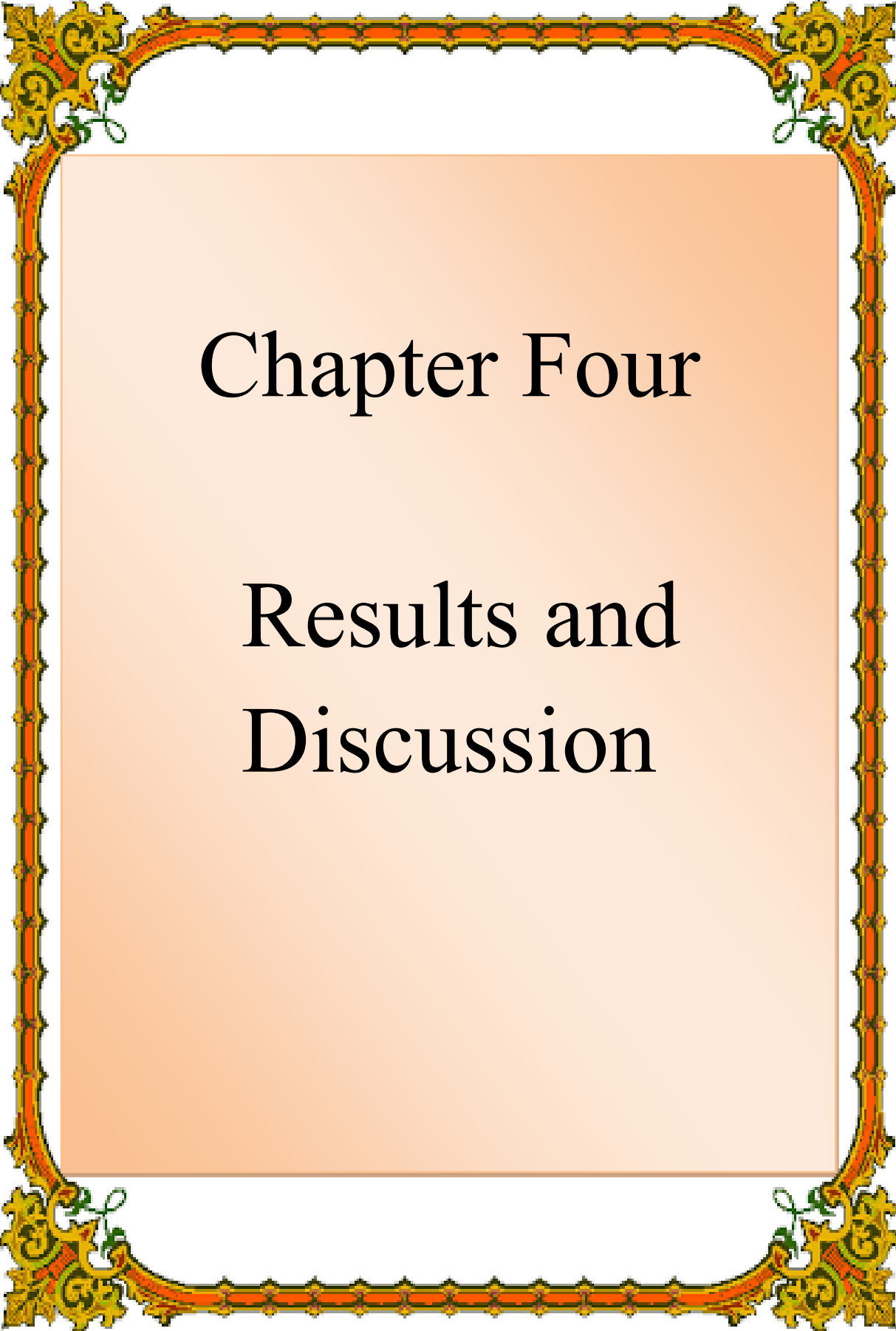
The device has been used (MIRA3) model, manufacturer of the (TESCAN) Czech company, it is located in the central research laboratory of Mashhad University – Iran.

### 3.8 Hardness Test

Microscopic hardness (Vickers hardness) for the surface of low carbon steel samples was measured before and after coating using a Leitz wetzlar type device, model (GMBH - D6330), manufactured by (Wetzlar Germany), It is located in the laboratory of the Department of Mechanical Engineering University of Diyala. The microscopic hardness of the samples was measured after smoothing and polishing. Hardness was measured by a load of (9.8 N) for a period of (15 sec).

### 3.9 Corrosion Measurements

In order to identify the effect of high temperatures on coated and not coated samples with two layers, the first bond layer (NiCrAlY ) and the top layer  $\alpha$ -Al<sub>2</sub>O<sub>3</sub> nanoparticles, corrosion rate, coating efficiency and activation Energy was calculated.



# Chapter Four

## Results and Discussion

---

## 4.1 Introduction

This chapter includes four main parts:

1. Study of the structural properties of the alumina nanoparticles prepared by Sol-Gel method.
2. Study of the structural properties and topography of the surface of steel samples before and after coating with two layers, bonding layers (NiCrAlY) and the top layer, the alumina nanoparticles  $\text{Al}_2\text{O}_3$ .
3. for uncoated and coated samples in the presence and absence of ash at different temperatures of 600, 700, 800 and 900 °C for 20 h
3. A study of the structural and morphological characteristics for uncoated and coated samples in the presence and absence of ash at different temperatures of 600, 700, 800 and 900 °C for 20 h.
- 4- Calculating the corrosion rate of the samples by weight loss method, as well as calculating the efficiency of the coating and the effect of the corrosive medium, as well as calculating the activation energy of the prepared samples.

## 4.2 Structural Properties of the $\alpha\text{-Al}_2\text{O}_3$ by Sol-Gel method

### 4.2.1 XRD Analysis of $\alpha\text{-Al}_2\text{O}_3$ nanoparticles

Figure (4.1) shows the XRD patterns of the prepared  $\alpha\text{-Al}_2\text{O}_3$  nanoparticles, it was found that the diffraction peaks ( $2\theta \sim 43.8^\circ, 35.0^\circ, 57.4^\circ, 25.4^\circ, 68.1^\circ, 52.5^\circ, 37.7^\circ, \text{ and } 66.5^\circ$ ) which referred to (113), (104), (116), (012), (300), (024), (110), and (214) favorite directions respectively.

The results also showed that the nanoparticles have a Polycrystalline structure and in nature with a hexagonal structure. These values were

corresponded exactly to (ICDD) card number (010-0173) of  $\alpha$ -Al<sub>2</sub>O<sub>3</sub>, and also in agreement with the results obtained by each of S. D. Anggraeni and F. Kurniawan [161] and R. Rogoan et. al. [162], as shown in the Figure (4.2).

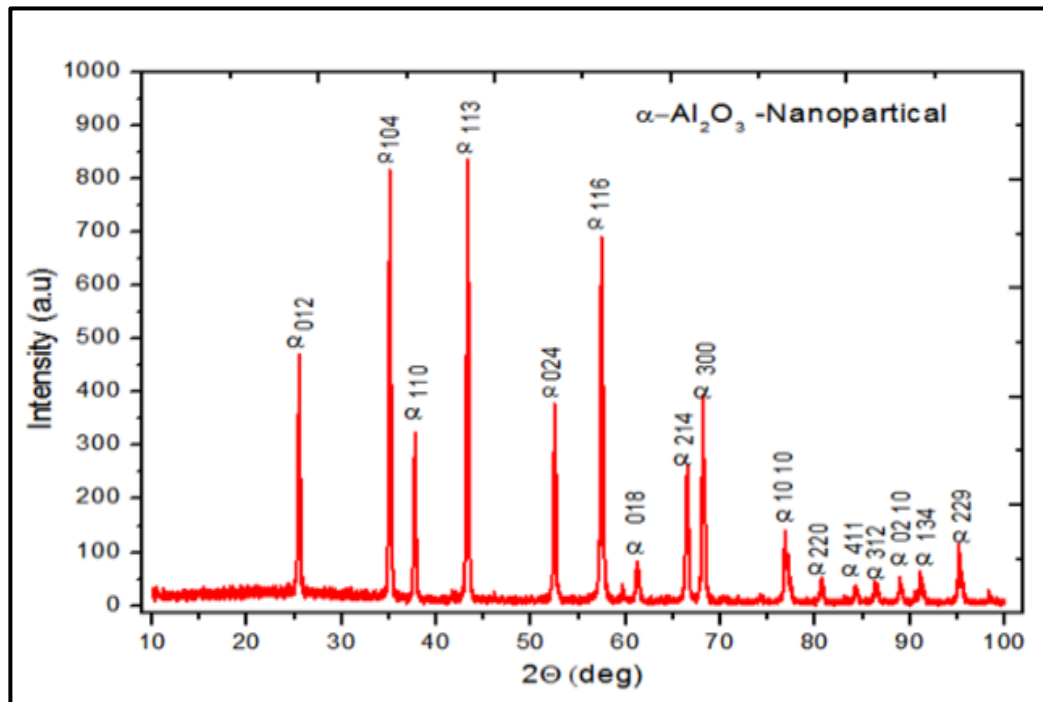


Figure 4.1: X-ray diffraction patterns for  $\alpha$ -Al<sub>2</sub>O<sub>3</sub> nanoparticles.

PDF Card Report of (ICDD) for $\alpha$ -Al <sub>2</sub> O <sub>3</sub> No:												
00-010-0173 (Fixed Slit Intensity) - Cu Ka1 1.54056Å												
2θ	d(Å)	I	h	k	l	*	2θ	d(Å)	I	h	k	l
25.5835	3.479000	75	0	1	2		80.6922	1.189800	8	2	2	0
35.1356	2.552000	90	1	0	4		83.2166	1.160000	<1	3	0	6
37.7837	2.379000	40	1	1	0		84.3753	1.147000	6	2	2	3
41.6834	2.165000	<1	0	0	6		85.1808	1.138200	2	1	3	1
43.3620	2.085000	100	1	1	3		86.3752	1.125500	6	3	1	2
46.1829	1.964000	2	2	0	2		86.4613	1.124600	4	1	2	8
52.5512	1.740000	45	0	2	4		89.0177	1.098800	8	0	2	10
57.5177	1.601000	80	1	1	6		90.6622	1.083100	4	0	0	12
59.7673	1.546000	4	2	1	1		91.2011	1.078100	8	1	3	4
61.1641	1.514000	6	1	2	2		95.2597	1.042600	14	2	2	6
61.3435	1.510000	8	0	1	8		98.4065	1.017500	2	0	4	2
66.5465	1.404000	30	2	1	4		101.0917	0.997600	12	2	1	10
68.1962	1.374000	50	3	0	0		102.7879	0.985700	<1	1	1	12
70.3570	1.337000	2	1	2	5		103.3450	0.981900	4	4	0	4
74.2661	1.276000	4	2	0	8		109.5222	0.943100	<1	3	2	1
76.8800	1.239000	16	1	0	10		109.8330	0.941300	<1	1	2	11
77.2268	1.234300	8	1	1	9		111.0290	0.934500	4	3	1	8

Figure 4.2 ICDD card number (00-010-0173) of  $\alpha$ -Al<sub>2</sub>O<sub>3</sub> nanoparticles.

---

### 4.2.2 Calculation of interplanar spacing ( $d_{hkl}$ )

Interplanar spacing with the same Miller coefficients was calculated using Bragg's law and from the relationship (2.6). Where it was found that the value of ( $d_{hkl}$ ) is consistent with the values of the, (ICDD) (10-0173) of  $\alpha$ -Al<sub>2</sub>O<sub>3</sub>, as shown in the table (4.1).

### 4.2.3 The lattice constants ( $a_0$ , $b_0$ and $c_0$ )

The crystal lattice constants ( $a_0 = b_0$ , and  $c_0$ ) were calculated for the alumina nanoparticles prepared by the sol-gel method. Using the relationship (2.8). Where the lattice constant ( $a_0$ ) is calculated from them for the plane (110), and the lattice constant ( $c_0$ ) was calculated for the plane (113). It was found that the values of the lattice constants are consistent with the values in the international card number (00-010-0173). As shown in the table (4.2).

### 4.2.4 The crystallite size ( $D_{av}$ )

#### I. Calculation of crystallite size using Scherrer's formula:

The crystallite size of the prepared nanoparticles was determined by using a relationship, (Scherrer method) according to the relation (2.9). It has been observed that the crystallite size for the prepared nanoparticles equals (33.9) nm as shown in Table (4.2).

#### II. Calculation of crystallite size by Williamson-Hall analysis:

The average crystallite size of the synthesized nanoparticles has been calculated by (Williamson-Hall) analysis according to the relationship (2.12). Where ( $4\sin\theta$ ), is plotted on the (X axis) and ( $\beta \cos\theta$ ) on (Y-axis). The average crystallite size ( $D_{av}$ ) from the (y-intercept), and microstrain ( $S$ ) from the fit slope were calculated from a linear fit to the

results. During the creation of the nano materials microstrain is induced, and it will be elevated from extension or lattice compression. Microstrain result from varying displacement of the atoms with respect to the their reference lattice positions. A negative microstrain value for  $\alpha\text{-Al}_2\text{O}_3$  nanoparticles, will lead to compression in the lattice [163]. It has been noted that crystallite size for the particles prepared is equal to (27.7) nm as shown in Table (4.2).

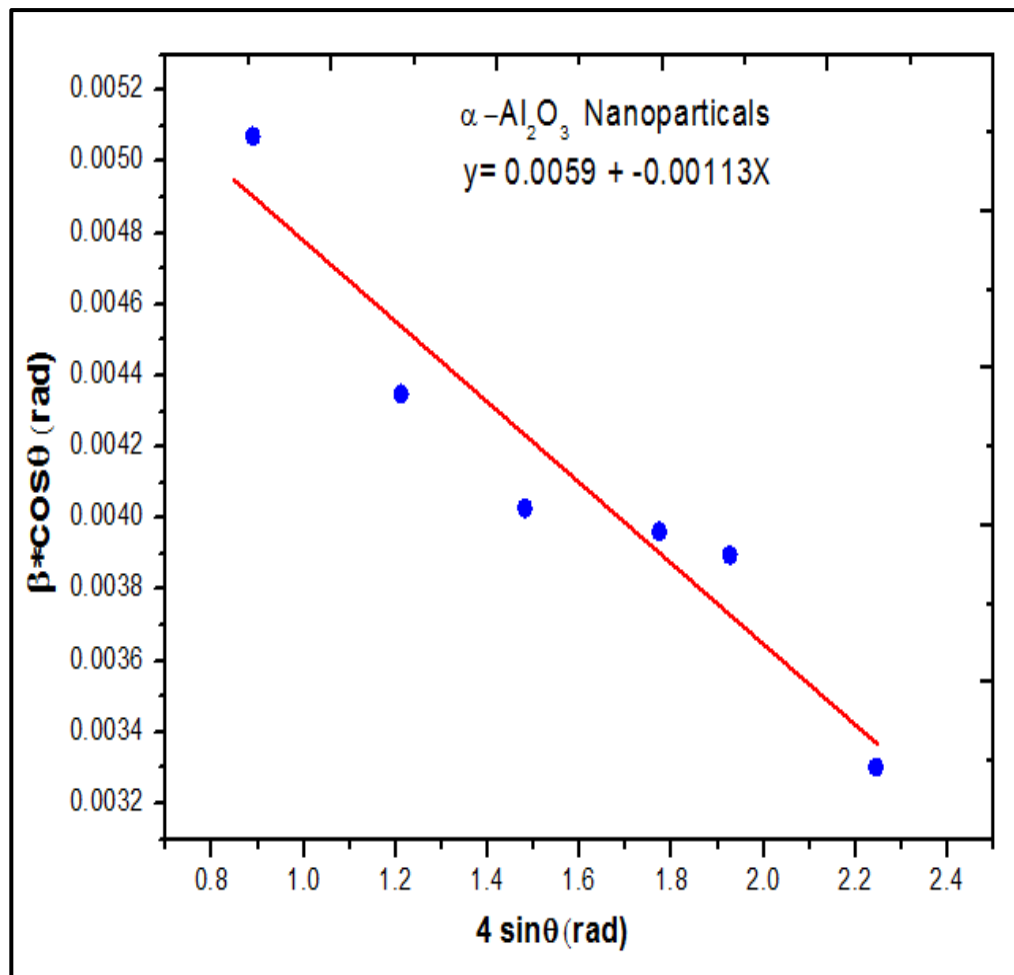


Figure 4.3: The W-H analysis of  $\alpha\text{-Al}_2\text{O}_3$  nanoparticles.

Table 4-1: Some of the results obtained from X-ray diffraction and its comparison with the international card (00-010-0173).

Sample	$2\Theta$ (deg)	$d_{hkl}$ (Å)	FWHM(deg)	$hkl$
$\alpha$ -Al <sub>2</sub> O <sub>3</sub> (ICDD) card number (00-010-0173)	43.4	2.08	_____	(113)
	35.1	2.55	_____	(104)
	57.5	1.60	_____	(116)
	25.5	3.47	_____	(012)
	68.1	1.37	_____	(300)
	52.5	1.74	_____	(024)
	37.7	2.37	_____	(110)
	66.5	1.40	_____	(214)
$\alpha$ -Al <sub>2</sub> O <sub>3</sub> prepared	43.3	2.08	0.2071	(113)
	35.1	2.55	1.955	(104)
	57.4	1.60	2.214	(116)
	25.5	3.48	0.2200	(012)
	68.1	1.37	0.2098	(300)
	52.5	1.74	0.1971	(024)
	37.7	2.38	0.2141	(110)
	66.5	1.40	0.2212	(214)

---

### 4.2.5 Dislocation Density ( $\delta$ )

The density of dislocation is the measurement of the number of defects within the crystal. The low value of the density of dislocation obtained in the present research confirmed strong crystallization of  $\alpha$ -Al<sub>2</sub>O<sub>3</sub> nanoparticles prepared by Sol-gel. The dislocation density was calculated according to equation (2.10), and there is an inverse relation, between the density of dislocation, and the size of crystals, as a result, the intensity of the dislocation decreases when crystal size values increase, as shown in Table (4.2).

### 4.2.6 Texture coefficient $T_c$ (hkl)

The texture coefficient of the  $\alpha$ -Al<sub>2</sub>O<sub>3</sub> nanoparticles was calculated using equation ( 2.14) . It describes the predominant direction of the crystal plane (h k l) of the prepared nanoparticles It was found that its value is less than one and this means that the prepared nanoparticles are polycrystalline, but in multiple directions [163], as shown in Table (4.2).

### 4.2.7 Specific Surface Area (SSA)

Specific Surface Area (SSA) of the  $\alpha$ -Al<sub>2</sub>O<sub>3</sub> nanoparticles was calculated using equation ( 2.17). It was found to decrease with increasing crystallite size, as shown in Table (4.2).

Table 4.2: Structural parameters of the  $\alpha$ -Al<sub>2</sub>O<sub>3</sub> nanoparticles

Structural parameters		$\alpha$ -Al <sub>2</sub> O <sub>3</sub> Nanoparticles
D <sub>av</sub> (nm)	Scherrer	33.9
	W.H	27.7
$(\delta)$ $* 10^{-4} (\text{nm}^{-2})$	Scherrer	8.694
	W.H	13.03
(SSA) (m <sup>2</sup> .g <sup>-1</sup> ) $\rho = 3.95 \text{ g/cm}^3$ for $\alpha$ -Al <sub>2</sub> O <sub>3</sub> nanoparticles	Scherrer	36.717
	W.H	38.58
The lattice constants $\text{\AA}$	a <sub>0</sub>	4.761
	c <sub>0</sub>	12.978
Micro Strain $(S) * 10^{-3}$		-1.13
T <sub>c (hkl)</sub>		0.96

### 4.3 Morphological Analysis of the $\alpha$ -Al<sub>2</sub>O<sub>3</sub> prepared by Sol- Gel method

#### 4.3.1 FESEM Analysis of the $\alpha$ -Al<sub>2</sub>O<sub>3</sub> Nanoparticles

The Field Emission Electroscop (FESEM) was used to examine the  $\alpha$ -Al<sub>2</sub>O<sub>3</sub> nanoparticles prepared by Sol-Gel. Figure (4.4a, b) shows FESEM images of  $\alpha$ -Al<sub>2</sub>O<sub>3</sub> nanoparticles from. It is noted that the crystalline shapes have heterogeneous sizes, different shapes and spherical and semi-spherical shapes [5]. The pictures also showed the presence of agglomerates, which are due to the granulation process carried out on the nanoparticles after preparation so that they can be used in the plasma spraying process. There are also a large number of nanoparticles within these agglomerates. Figure (4.5) shows that the average grain size of  $\alpha$ -Al<sub>2</sub>O<sub>3</sub> was approximately (29 nm). This is in agreement with the x-ray diffraction results.

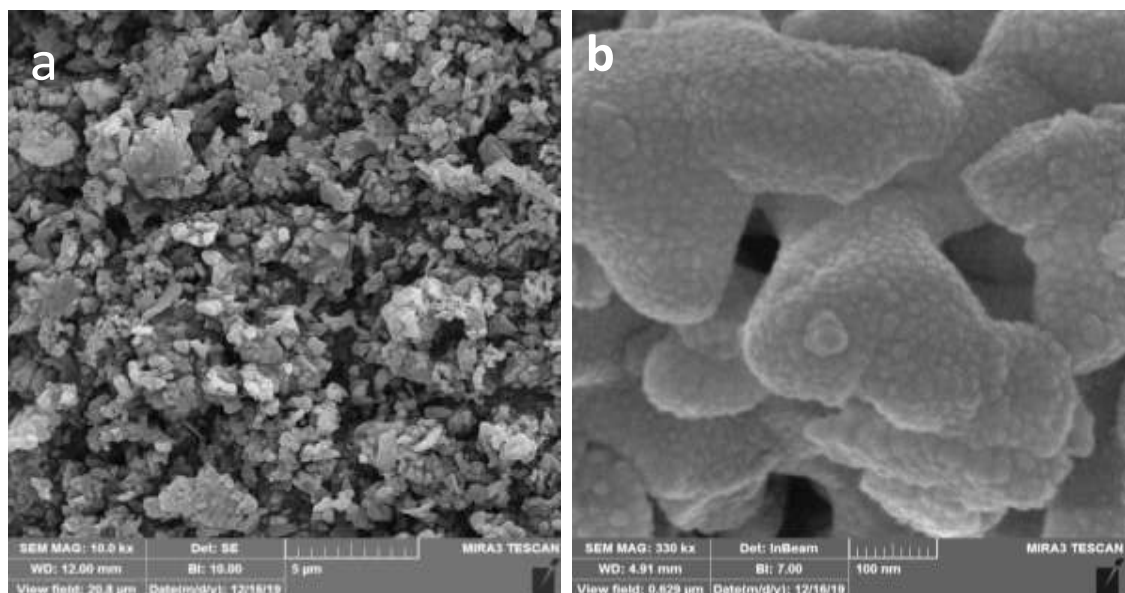


Figure 4.4: FESEM images of  $\alpha$ -Al<sub>2</sub>O<sub>3</sub> nanoparticles at (a) 10.0 kx and (b) 330 kx magnifications.

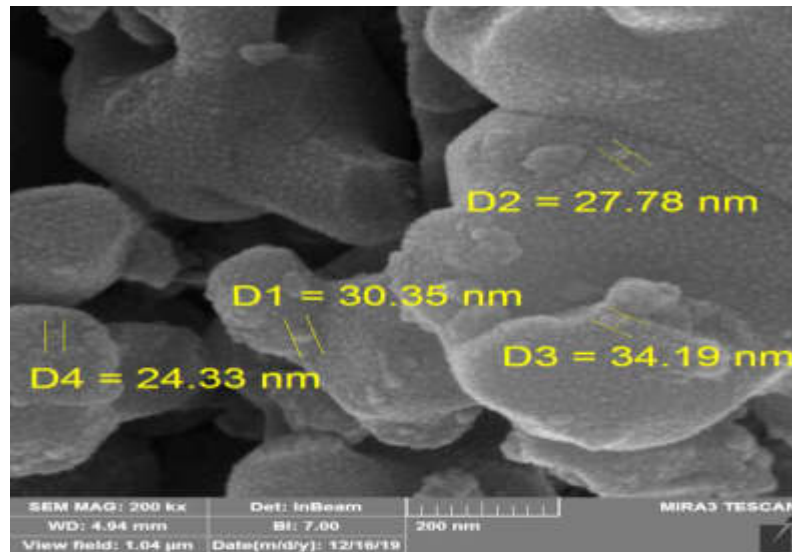


Figure 4.5: The average grain size FESEM image of  $\alpha$ -Al<sub>2</sub>O<sub>3</sub> at 200 kx magnifications.

#### 4.3.2 EDS of the $\alpha$ -Al<sub>2</sub>O<sub>3</sub> Nanoparticles

Fig (4.6) shows the energy dispersive spectroscopy (EDS) of the prepared  $\alpha$ -Al<sub>2</sub>O<sub>3</sub> powder by sol-gel method. The figure shows that the visible peaks are only for oxygen and aluminum. With the appearance of a few impurities of the element carbon, this results from the method of preparation after granulating the nanopowders, as well as from the powder preparation process before examining FESEM [164].

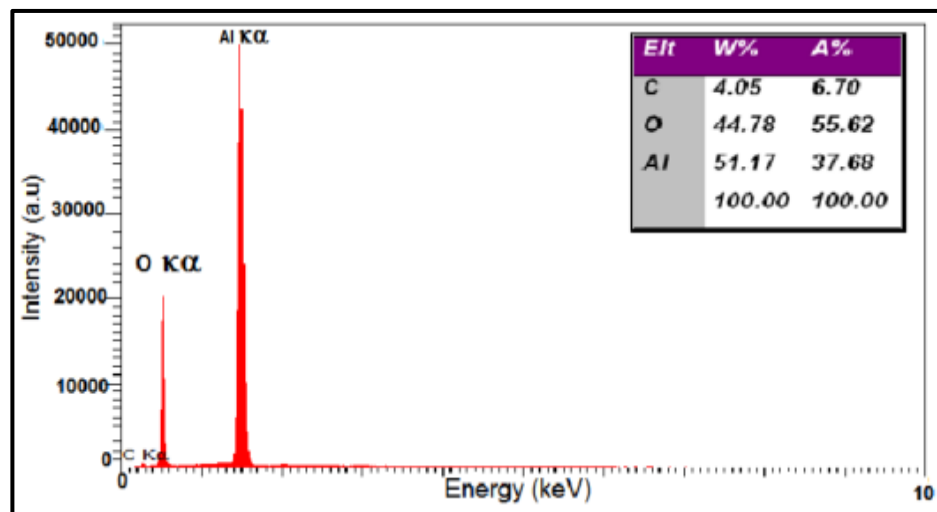


Figure 4.6: EDS of the prepared  $\alpha$ -Al<sub>2</sub>O<sub>3</sub> nanoparticles

### 4.3.3 TEM Analysis of the $\alpha$ -Al<sub>2</sub>O<sub>3</sub> Nanoparticles

The  $\alpha$ -Al<sub>2</sub>O<sub>3</sub> nanoparticles prepared by Sol-Gel was examined by the TEM. Figure (4.7) shows TEM images of the  $\alpha$ -Al<sub>2</sub>O<sub>3</sub> nanoparticles after granulation prepared that are agglomerations of the prepared nanoparticles, and the shape of the particles within the agglomerations is almost spherical, as shown by the images, that the prepared granules are within the nanoscale.

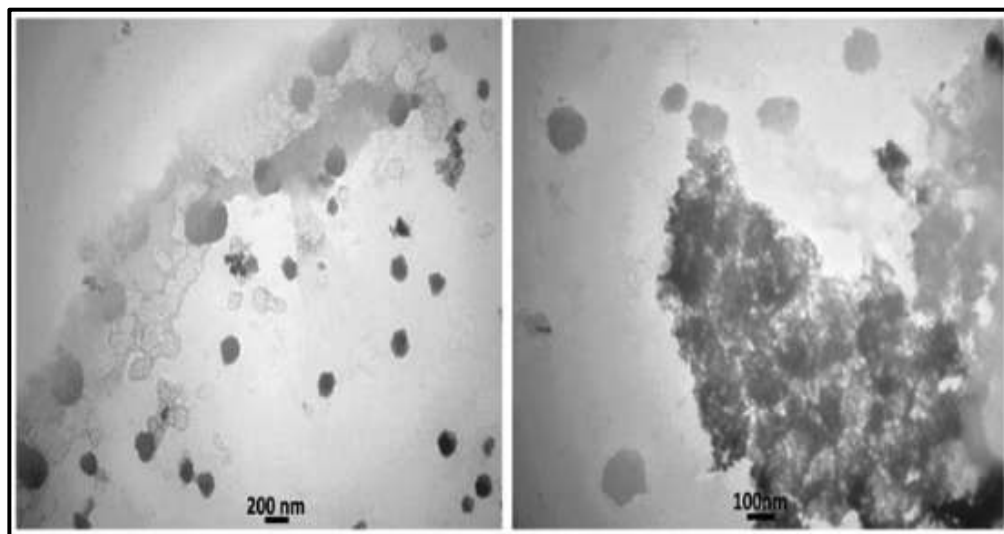


Figure 4.7: TEM of the prepared  $\alpha$ -Al<sub>2</sub>O<sub>3</sub> powder after granulation.

## 4.4 Analysis of NiCrAlY Powder

### 4.4.1 XRD Analysis of NiCrAlY Powder

Figure (4.8) shows the XRD patterns of the NiCrAlY Powder (Amdry 963 alloy), it was found that the diffraction peaks ( $2\theta \sim 44.09^\circ$ ,  $51.36^\circ$ ,  $75^\circ$ ,  $191.87^\circ$ , and  $97.29^\circ$ ) are referred to (111), (200), (311), (220), and (222) favorite directions respectively, These values correspond exactly to the card number (15-1294) of (NiCrAlY) Powder, these results are in

agreement with the results of the literatures, Sanxu et al, Shengqiang et al and Zhou et al [165- 167].

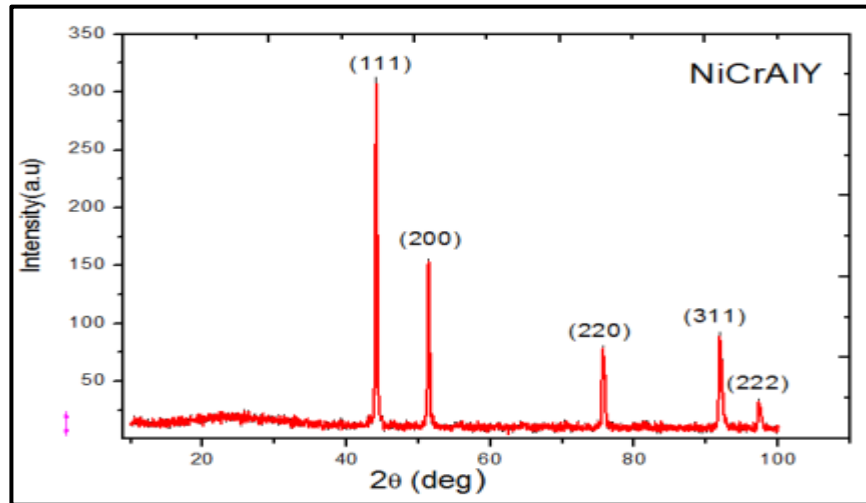


Figure 4.8: X-ray diffraction patterns for NiCrAlY Powder.

#### 4.4.2 FESEM of the NiCrAlY Powder

The NiCrAlY alloy Powder was examined by FESEM. Figure (4.9 a, b) shows FESEM images of NiCrAlY. The figure show that the crystalline shapes have spherical and semi-spherical shapes. This is in agreement with the results obtained from Takahashi et al [168].

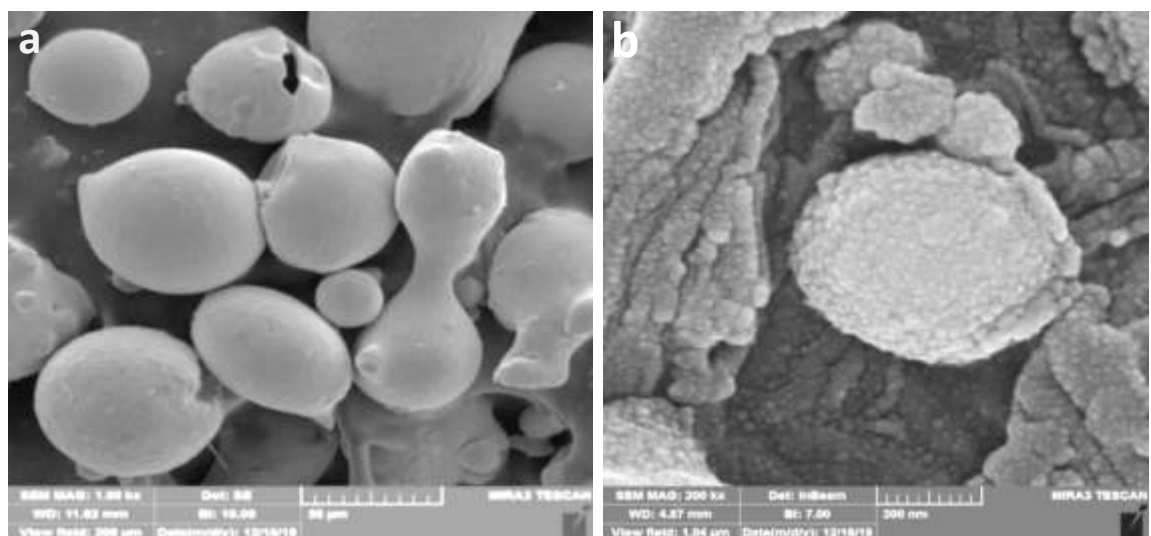


Figure 4.9 : FESEM of NiCrAlY alloy powder, at (a) 1.00 kx and (b) 200 kx magnifications.

## 4.5 Analysis of results of low carbon steel samples before coating and testing process

### 4.5.1 XRD Analysis of low carbon steel samples

Figure (4.10) shows the XRD patterns of low carbon steel samples , it was found that the diffraction peaks ( $2\theta \sim 43.56^\circ, 74.58^\circ, 50.65^\circ, 90.51^\circ, 44.42^\circ, 95.83^\circ$  and  $81.99^\circ$ ) referred to (111), (220), (200), (311), (110) , (222) and (221) favorite directions respectively. These values correspond exactly to the International Center of Diffraction Data (ICDD) card numbers (047-1405), (031-0619) and (050-1293) .

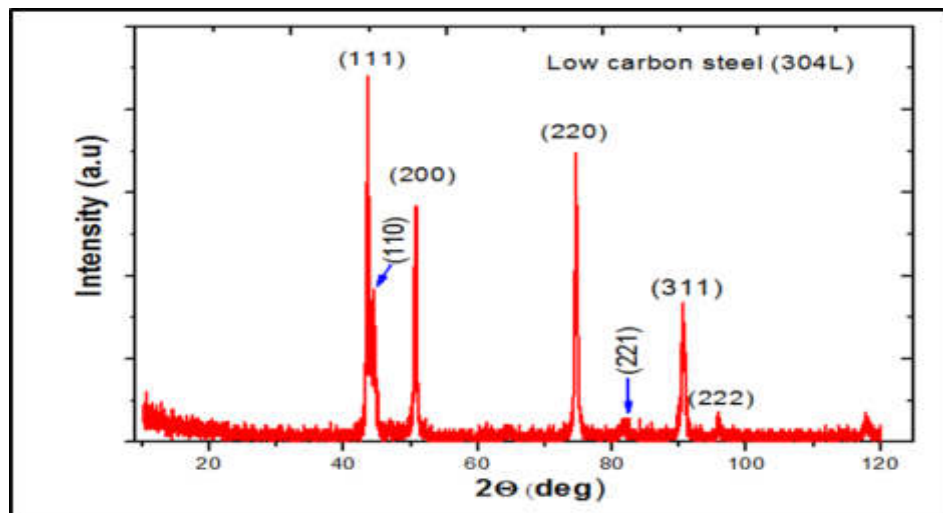


Figure 4.10: X-ray diffraction patterns for low carbon steel.

### 4.5.2 FESEM of low carbon steel samples before coating and testing

Figure (4.11) shows a picture of the low carbon steel samples surface using the (FESEM) before coating and testing, it was found that the presence of some lines that are produced by cleaning processes using glass paper, where smoothing has not been done highly and that is because the very satin surface impairs the consistency of the coating with the surface of the metal. Also it was found that the presence of some oxidation on the

surface and this is caused by the conditions of preparing samples for FESEM examination, or Exposure to atmospheric air before the examination.

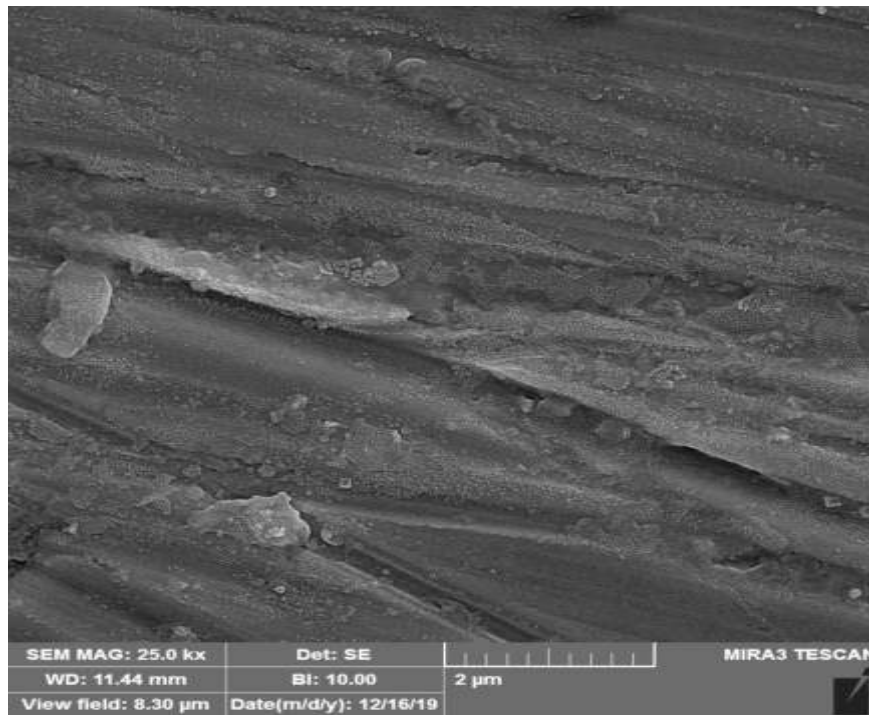


Figure 4.11 : FESEM of the low carbon steel samples surface before coating and testing at 25.0 kx magnifications

#### 4.5.3 EDS of low carbon steel before coating and oxidation test

Fig (4.12) shows the energy dispersive spectroscopy (EDS) of the low carbon steel samples surface before coating and testing. It was found from the figure that the predominant element in the sample is iron, followed by nickel, chromium, and other elements that are in lower proportions. These results are consistent with the results of the chemical analysis of the sample components mentioned in the third chapter of this study.

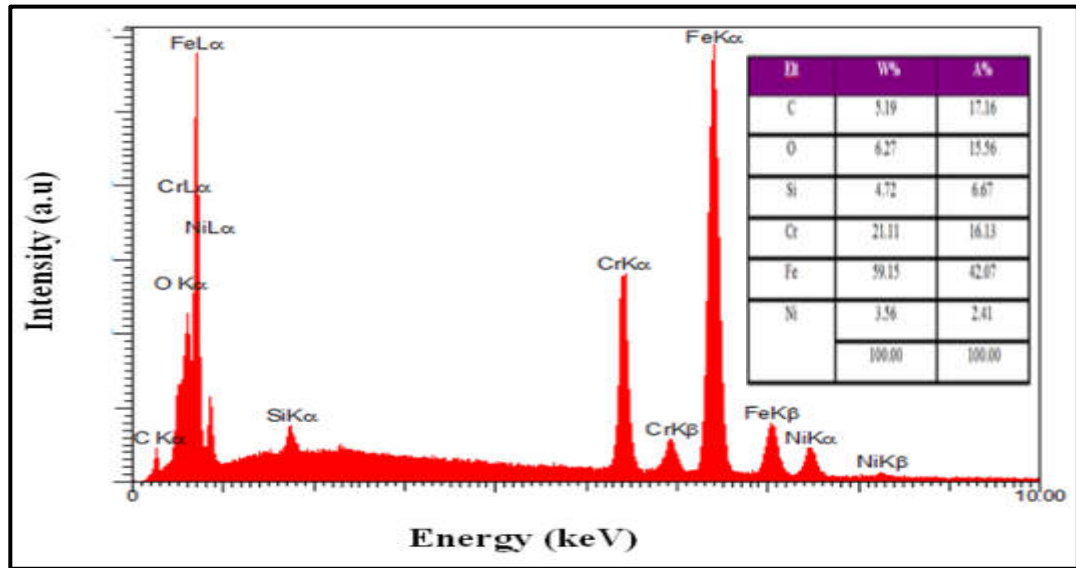


Figure 4.12: EDS of the low carbon steel samples surface before coating and testing

## 4.6 Analysis the results of samples after coating and before testing

### 4.6.1 XRD analysis the results of samples after coating and before testing

After completing the process of coating the samples with the bonding material and the upper layer, the synthetic tests were performed to the surface of the samples using XRD technique. Fig. (4.13b) shows the XRD patterns of the samples after coating, it was found that the diffraction peaks are located at ( $2\theta \sim 66.61^\circ, 45.66^\circ, 57.21^\circ, 67.95^\circ, 34.85^\circ, 37.42^\circ, 52.26^\circ$  and  $25.28^\circ$ ). It also notice the appearance of some peaks at ( $2\theta \sim 37.42^\circ$ , and  $45.66^\circ$ ) which belong to  $\gamma\text{-Al}_2\text{O}_3$  phases and these values are in agreement exactly to the ICDD cards numbers (00-010-0173) and (00-050-0741) of  $\gamma\text{-Al}_2\text{O}_3$  and  $\alpha\text{-Al}_2\text{O}_3$ . This is when comparing Figure 4.13b to Figure 4.13a, which represents diffraction patterns for  $\alpha\text{-Al}_2\text{O}_3$  nanoparticles.

The reason for the appearance of new phases is due to the exposure of the nanomaterial to high temperatures, whether during the process of thermal coating by plasma spraying technique [80].

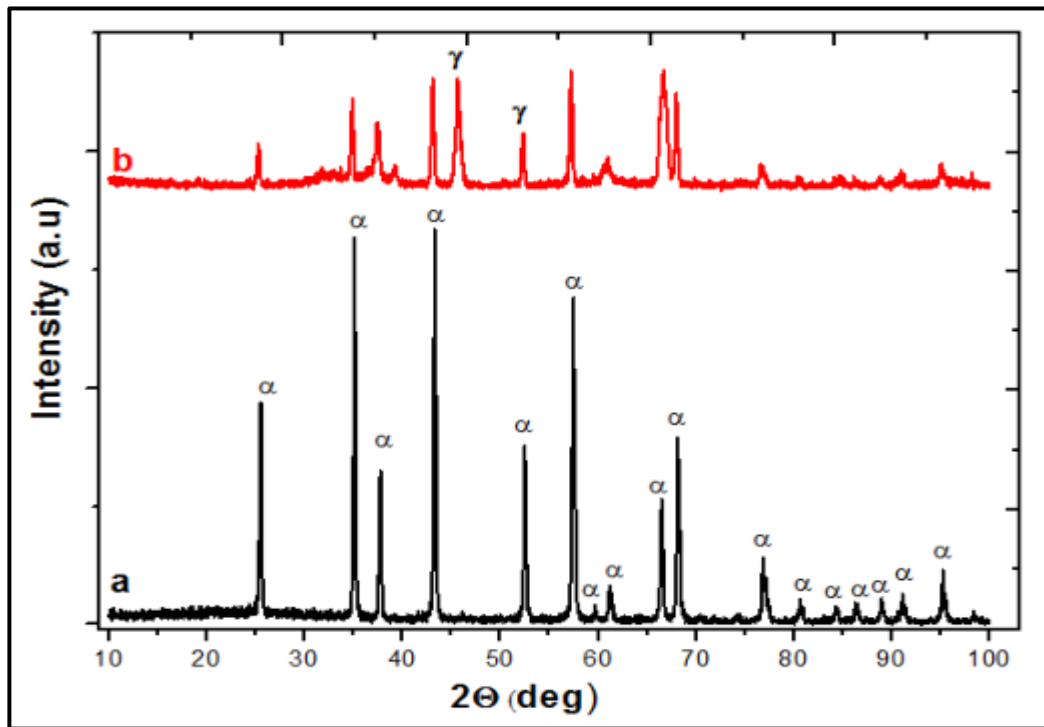


Fig.(4.13) (a): XRD patterns for  $\alpha$ - $\text{Al}_2\text{O}_3$  nanoparticles. (b): XRD of the samples after coating and before testing.

#### 4.6.2 Calculation of interplanar spacing ( $d_{hkl}$ ) of the samples after coating and before testing

Interplanar spacing with the same Miller indices of samples after coating and before testing has been calculated by reference to the Bragg's law and the relation (2.6). Where a value ( $d_{hkl}$ ) has been found to be consistent with (ICCD) (00-010-0173) and (00-050-0741), as shown in Table (4.3).

Table 4.3: Some of the results obtained from X-ray diffraction of the samples with coating and without ash before and after oxidation test

Sample	$2\Theta$ (deg)	$d(\text{\AA})$	FWHM(deg)	( $hkl$ )
Coat before Test	66.60	1.40293	0.8393	(440)
	45.66	1.98	0.6167	(400)
	57.21	1.61	0.480	(116)
After Test 600	57.45	1.60	0.2251	(116)
	43.30	2.09	0.2359	(113)
	35.1	2.55	0.2543	(104)
700	57.39	1.6	0.2388	(116)
	43.25	2.09	0.2687	(113)
	35.04	2.56	0.2326	(104)
800	57.2	1.6	0.2778	(116)
	43.05	2.09	0.2814	(113)
	34.85	2.57	0.2924	(104)
900	57.24	1.61	0.2330	(116)
	43.11	2.09	0.2337	(113)
	34.9	2.57	0.2277	(104)

---

### 4.6.3 The crystallite size ( $D_{av}$ )

The ( $D_{av}$ ) of samples after coating and before testing is estimated by using, (Scherrer method) and (Williamson-Hall analysis), according to the equation (2.9) and (2.12) respectively. It has been observed that the crystallite size value was (18.3 nm and 20.3 nm) respectively as shown in Table (4.5). It is noted that the crystalline size is less than the crystallite size of the nanoparticles before coating, and this result by using the plasma technology coating process led to the melting of the nanoparticles and their transformation into the liquid phase before colliding with the low carbon steel sample to form an upper coating layer which leads to the growth of the granules again under conditions plasma spray coating.

From findings, it has been found that, the value of a microstrain increases, with decreased crystallite size [169], as shown in the Figure (4.14).

### 4.6.4 Dislocation Density ( $\delta$ )

The dislocation density of samples after coating and before testing was calculated according to equation (2.10), it turns out that the intensity of dislocation increases when the values of the crystal size decreases, because the relationship between them is inverse, as shown in Table (4.4).

### 4.6.5 Texture coefficient $T_c(hkl)$

The texture coefficient of samples after coating and before testing was calculated using equation (2.14). It describes the predominant direction of the crystal plane (h k l) of the prepared nanoparticles. It has been found that its value is greater than one and this means that the polycrystalline nanoparticles have more dominance than other directions [170], as shown in Table (4.4).

#### 4.6.6 Specific Surface Area (SSA)

The specific surface area (SSA) of the samples after coating and before testing has been calculated using equation (2.17). It was found to increase with decreasing size of crystallite, determined by methods of Scherrer and Williamson Hall, as shown in Table (4.4).

#### 4.6.7 FESEM of the samples after coating and before testing

Figure (4.14 a and b) shows the cross-section of the as sprayed coatings. The figure shows the two layers of coating on the steel sample, and good adhesion between the bonding layer and the low carbon steel sample, and this is due to the preparation of the surface of the steel sample, especially the roughing process. It is also note that the top layer of alumina nanoparticles is homogeneous and does not contain gaps or cracks. This proves that the plasma spray coatings possess was a high coating quality as shown by the high-magnification FESEM images in figure (4.14a) and this results from the effects bonding between the splats [171-173]. This is due to the fact that the  $\alpha$ -Al<sub>2</sub>O<sub>3</sub> nanostructures layer is made from very fine particles and this also proves that the plasma spray technology is very effective in obtaining heat insulating ceramic layers, so it is used to protect the metals from corrosion in various conditions, including hot corrosion.

From figure (4.14a) it shows the growth of the thermal oxide layer (TGO) between the reference sample and the bonding layer, and the growth of another layer between the bonding layer and the top layer.

The thickness of the two layers of coating was calculated as the bonding layer was (100±10 μm) and for the upper layer (37±5 μm), as shown in figure (4.14b).

Figure (4.15) of FESEM shows images at 100 kx and 200 kx magnifications of the sample surface for sprayed coatings with  $\alpha$ -Al<sub>2</sub>O<sub>3</sub>.

nanoparticles. Where it can be noted that the upper layer of coating is typical topography, lamellar grains, homogeneous, semi melted particles of  $\alpha$ -Al<sub>2</sub>O<sub>3</sub> and free from porosity, voids and cracks, as it is clear that most of the particles are spherical in form when compared to the shape of the particles before coating, and this is due to the high temperatures resulting from spraying with the plasma device, which led to the melting of the nanoparticles and their growth and solidification on the surface of the sample.

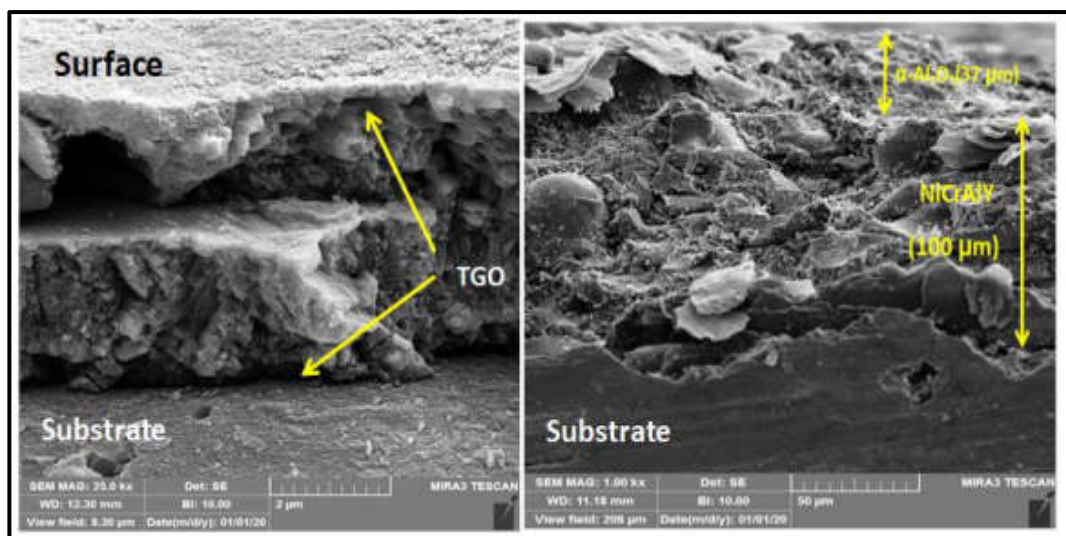


Figure 4.14: Cross section of the sample with coating before testing, at (a) 25.0 kx and (b) 1.00 kx

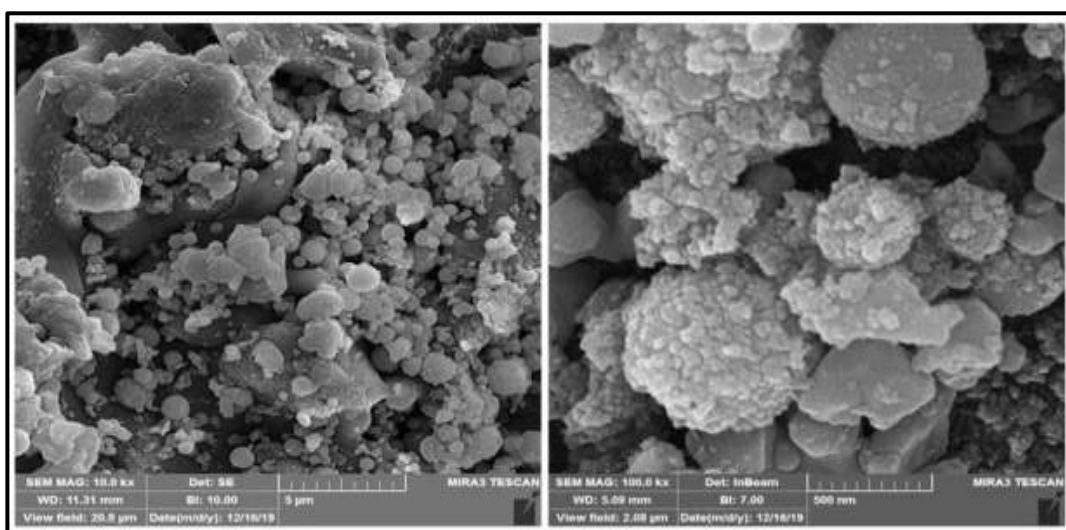


Figure 4.15: FESEM, of the sample with coating before testing, at (a) 10.0 kx and (b) 100.0 kx magnifications.

#### 4.6.8 EDS of the samples after coating and before testing

Figure (4.16) shows the energy dispersive spectroscopy (EDS) of the sample surface for sprayed coatings with  $\alpha$ -Al<sub>2</sub>O<sub>3</sub> nanoparticles. It was found from the figure that the ratio of aluminum and oxygen is very high, and this indicates that the upper surface consists of aluminum oxide only, and this is evidence of the homogeneity of the coating. It can be noted the presence of some impurities such as carbon and sodium, and this is due to the preparation of samples and their coating with a substance before being examined by FESEM.

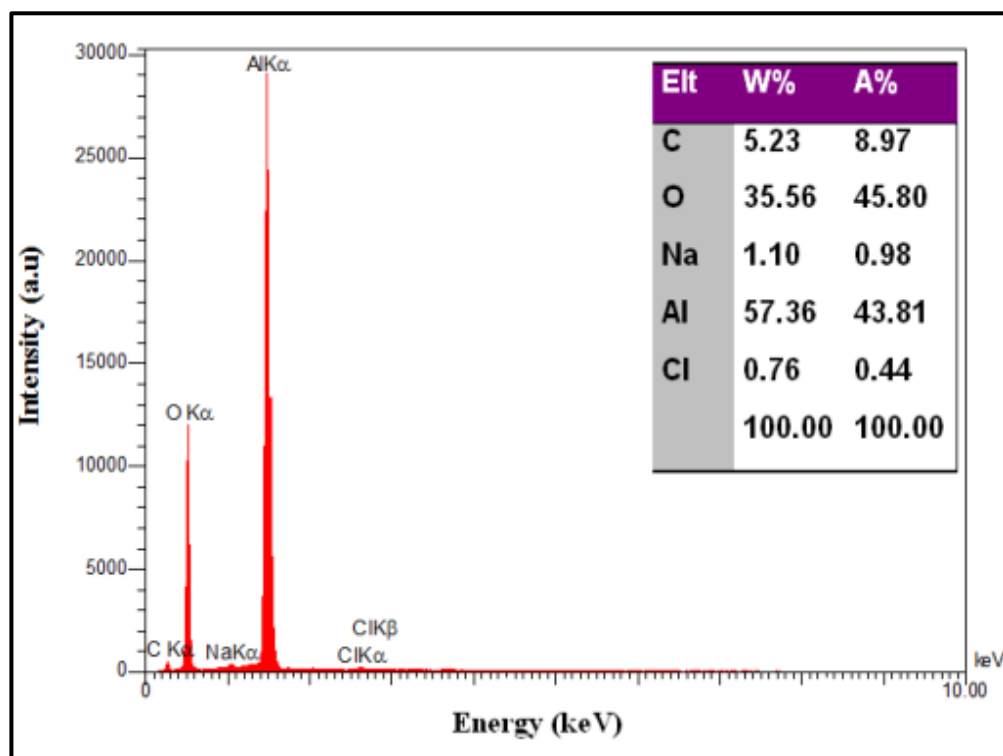


Figure 4.16: (EDS) of samples after coating and before testing.

#### 4.6.9 Vickers hardness for the surface of the samples before and after coating

Microscopic hardness (Vickers hardness) for the surface of low carbon steel samples was measured before and after coating. Table (4.4), shows the Vickers hardness values obtained. Where it was found that its value for samples of low carbon steel without coating and before testing is (208 H.v) and this value is close to the standard values for low carbon steel (304L). As for the hardness value of the Vickers of the surface samples after they were coated with  $\alpha$ -Al<sub>2</sub>O<sub>3</sub> nanoparticles by plasma spray method , it was (1387 H.v), and this result is consistent with [62, 174]. This high result proves that the ceramic nanostructures are homogeneous, the surface defects are low, and the surface is free of pores.

Table 4.4: Vickers hardness for the surface of the samples before and after coating

Samples	Vickers Hardness Number
without coating and before testing	208 H.V
coating with $\alpha$ -Al <sub>2</sub> O <sub>3</sub> nanoparticles and before testing	1387 H.V

#### 4.7 Analysis the results of the samples after Oxidation test .

Uncoated and coated low carbon steel samples were studied and analyzed after been tested at high temperatures and the absence and presence of the corrosive medium at temperatures (600,700,800, and 900°C) and at a fixed time of ( 20 h). Figure (4.17) represents photographs of samples before and after the testing.

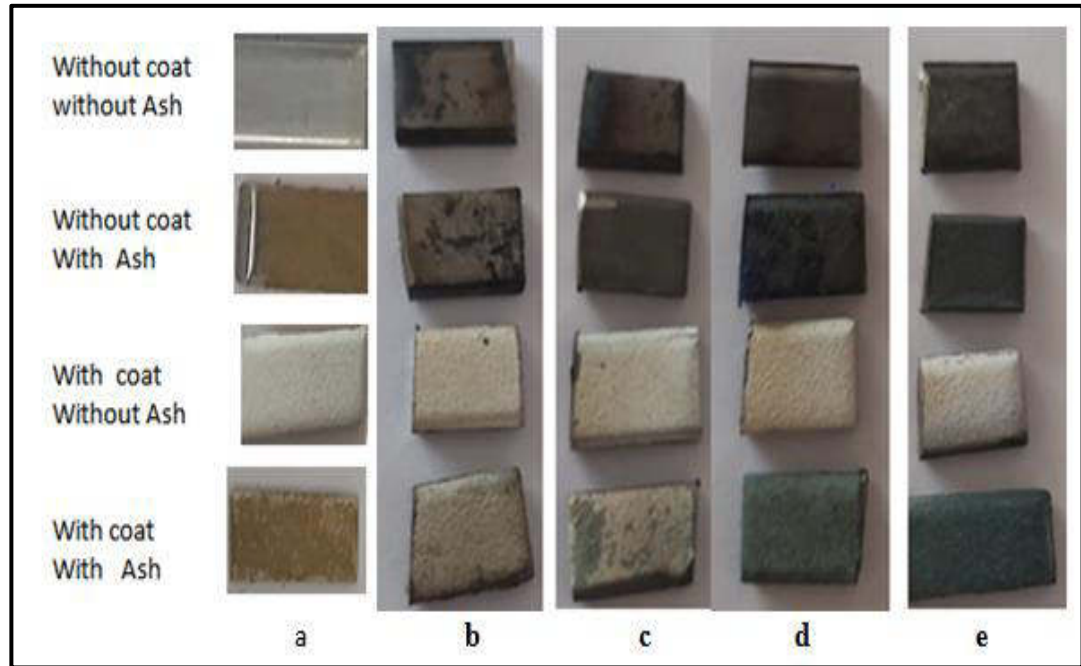


Figure 4.17: Images of samples (a) before testing, (b, c, d and e) after testing at (600, 700, 800 and 900 °C) respectively.

#### 4.7.1 FESEM and EDS of the samples without coating and without ash after oxidation test results

Figure (4.18): shows FESEM images of the surface of the sample, after testing it at 600 °C for 20 h. Where it can be noted the effect of temperature on the surface of the sample with cracks and addition to the presence of corrosion. Figure (4.19) represents the FESEM images of the surface of the sample, after testing it at 900 °C for 20 h. it can be noted the increase in the corrosion, holes and cracks, this is due to the oxidation process and this can be seen from the increase in oxygen and carbon. As well as the depletion of the nickel component in the alloy, which leads to the penetration of oxygen to the depth of the alloy and the formation of oxides that scratch the protective layer, which leads to corrosion, as shown in figure (4.20) which represents (EDS) analysis of the sample surface, after being tested at (600, 900 °C) for 20 hours [84, 171]

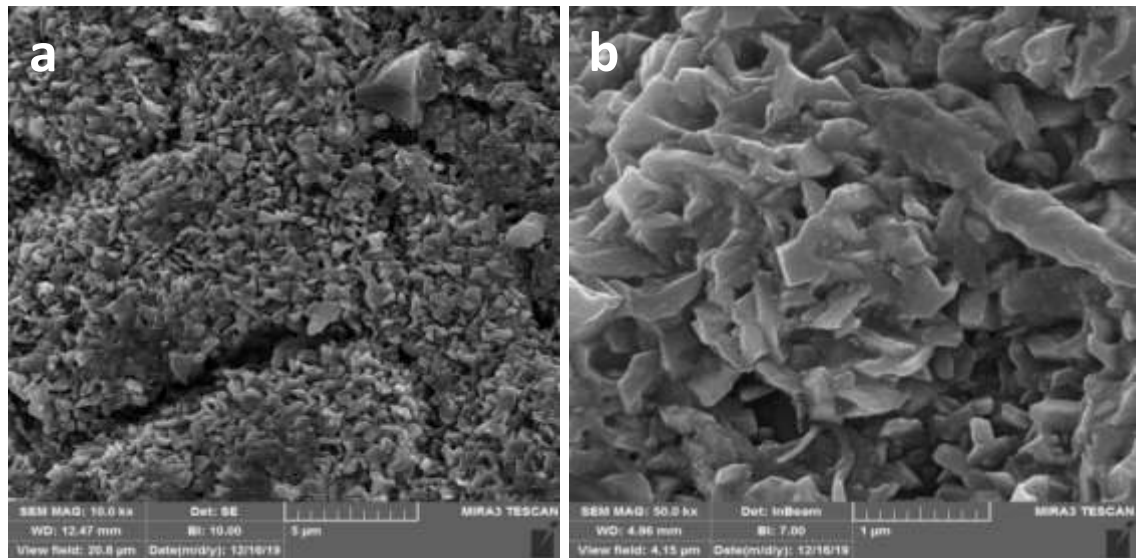


Figure 4.18: FESEM images of the samples without coating and without ash after testing at 600 °C (a) 10.0 kx and (b) 50.0 kx.

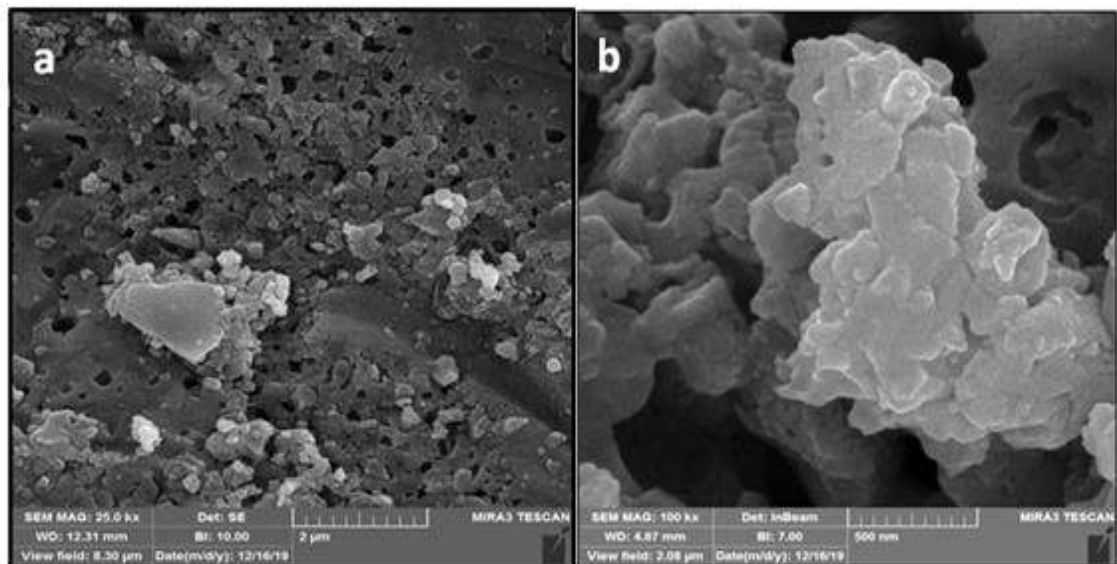
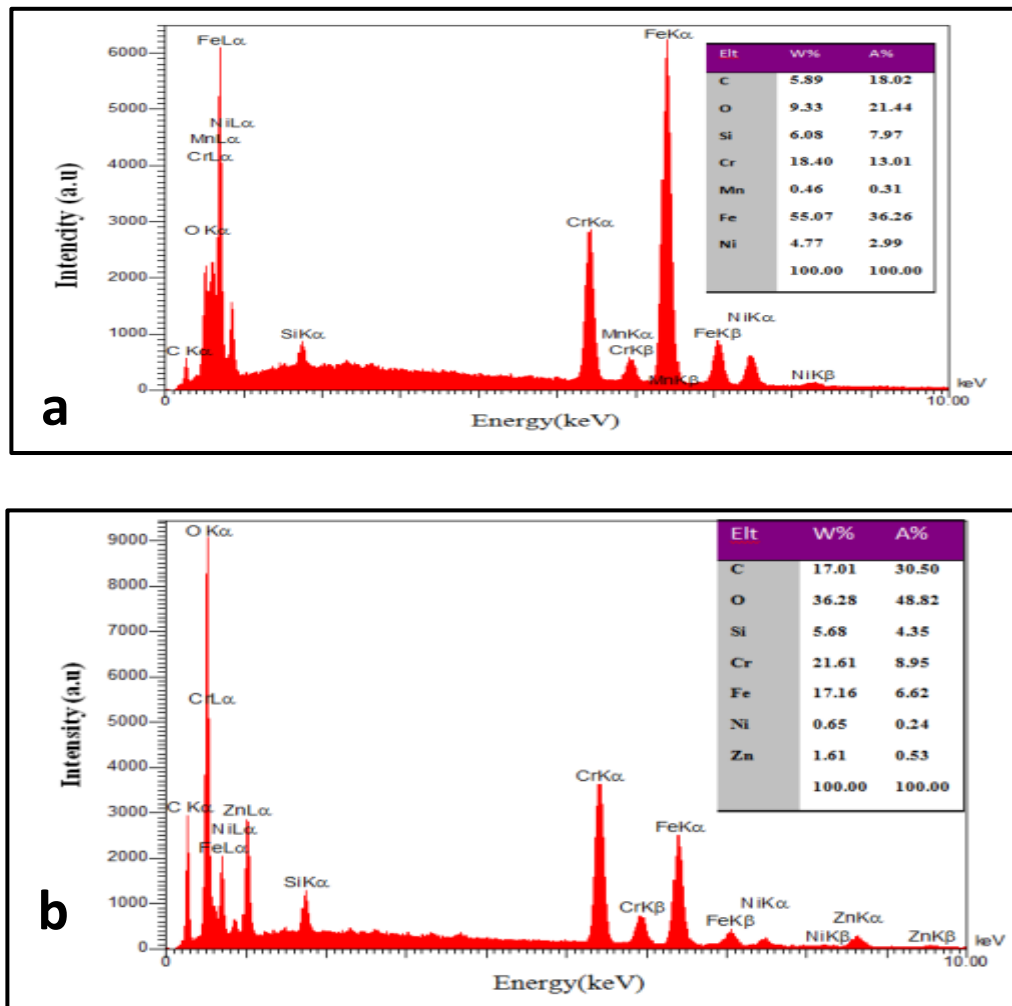


Figure 4.19: FESEM images of the samples without coating and without ash after testing at 900 °C (a) 10.0 kx and (b) 50.0 kx.



Figures 4.20 : (EDS) of samples before coating and after testing(a): at (600°C) and (b): . at (900°C).

#### 4.7.2 FESEM and EDS of the samples without coating and with ash after oxidation test results

Figures (4.21) and (4.22) shows FESEM images of the sample surface without coating and with ash erosion media (57%  $V_2O_5$ % and 43%  $Na_2SO_4$ ), after being tested at (600 and 900 °C) for 20 hours. Where it can be noted the effect of the ash layer on the surface of the sample by increasing the corrosion and the occurrence of cracks and gaps and the formation of lumps and at different depths as a result of the interaction of the salt mixture with the alloy elements.

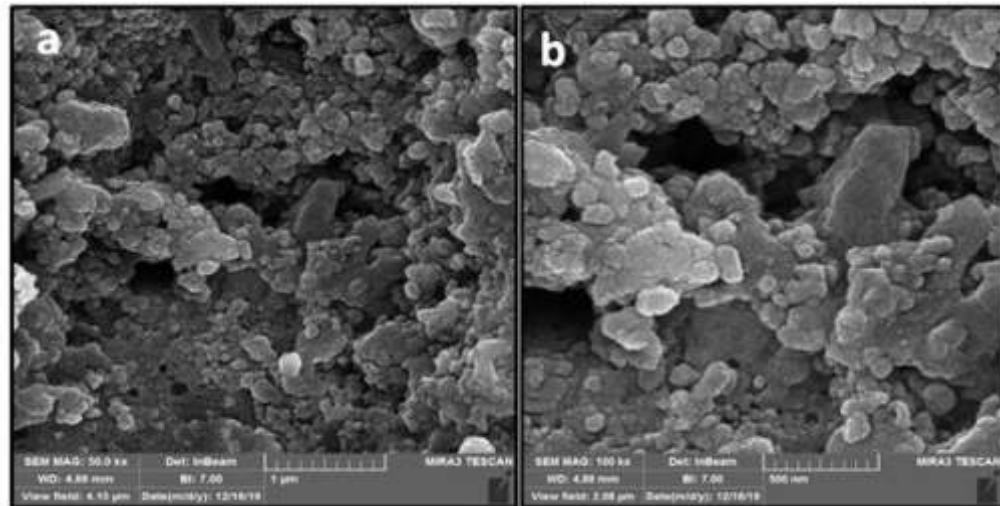


Figure 4.21: FESEM images of the samples without coating and with ash after oxidation test at 600 °C (a) 50.0 kx and (b) 100.0 kx.

Figure (4.22): FESEM images of the samples without coating and with ash after testing at 900 °C (a) 25.0 kx and (b) 100.0 kx magnifications. The figure shows a rapid decomposition, and the rate of corrosion increases significantly, due to the formation of vanadic compounds such as ( $\text{Na}_2\text{O}\cdot\text{V}_2\text{O}_5$ ,  $\text{NaVO}_3$  and  $\text{Na}_2\text{O}\cdot 6\text{V}_2\text{O}$ ), that causes the dissolution of the protective layer. Also the Figure (4.22) shows that, clusters are formed with regular geometric shapes, and these are due to the compounds formed when the salt mixture interacts with the alloy components. These results are consistent with [84, 85, 174, 175].

Figure 4.23 represents the EDS for the surface of the samples after being tested at temperatures of 600 and 900 and with ash. The results shows that the components of the alloy and there's an increase in the percentage of oxygen and the low forgotten iron, nickel and chrome compared to the analysis of the alloy components before the test as well as after the test without ash, and this is due to the occurrence of corrosion and weight loss. The results also shows that, the vanadium element does not appear in the test case at 600 °C, but it appear in the case of sample testing

at 900 °C degrees, due to the melting of the ash mixture at a temperature higher than 600 °C [174, 175].

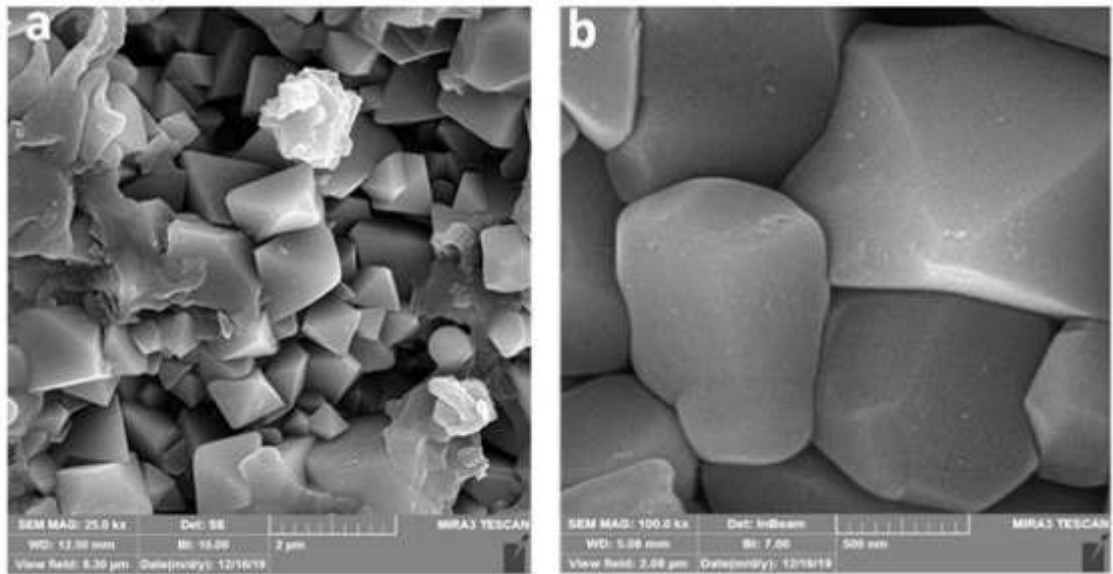


Figure 4.22: FESEM images of the samples without coating and with ash after oxidation test at 900 °C (a) 25.0 kx and (b) 100.0 kx.

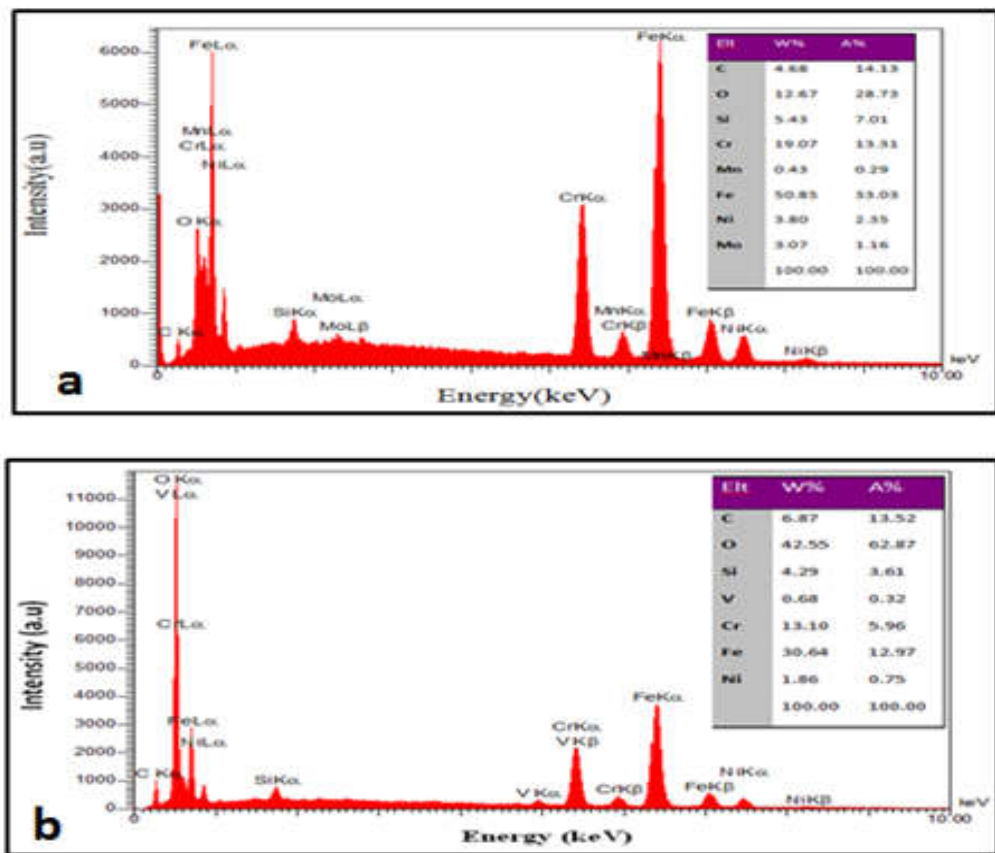


Figure 4.23: EDS of the samples without coating and with ash at (a) 600 °C and (b) 900 °C .

---

### 4.7.3 XRD of the samples with coating and without ash after oxidation test results

Figure (4.24) illustrates the XRD patterns of the samples with binding and top layer samples using plasma spray technology, and without the presence of corrosive medium (ash), after testing the samples at temperatures (600, 700, 800 and 900 °C) and for a fixed time of 20 hours. By comparing the XRD of the for  $\alpha$ -Al<sub>2</sub>O<sub>3</sub> nanoparticles before coating and with the diffraction patterns of the samples after coating and before testing, it was found that the upper ceramic nanostructures were not affected when tested with high temperatures, as diffraction patterns of other elements did not appear, only some phases of  $\gamma$ -Al<sub>2</sub>O<sub>3</sub> appeared at ( $2\theta \sim 37.5^\circ$ ,  $45.7^\circ$  and  $66.6^\circ$ ), and these values correspond exactly to the ICDD card number (00 -010-0173) from  $\gamma$ -Al<sub>2</sub>O<sub>3</sub>. The reason for the emergence of the new peaks is the exposure of the nanomaterial to high temperatures, whether during the thermal coating process with plasma spray technology or as a result of testing conditions at high temperatures for a period of 20 hours. This means that the top coating did not get corrosive and was a good heat insulator of bonding layer and substrate. From these results, it is clear that the plasma spray technique is very effective for obtaining ceramic layers on metals, after using a bonding layer between them, and that these layers are good thermal insulation at high temperatures so it can be used to protect the metals from corrosion, especially the hot corrosion. Corrosion rate and coating efficiency will be investigated in the following paragraphs.

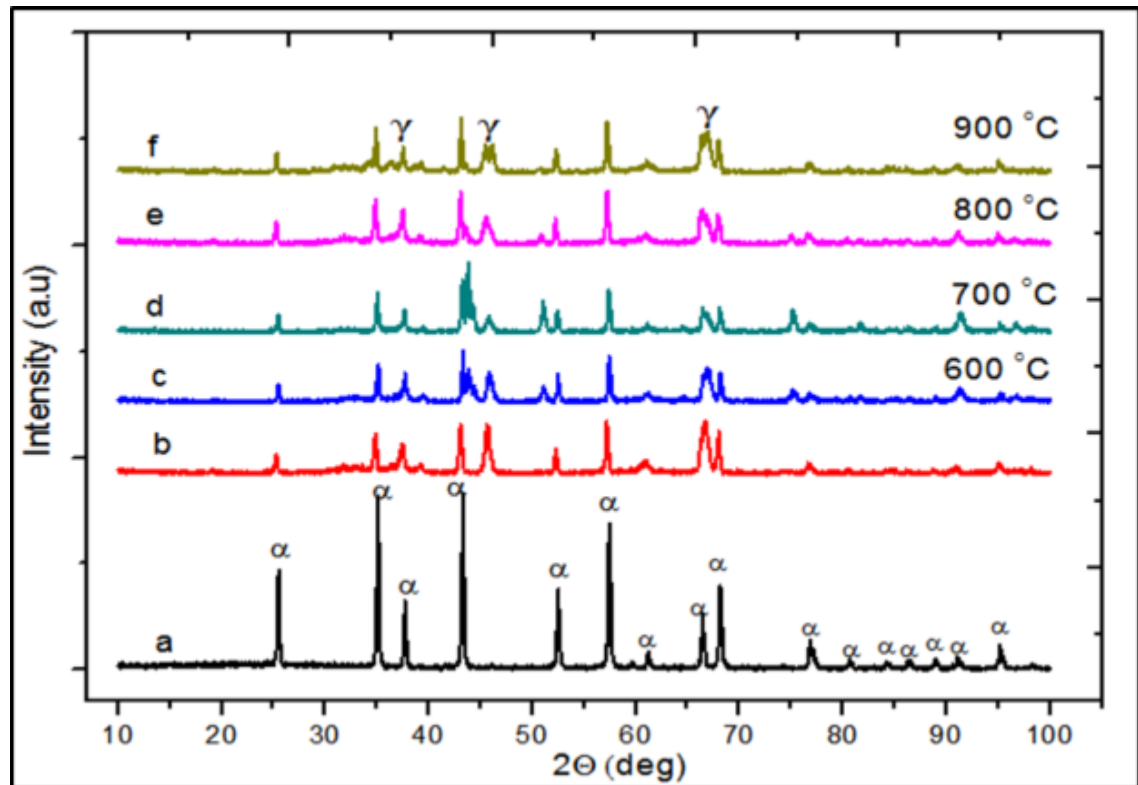


Figure 4.24: XRD patterns of (a)  $\alpha$ -Al<sub>2</sub>O<sub>3</sub> powder, (b) sample with coating before testing, c, d, e, and f samples with coating and without ash after 20 h, at 600, 700, 800, and 900 °C respectively.

#### 4.7.4 Calculation of interplanar spacing ( $d_{hkl}$ ) of the samples with coating and without ash after oxidation test results

Interplanar spacing with the same Miller indices of samples after coating and testing at 600, 700, 800, and 900 °C has been calculated by reference to the Bragg's law and the equation (2.6). Where it was found from the results that, the value of ( $d_{hkl}$ ) is slightly greater than the results of the coated samples before the test, as it was found that they are consistent with the values of the international card (00-010-0173) and (00-050-0741), as shown in Table (4.4) .

#### 4.7.5 The crystallite size ( $D_{av}$ ) of the samples with coating and without ash after oxidation test results

The average crystallite size of samples with coating and without ash after oxidation test at 600, 700, 800, and 900 °C, is calculated, by means of the Scherrer formula and the W.H analysis, by relation (2.9) and (2.12)

---

respectively. It has been observed that the crystalline volume according to Scherer's method ranges between (37.4, 30.5, 35.5, and 36.4 nm), and according to Williamson Hall analyzes, it ranges between (20.9, 24.6, 20.4, and 28.1 nm), as shown in Table (4.5). It is noted that the crystalline size is greater than the crystallite size of the samples after coating and before testing. From the results it was found that the value of microstrain is negative and decreases while the crystal size increases, and this is the reason that the crystalline size in the W.H analysis is less than Scherer's formula as shown in Figure (4.25) [169].

#### 4.7.6 Dislocation Density ( $\delta$ )

The dislocation density of the samples with coating and without ash after the oxidation test was calculated according to equation (2.10), the dislocation strength was found to decrease as crystallite size values increase, as shown in Table (4.5).

#### 4.7.7 Texture coefficient $TC_{(hkl)}$

The texture coefficient of the samples with coating and without ash after oxidation was calculated using equation (2.14). It has been found that its value is greater than one and this means that the polycrystalline nanoparticles have more dominance than other directions [170], as shown in Table (4.5).

#### 4.7.8 Specific Surface Area (SSA)

The specific surface area (SSA) of the samples with coating and without ash after oxidation has been calculated using equation (2.17). It was found to decrease with increasing size of crystallite, determined by methods of Scherrer and Williamson Hall, as shown in Table (4.5).

Table 4-5: Some parameters of the results obtained from X-ray diffraction of the samples with coating and without ash before and after the oxidation test

Structural parameters		Al <sub>2</sub> O <sub>3</sub> Powder	Before Testing	600 °C	700 °C	800 °C	900 °C
D <sub>av</sub> (nm)	Scherrer	33.9	18.3	36.4	35.5	30.5	37.4
	W.H	27.7	20.3	20.9	24.6	20.4	28.1
$(\delta)$ $*10^{-4} (\text{nm}^{-2})$	Scherrer	8.694	29.85	7.54	7.93	10.75	7.15
	W.H	13.03	24.27	24.26	16.52	24.1	12.66
(SSA) (m <sup>2</sup> .g <sup>-1</sup> )	Scherrer	45.38	84.069	42.1	43.34	50.44	41.14
	W.H	55.54	75.79	73.62	62.54	75.41	54.75
The lattice constants (Å)	a <sub>0</sub>	4.761	4.77	4.75	4.76	4.82	5.12
	c <sub>0</sub>	12.978	12.65	13	12.39	12.79	13.3
Micro Strain (S) * 10 <sup>-3</sup>		-1.13	+1.07	-1.7	-0.93	-0.37	-0.82
T <sub>c (hkl)</sub>		0.96	1.2	1.01	1.16	0.81	0.87

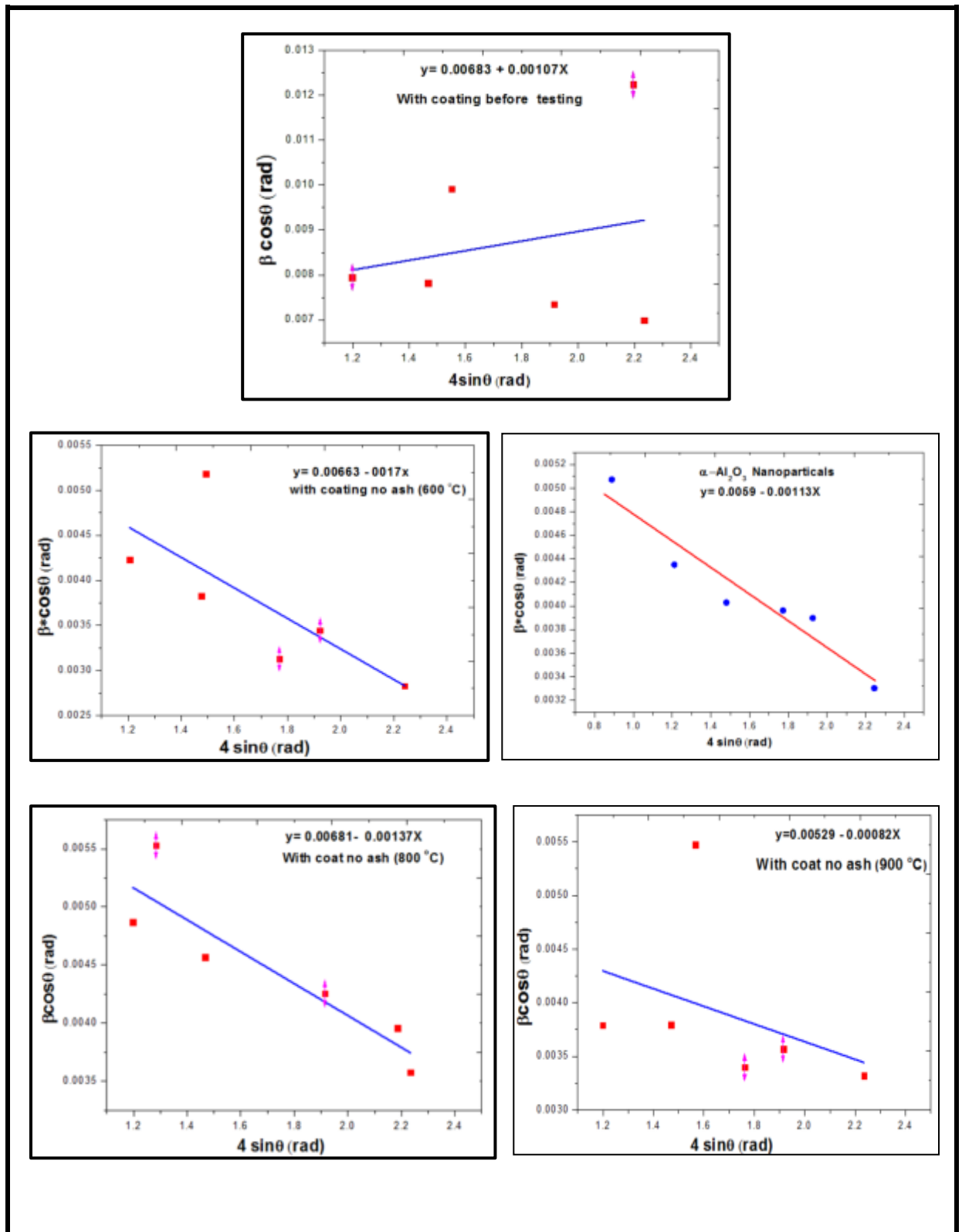


Figure 4.25: The W-H analysis of the samples surface with coating and without ash after testing at ( 600, 700, 800 and 900 °C).

#### 4.7.9 FESEM of the samples with coating and without ash after oxidation test results

Figures (4.26, 4.27, 4.28 and 4.29) show the FESEM images of the sample surface with coating and without ash the after oxidation test at (600, 700, 800 and 900 °C). It was found that, there is no effect of temperature on the surface of the samples, and there is an improvement in the nature of the upper coating layer by noting that the shapes turned spherical and no cracks or corrosion were observed in the coating layer. It was found that clearly in the cross-section images of the samples after coating and testing and without ash at (600 and 900 °C) as in Figures (4.30 a and b), where it was found that clearly in the cross-section images of the samples after coating and testing and without ash the consistency of the upper coating layer with the bonding layer and with the substrate, and this is consistent with the photographs of the samples after the test where the color did not change Samples. As in Fig. (4.17).

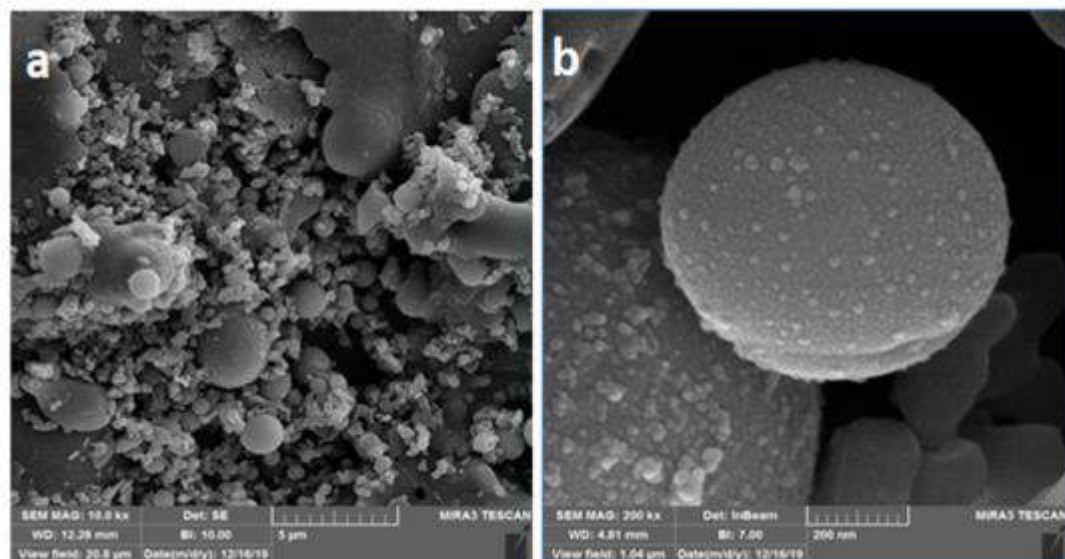


Figure 4.26: FESEM, of the sample with coating and without ash after oxidation testing, at 600 °C (a) 10.0 kx and (b) 200.0 kx magnifications.

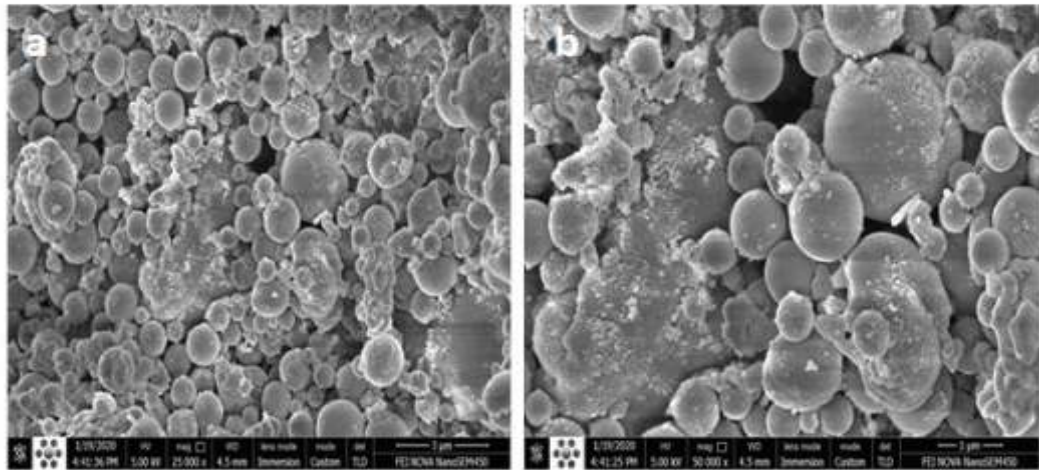


Figure 4.27: FESEM images of the samples with coating and without ash after testing at 700 °C (a) 25.0 kx and (b) 50.0 kx magnifications.

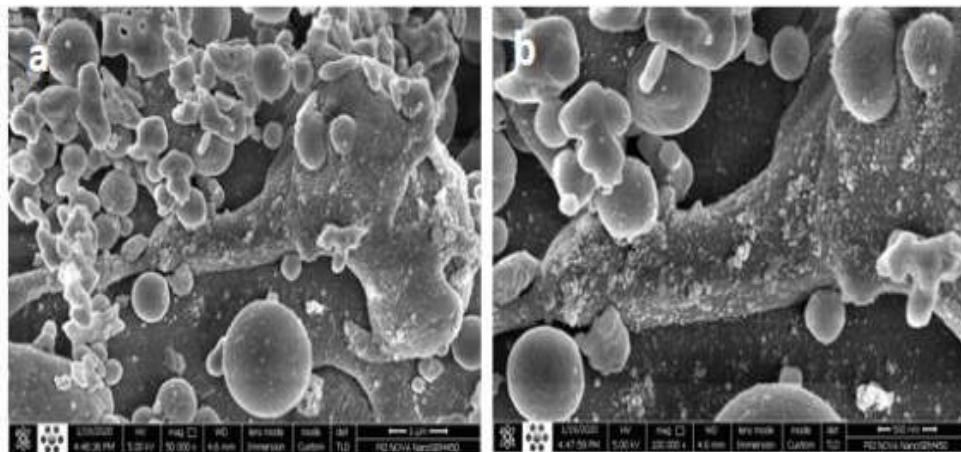


Figure 4.28: FESEM images of the samples with coating and without ash after testing at 800 °C (a) 50.0 kx and (b) 100.0 kx magnifications.

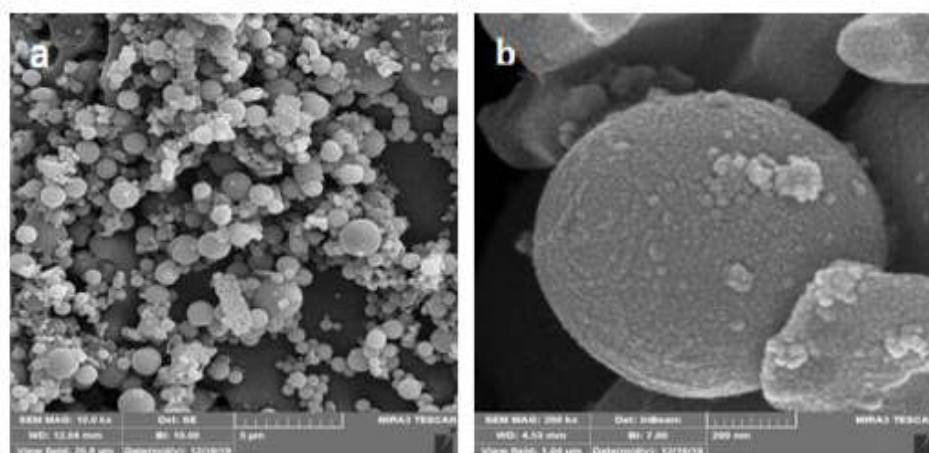


Figure 4.29: FESEM images of the samples with coating and without ash after testing at 900 °C (a) 10.0 kx and (b) 200.0 kx magnifications.

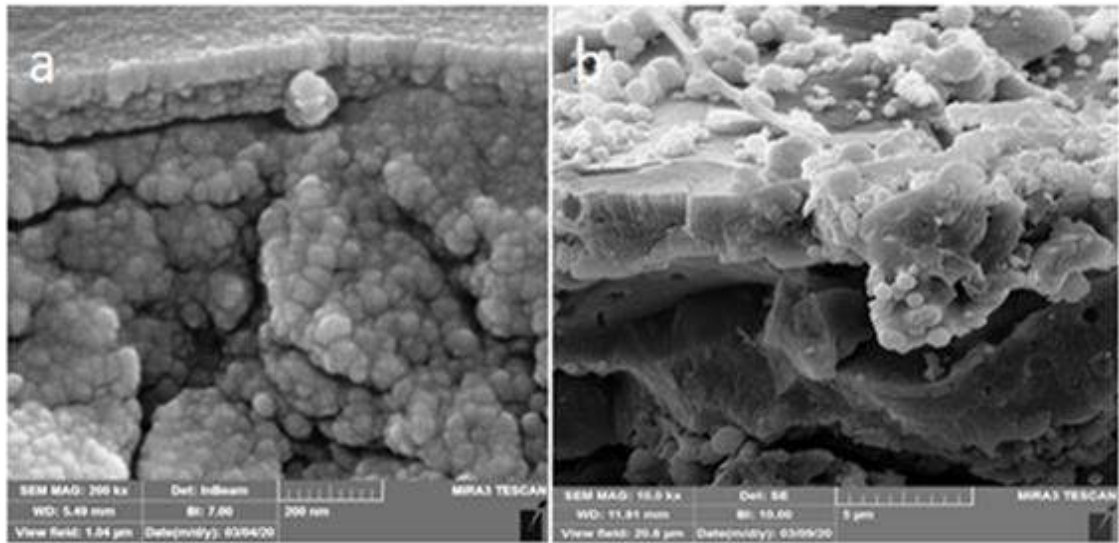


Figure 4.30 : Cross- Section FESEM images of the samples after coating and testing without ash at , (a): (600 °C) and (b) (900 °C).

#### 4.7.10 EDS of the samples with coating and without ash after testing

Figure 4.31 shows the energy dispersive spectroscopy (EDS) of samples with coating and without ash after testing at (600 and 900° C). It was found from the figure that the percentage of aluminum and oxygen are very high. When comparing these results with the results of the EDS of the nanoparticles prepared before coating and with the coating layer before the test, there are no new elements.

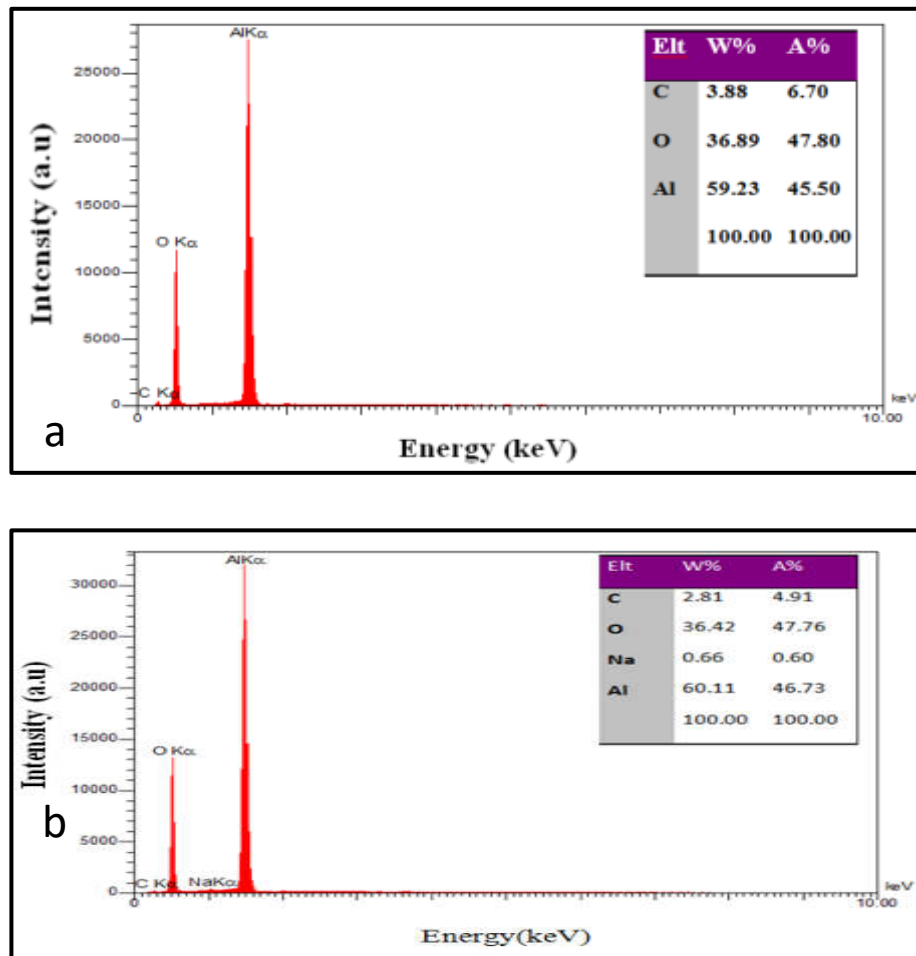


Figure 4.31: EDS of the samples with coating and without Ash after testing at (a) : (600 °C) and (b) (900 °C).

#### 4.7.11 XRD of the samples with coating and with ash after oxidation test results

Figure 4.32 illustrates the XRD patterns of ash-coated samples. The diffraction patterns of the coated samples were compared before and after oxidation test in the presence of ash at temperatures of 600 and 700 °C for 20 hours as in (Figure 32 (b and c)), it was found that, the diffraction patterns at 600 °C were affected slightly, which means that the upper layer of the coating did not corrode, while at 700 °C diffraction patterns show the formation of new compounds, such as  $(AlCr)_2O_3$  at  $2\theta \sim 57.16$ . These values correspond to the ICDD card number 00-050-

741 and AlNi at  $2\Theta \sim 58.76$ , which corresponds to the ICDD card number 00-051-1394. This indicates an interaction between the upper coating layer and the binder due to the effect of ash compounds, which means that the upper coating has corrosion or crack.

Figure (4.33) represents XRD patterns for samples coated with ash at 800 and 900 °C for 20 h. The formation of new compounds has been observed, such as  $\text{Al}_2\text{FeO}_4$ ,  $\text{AlV}_2\text{O}_4$ ,  $\text{FeNiAlO}_4$ ,  $\text{Fe}_3\text{O}_4$  and  $\text{CCrFeNi}$ , and they correspond to the card numbers from 0034-0192, 025-0026, 0052-1079, 0026-1136 and 0034-0140, respectively. The reason for the appearance of these compounds is the occurrence of cracking in the upper coating layer, which led to the interaction with the bonding layer that led to the formation of these compounds.

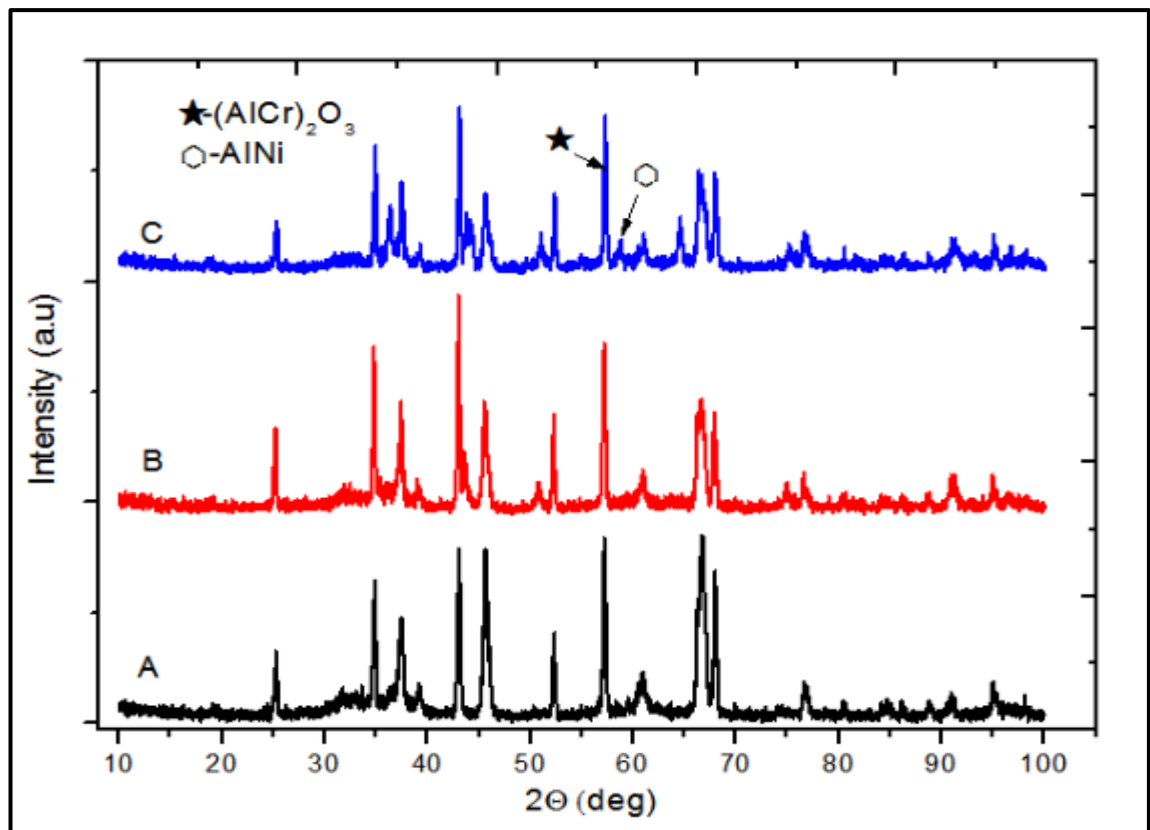


Figure 4.32: XRD patterns of (A) sample with coating before testing, (B and C) samples with coating in presence of fuel ash after 20 h at 600, and 700 °C respectively.

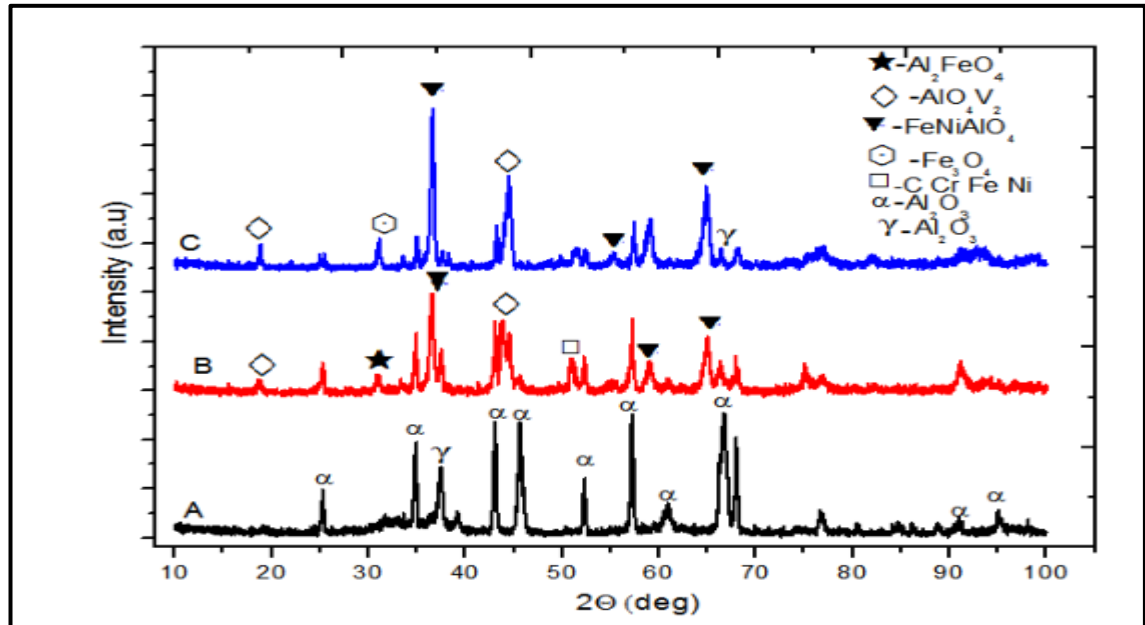


Figure 4.33: XRD patterns of (A) sample with coating before testing: (B and C) samples with coating in presence of fuel ash after 20 h at 800 and 900 °C respectively.

#### 4.7.12: FESEM and EDS of the samples with coating and with ash after oxidation test results

Figures (4.34, 4.35, 4.36 and 4.37) show the FESEM images of the sample surface with coating and with ash after the oxidation test at (600, 700, 800 and 900 °C). Significant effect on the sample surface was observed. This is due to the interaction of ash compounds with the alumina nanoparticle at high temperatures. Cracks and pores in the surface of the sample were observed due to the fusion of the ash mixture and reaction with the coating layer. Furthermore the presence of cracks in coating layers enhances the penetration of oxygen to steel surface; hence, corrosion rate is increased. This is consistent with the results of the XRD as shown in figure (4.30 and 4.31).

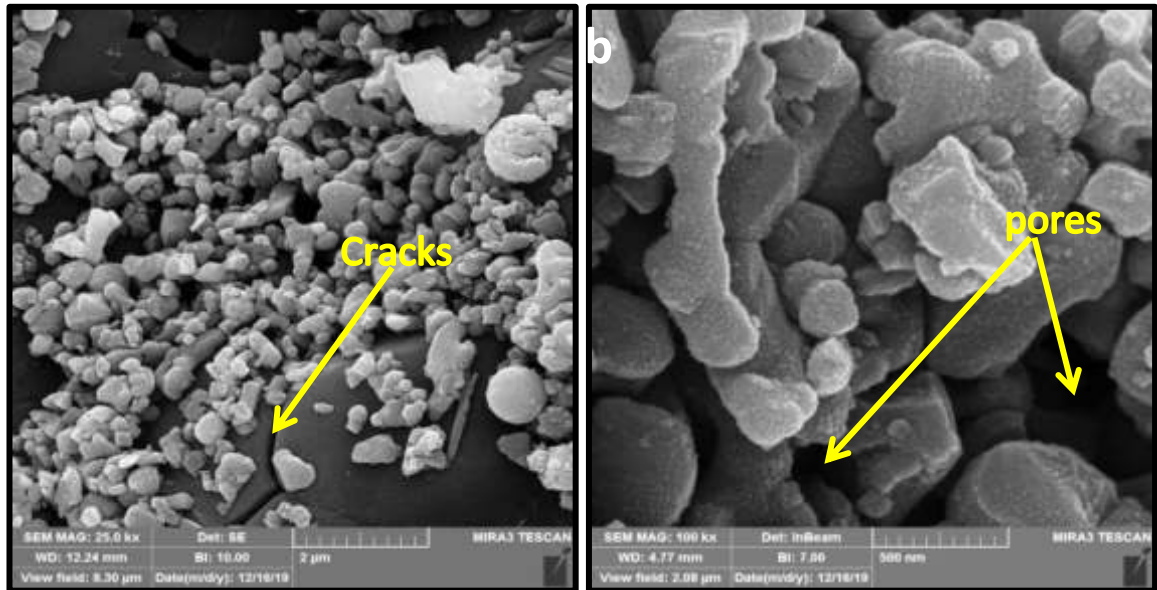


Figure 4.34: FESEM images of the samples with coating and with ash after testing at 600 °C (a) 10.0 kx and (b) 200.0 kx magnifications.

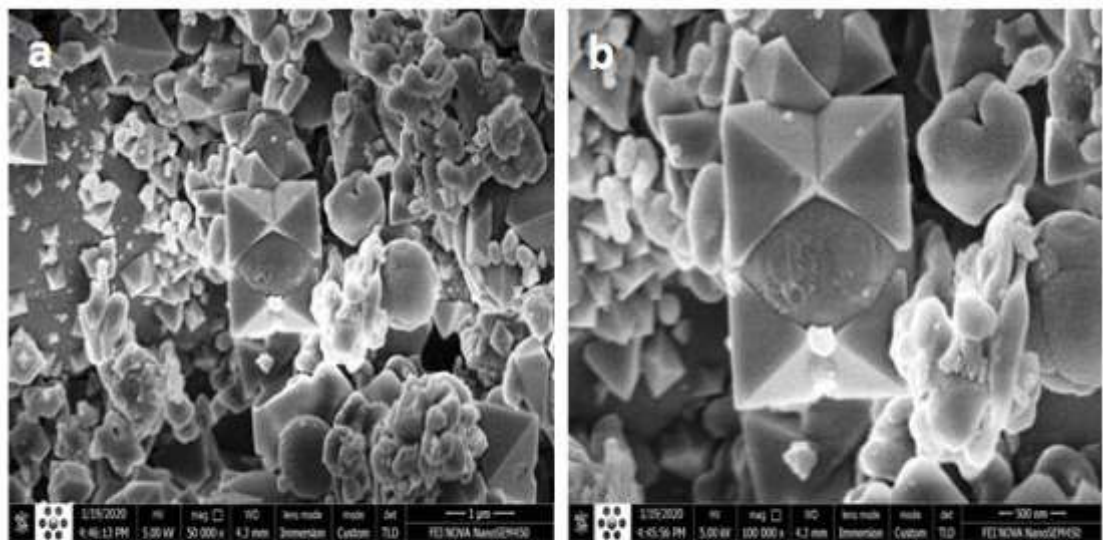


Figure 4.35: FESEM images of the samples with coating and with ash after testing at 700 °C (a) 50.0 kx and (b) 100.0 kx magnifications.

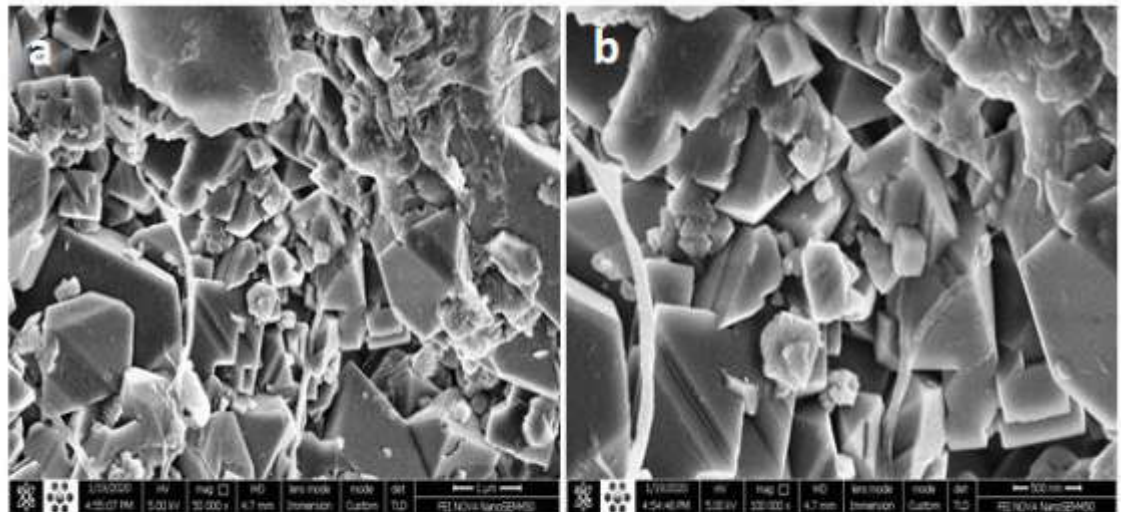


Figure 4.36: FESEM images of the samples with coating and with ash after testing at 800 °C (a) 50.0 kx and (b) 100.0 kx magnifications.

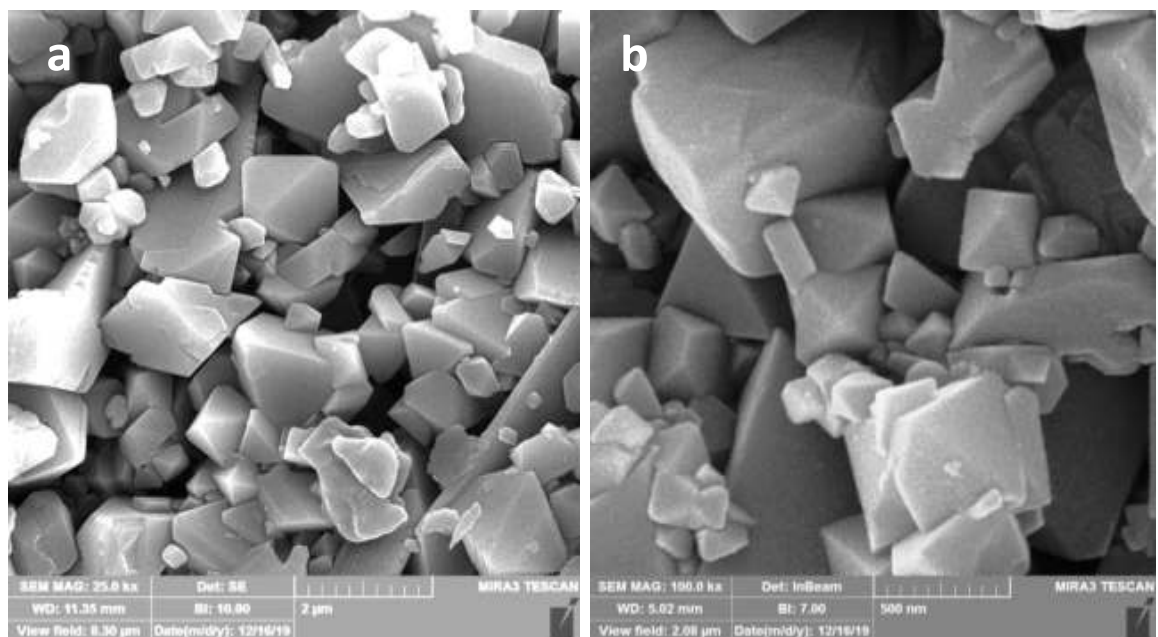


Figure 4.37: FESEM images of the samples with coating and with ash after testing at 900 °C (a) 25.0 kx and (b) 100.0 kx magnifications.

Figure (4.38 a and b) shows FESEM cross-section images of samples after coating at (600 and 900°C). Where we notice cracks have formed between the bonding layer and the substrate, due to the difference in the thermal conductivity coefficient between the bonding coating layer and the substrate, as well as the effect of oxidation and oxygen penetration between the two layers of the non-coated side edges. These results are in agreement with [176, 177].

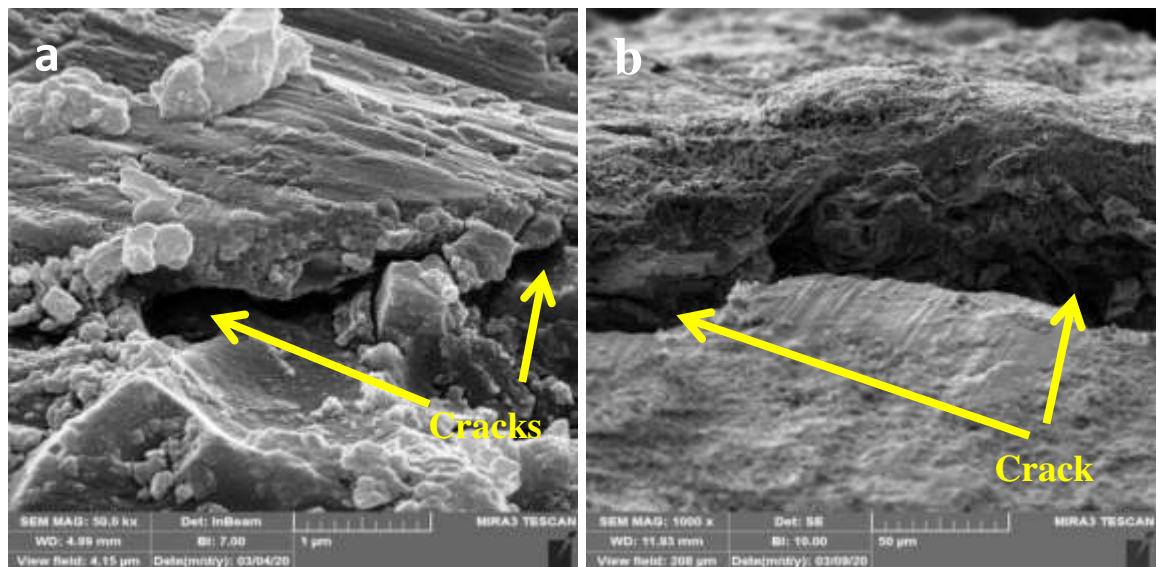


Figure4.38: FESEM cross section images of the samples with coating and with ash after testing at (a) 600 °C and (b) 900 °C .

Figure (4.39 a and b) show EDS analysis of coating layers in absence and presence of fuel ash. New compounds were formed due to the reaction of fuel ash with coating layers.

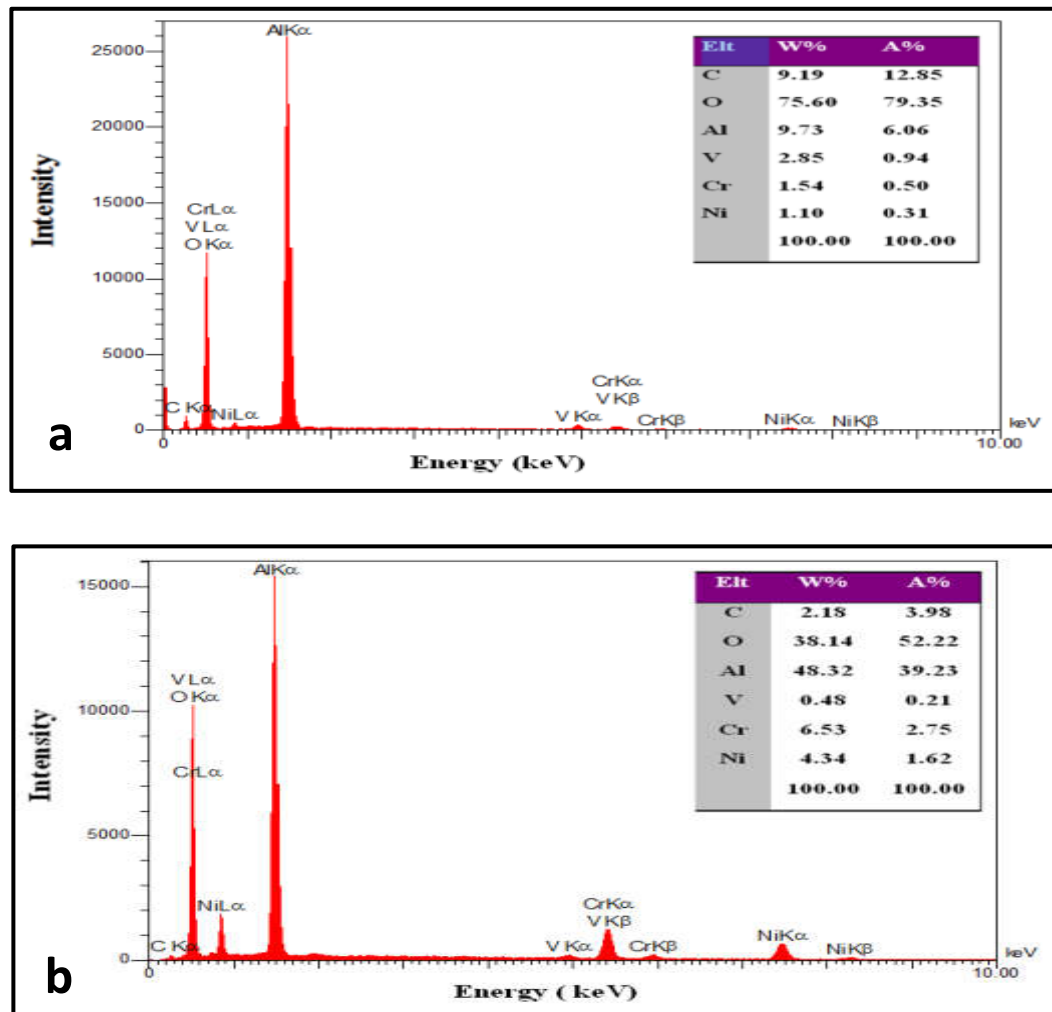


Figure (4.39): EDS of the samples with coating and with Ash after testing at (a) : (600 °C) and (b) (900 °C).

## 4.8 Corrosion Measurements

Hot corrosion of uncoated and coated samples was studied in the presence and absence of ash at different temperatures from 600, 700, 800 and 900 °C for 20 hours. Table (4.5) shows the results obtained, through which the corrosion rate, coating efficiency and activation energy were calculated.

### 4.8.1 Corrosion rate measurements

Table (4.6) and Figure (4.40) shows the relation between corrosion rate and temperature. The results show that the corrosion rate increases with

increasing temperatures and presence of fuel ash. It was found that, the lowest rate of corrosion is for coated samples and without ash, and the highest corrosion rate for uncoated samples is in the presence of ash. From these results, it is clear that the (NiCrAlY) as a bonding layer and  $\alpha\text{-Al}_2\text{O}_3$  nanoparticles as top layer is very effective to protect the low carbon steel from hot corrosion in the absence of ash and in its presence. Also, it was found that the thermal plasma spray technology can be obtained from coherent coating layers. It is possible to obtain thermal insulation layers. These results are consistent with the results of XRD, FESEM and EDS that were explained in the previous paragraphs.

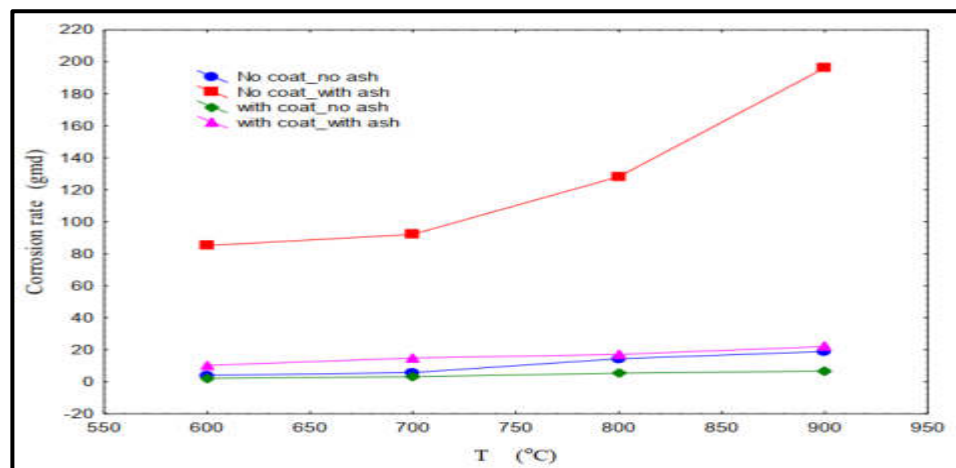


Figure. 4.40: Corrosion rate as a function of temperature.

#### 4.8.2 Coating Efficiency (% IEC)

The coating efficiency of the samples was calculated due to the absence and presence of ash. The results show that the coating efficiency ranged from (44% to 82%) for absence of fuel ash and (84% to 88%) for presence of fuel ash as shown in the table (4.6) and figure (4.41). Therefore, the coating layers can be used as a thermal insulation material and prevent oxidation of the metal surface.

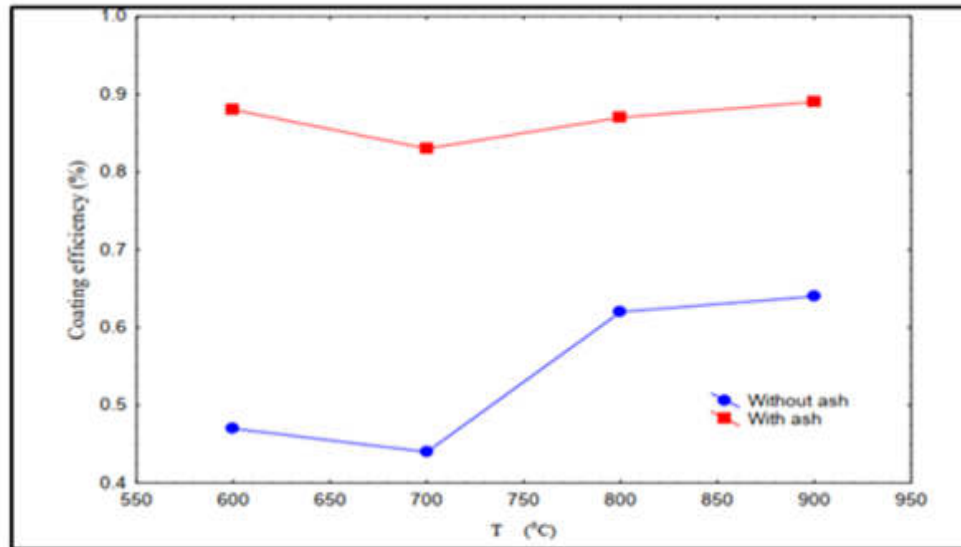


Figure 4.41: Coating Efficiency as a function of temperature

### 4.8.3 activation energy ( $E_a$ )

The activation energy ( $E_a$ ) and frequency factor ( $A$ ) of the coated and uncoated samples in the absence and presence of ash was calculated to study the coating action kinetics in a hot environment at different temperatures by the Arrhenius equation as shown in Fig.(4.42). Table (4.7) shows the values of the activation energy. As the activation value was higher in the absence of ash in the case of coated and uncoated samples. The reason for this may be due to the fact that the reactions need more energy to occur, while the value of the activation energy was lower in the presence of ash. We note that the activation energy of the samples is without coating and without ash ( $67.98 \text{ kJ.mol}^{-1}$ ). And with ash there was ( $23.45 \text{ kJ.mol}^{-1}$ ). While we note that the activation energy value of the coated samples without ash is ( $38.28 \text{ kJ.mol}^{-1}$ ) and the presence of ash ( $21 \text{ kJ.mol}^{-1}$ ). This explains the reason for the increased rate of corrosion in the presence of ash, as it requires little energy for reactions to occur. These results are consistent with the results of the literature [178-180].

Table 4.6: Corrosion rate and Coating efficiency data at different conditions.

Samples	Area cm <sup>2</sup>	T °C	W <sub>1</sub> g	W <sub>2</sub> g	W <sub>1</sub> -W <sub>2</sub> g	C.R gmd	% eff coat
No Coat And No Ash	8.376	600	6.5642	6.5614	0.0028	<b>4.015</b>	—
	8.4	700	6.3766	6.3726	0.0040	<b>5.714</b>	—
	8.753	800	6.7813	6.7708	0.0105	<b>14.395</b>	—
	9.353	900	7.4416	7.4059	0.0353	<b>45.29</b>	—
No Coat And with Ash	7.74	600	6.9517	6.8968	0.0550	<b>85.271</b>	—
	8.568	700	6.6492	6.5834	0.0658	<b>92.157</b>	—
	8.770	800	6.6903	6.5966	0.0937	<b>128.21</b>	—
	8.566	900	6.4515	6.3109	0.1406	<b>196.96</b>	—
With Coat And No Ash	8.477	600	6.7595	6.7580	0.0015	<b>2.123</b>	<b>47 %</b>
	9.022	700	7.2126	7.2102	0.0024	<b>3.192</b>	<b>44 %</b>
	8.972	800	7.0038	6.9998	0.0040	<b>5.350</b>	<b>63 %</b>
	8.613	900	6.5068	6.5020	0.0058	<b>8.08</b>	<b>82 %</b>
With Coat And with Ash	8.596	600	7.2340	7.2267	0.0073	<b>10.19</b>	<b>88 %</b>
	8.230	700	6.2423	6.2321	0.0102	<b>14.87</b>	<b>84 %</b>
	9.278	800	7.0268	7.0136	0.0132	<b>17.07</b>	<b>87 %</b>
	8.613	900	6.6657	6.6499	0.0158	<b>22.01</b>	<b>88 %</b>

Table 4.7: Activation energy at different conditions.

Case	Slope	Intercept	Ea (kJ.mol <sup>-1</sup> )
Without coating and without ash	-8181	10.498	67.98
Without coating and with ash	-2822	7.569	23.45
With coating and without ash	-4606	5.977	38.28
With coating and with ash	-2519	5.230	21.5

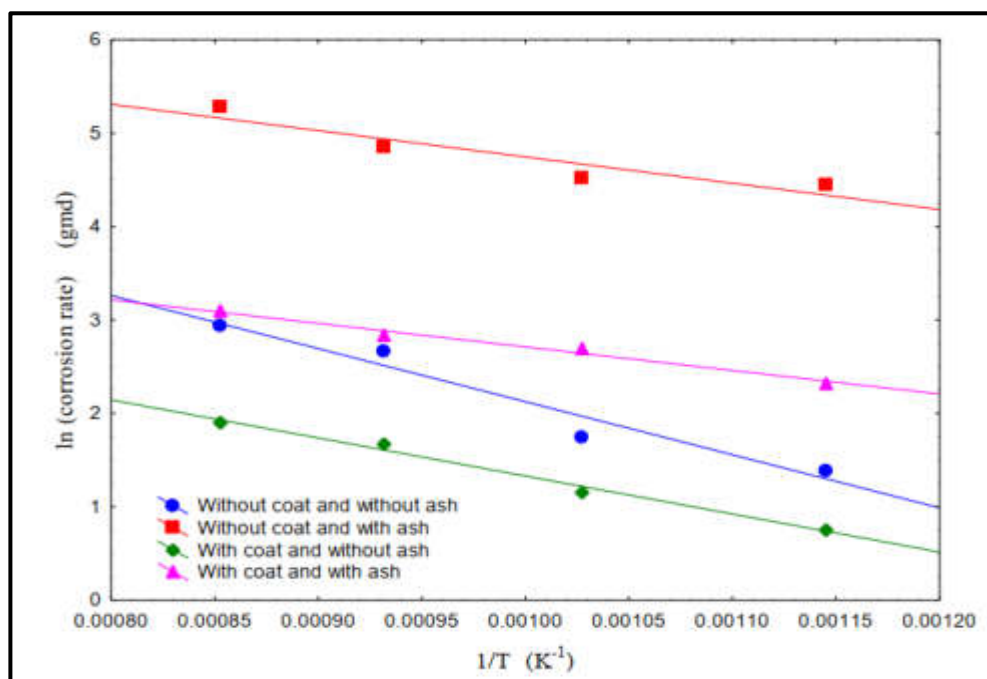


Figure 4.42: Arrhenius plots for oxidation of the samples.

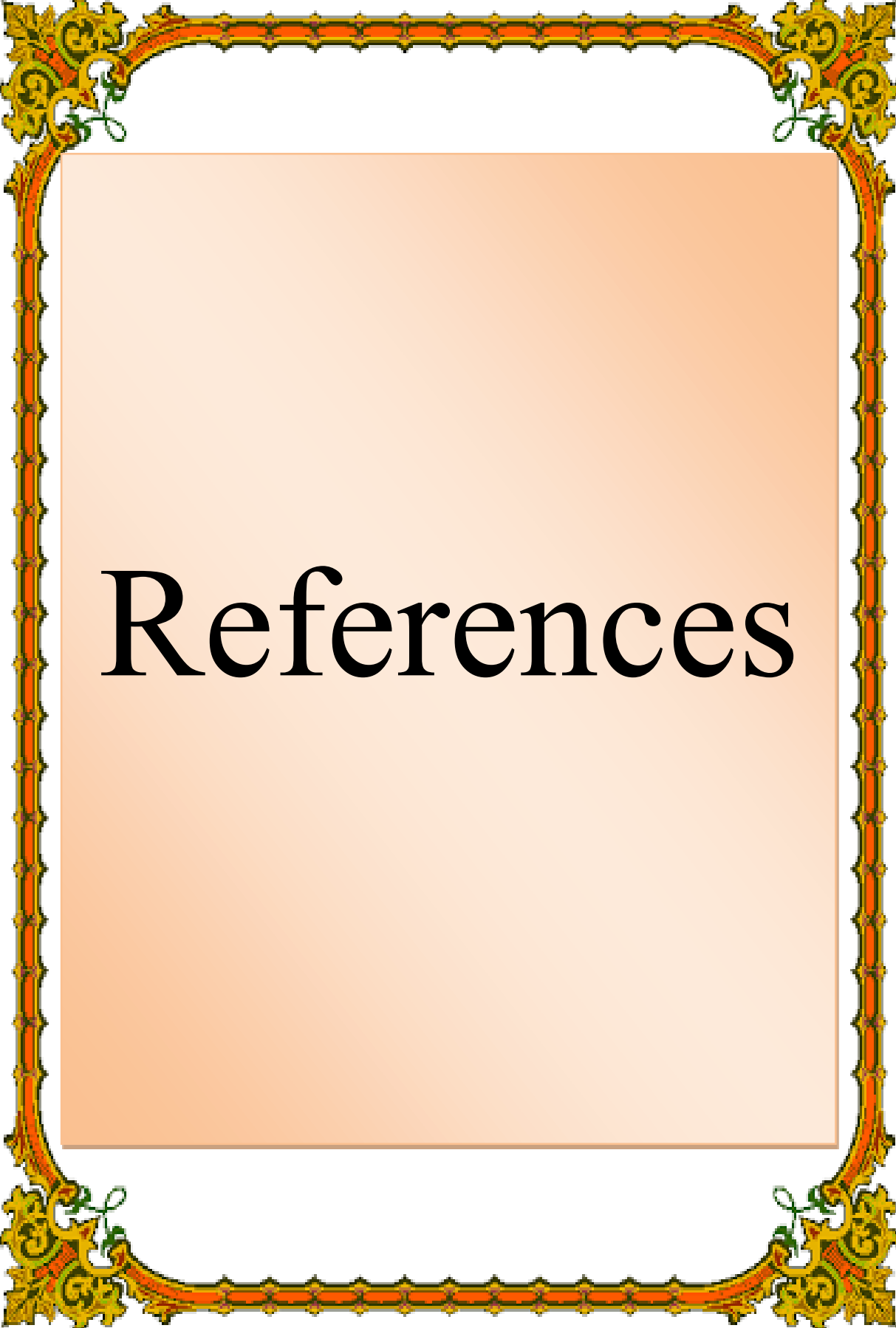
## 4.9 Conclusions

1. Sol-gel method has proven successful for preparing nanomaterials in powder form, such as,  $\alpha$ -Al<sub>2</sub>O<sub>3</sub> nanoparticles.
2. A good coating layer can be obtained by using plasma spray to protect the austenitic stainless steel against high temperature corrosion. It consists of two layers, the first alloy component of NiCrAlY as a binding coating layer and the top layer is  $\alpha$ -Al<sub>2</sub>O<sub>3</sub> nanoparticles.
3. The results have proven that, the thermal plasma spray technique is very effective to obtain high-quality ceramic coatings free from cracks and pores.
4. The results prove that thermal barrier coatings are very effective for protecting low carbon steels from hot corrosion, with or without corrosion medium.
5. The results showed that, the corrosion rate increases with increasing temperatures, but the corrosion rate was very low for samples with coating, compared to samples without coating.
6. The results showed that the activation energy for the samples without coating and without ash was high and the activation energy decreased with ash.

### 4.10 Future Work

Through the results obtained from this study, the following future studies were suggested:

1. Preparation of alumina nanoparticles by other methods such as hydrothermal method.
2. Fabrication of composite nanoparticles such as ( $\alpha\text{-Al}_2\text{O}_3\text{+TiO}_2$ ), ( $\alpha\text{-Al}_2\text{O}_3\text{+ZrO}_2$ ) and ( $\alpha\text{-Al}_2\text{O}_3\text{+YSZ}$ ), to coating the low carbon steel and studying the hot corrosion rates.
3. Study of the effect of high temperatures on low carbon steel coatings using other methods such as: Flame Spraying, High Velocity Oxy-fuel Spraying (HVOF) and Vacuum Plasma Spraying (VPS)
4. Study of corrosion rates at different times and for different temperatures.



# References

## References

---

### References

- [1] M. Arivarasu, M. Manikandan, K. Gokulkumar, V. Rajkumar, K. D. Ramkumar and N. Arivazhagan, "High temperature studies on welded joint in molten salt power plant environments", *International Journal of ChemTech Research*, Vol. 6, No.1, pp. 409-415, 2014.
- [2] G. Evans, D. R. Mumm, J. W. Hutchinson, G. H. Meier and F. S. Pettit, "Mechanisms Controlling the Durability of Thermal Barrier Coatings", *Progress in Materials Science*, Vol. 46, No. 5, pp. 505-553, 2001.
- [3] M. I. Sahri, N. K. Othman, Z. Samsu, and A. R. Daud, "Investigation of High Temperature Corrosion Behavior on 304L Austenite Stainless Steel in Corrosive Environments", *AIP Conf. Proc*, Vol. 1614, pp. 152-157, 2014.
- [4] V. K. Gouda, M. M. Nassrallah, S. M. Sayed and N. H. Gerges, "Failure of Boiler Tubes in Power Plants", *British Corrosion Journal*, Vol. 16, No. 1, 1981.
- [5] Y. Zeng, S. W. Lee and C. X. Ding, "Plasma Spray Coatings in Different Nanosize Alumina", *Materials Letters*, Vol. 57, pp. 495 – 501, 2002.
- [6] L. Shaw, D. Goberman and R. Ren, "The Dependency of Microstructure and Properties of Nanostructured Coatings on Plasma Spray Conditions", *Surface and Coatings Technology*, Vol. 130, pp. 1– 8, 2000.
- [7] R. Gadow, F. Kern and Killinger. A, "Manufacturing Technologies for Nanocomposite Ceramic Structural Materials and Coatings Materials" *Science and Engineering*, Vol. 148, pp. 58 – 64. 2008.
- [8] I. Pranevičius, L. L. Valatkevičius, P. Valinčius and V. Montassier, "Catalytic Behavior of Plasma-sprayed Al-Al<sub>2</sub>O<sub>3</sub> Coatings Doped with Metal Oxides", *Surface and Coatings Technology*, Vol. 125, pp. 392 – 395, 2000.
- [9] M. Al Qubeissi, S.S. Sazhin, J. Turner, S. Begg, C. Crua and M.R. Heikal, "Modelling of gasoline fuel droplets heating and evaporation Fuel", Vol. 159, No.373, 2015.
- [10] M. A. Bash, "Optimizing, phase transformation and hot corrosion resistance of laser sealing plasma sprayed ceria stabilized zirconia thermal barrier coatings", PhD Thesis, Department of Production Engineering and Metallurgy, University of Technology, Baghdad, Iraq, 2017.

## References

---

- [11] L. Marcinauskas, "Deposition of Alumina Coatings from Nanopowders by Plasma Spraying", *Materials Science*, V. 16, No. 1, pp. 47–51, 2010.
- [12] D. Landolt, "Corrosion and Surface Chemistry of metals", CRC Press, 1<sup>st</sup> ed. Italy, 2007.
- [13] E. Bardal, "Corrosion and Protection- Engineering Materials and Processes", Springer- Verlag London limited, 2004.
- [14] R. Thiab, "Corrosion and Corrosion Inhibition of Carbon steel using Extracts of Natural Materials" M.Sc. Thesis, Department of production Engineering and Metallurgy, University of Technology, 2011.
- [15] R. G. Kelly, J. R. Scully, D. W. Shoesmith and R. G. Buchheit, "Electrochemical techniques in corrosion science and engineering", Marcel Dekker, 1<sup>st</sup> ed, 2003
- [16] D. Talbot and J. Talbot, "Corrosion Science and Technology", 1<sup>st</sup> ed, CRC Press, 1998.
- [17] A. P. Schweitzer "Corrosion Engineering Handbook and Fundamentals of Metallic corrosion Atmospheric and Media corrosion of metals", Taylor & Francis Group, 2<sup>nd</sup> ed, 2007.
- [18] A. Etor, M.SC. Thesis, "Electrochemical Measurement of Crevice corrosion of Type AISI 304 Stainless Steel", University of Saskatchewan, Saskatoon, 2009.
- [19] Z. Ahmad, "Principles of Corrosion Engineering and Corrosion Control", Butterworth-Heinemann is an imprint of Elsevier, 2006.
- [20] K. F. Al-Sultani, "A pilot System for Evaluation of Hot Ash Corrosion Inhibition in Power Generation Boilers", Ph.D. Thesis The Technology University, 2003.
- [21] M. Spiegel, "Influence of gas phase composition on the Hot Corrosion of steels and nickel-based alloys beneath a (Ca-Na-K)-sulfate mixture containing  $\text{PbSO}_4$  and  $\text{ZnSO}_4$ ", *Materials and Corrosion*, Vol. 51, pp. 303-312, 2000.
- [22] S. Kamala, R. Jayaganthan, S. Prakash, S. Kumar, "Hot corrosion behavior of detonation gun sprayed  $\text{Cr}_3\text{C}_2$ -NiCr coatings on Ni and Fe-based super alloys in  $\text{Na}_2\text{SO}_4$ -60%  $\text{V}_2\text{O}_5$  environment at 900 °C", *Journal of Alloys and Compounds*, Vol. 463, pp. 358-372, 2008.

## References

---

- [23] P. Bansal, N. P. Padture and A. Vasiliev, "Improved interfacial properties of Al<sub>2</sub>O<sub>3</sub>-13wt%TiO<sub>2</sub> plasma sprayed coatings derived from nanocrystalline powders", *Acta Materialia*, Vol.51, pp. 2959-2970, 2003.
- [24] Y.Z. Liu and X.B. Hu, "Segregation and microstructural evolution at interfaces of atmospheric plasma sprayed thermal barrier coatings during thermal cycling ", *Journal of Alloys and Compounds*, Vol. 819, No. 5, pp. 1-13, 2020.
- [25] U. Schulz , B. Saruhan, K. Fritscher and C. Leyens, "Review on Advanced EB-PVD Ceramic Topcoats for TBC Applications", *International Journal of Applied Ceramic Technology*, Vol. 1, No. 4, pp. 302- 315, 2004.
- [26] X. Q. Cao, R. Vassenb and D. Stoever, "Ceramic materials for thermal barrier coatings", *Journal of the European Ceramic Society*, Vol. 24, pp. 1- 10, 2004.
- [27] R. H Cayton and R. W Brotzman, "Nanocomposite Coatings Applications and Properties", *Materials Research Society*, Vol. 703 , 2002.
- [28] D. R. Baer, P. E. Burrows and A. A. El-Azab, "Enhancing Coating Functionality Using Nanoscience and Nanotechnology", *Progress in Organic Coatings*, Vol. 47, pp. 342–356, 2003.
- [29] W.R. Chen, X. Wu, D. Dudzinski and P.C. Patnaik, "Modification of oxide layer in plasma-sprayed thermal barrier coatings", *Surface and Coatings Technology*, Vol. 200, pp. 5863–5868, 2006.
- [30] E. Sadeghi, N. Markocsan and S. Joshi, "Advances in Corrosion-Resistant Thermal Spray Coatings for Renewable Energy Power Plants. Part I: Effect of Composition and Microstructure", *Journal of Thermal Spray Technology*, Vol. 28, pp. 1749- 1988, 2019.
- [31] S. B. Kalsi, T. S. Sidhu and H. Singh, "Chlorine based hot corrosion study of cold sprayed NiCrAlY coating", *Surface Engineering*, Vol. 30, No. 6, pp. 422-431, 2014.
- [32] T.S Sidhu, R.D. Agrawal and S. Prakash, "Hot corrosion of some superalloys and role of high-velocity oxy-fuel spray coatings -a review", *Surface & Coatings Technology*, Vol. 198, pp. 441-446, 2005.
- [33] J.M. Shockley, S. Descartes, P. Vo, E. Irissou and R.R. Chromik, "The influence of Al<sub>2</sub>O<sub>3</sub> particle morphology on the coating formation and dry sliding wear behavior of cold sprayed Al-Al<sub>2</sub>O<sub>3</sub> composites", *Surface and Coatings Technology*, Vol. 270, pp. 324-333, 2015.

## References

---

- [34] V. V Sobolev, J. M. Guilemany and J. Nutting, " High Velocity Oxy-Fuel Spraying Theory, Structure-Property Relationships and Application", 1<sup>st</sup> ed, The Institute of Materials, Minerals and Mining, 2004.
- [35] S. Kuroda, J. Kawakita, M. Watanabe and H. Katanoda, "Warm spraying -a novel coating process based on high-velocity impact of solid particles" , Vol. 9, pp. 1-17. 2008.
- [36] H. S. Kim, B. R. Kang and S. M. Choi, "Microstructure and Mechanical Properties of Vacuum Plasma Sprayed HfC, TiC, and HfC / TiC Ultra-High-Temperature Ceramic Coatings", Materials, Vol. 13, pp. 1-8, 2019.
- [37] S. V. Shinde, E. J. Gildersleeve , C. A. Johnson and S. Sampath, "Segmentation crack formation dynamics during air plasma spraying of zirconia", Acta Materialia, V. 183, pp. 196-206, 2020.
- [38] T. Pradeep , " Nano The Essentials, Understanding Nanoscience and Nanotechnology", Tata McGraw-Hill Publishing Company Limited New Delhi, 2007.
- [39] T. Ihn, "Semiconductors Nanostructures", Oxford University Press, New York, 2010.
- [40] J. Jeevanandam, A. Barhoum, Y. S. Chan, A. Dufresne and M. K. Danquah, "Review on nanoparticles and nanostructured materials: history, sources, toxicity and regulations", Beilstein J. Nanotechnology, Vol. 9, pp. 1050-1074, 2018.
- [41] T. Kusamoto, H. Nishihara, " Zero-, one- and two-dimensional bis (dithiolato) metal complexes with unique physical and chemical properties" , Coordination Chemistry Reviews, Vol. 380, pp. 419-430, 2019.
- [42] A. Alagarasi, " Introduction to nanoscience and nanomaterials, chapter.1", <https://www.researchgate.net/publication/259118068>, 2011.
- [43] T. Ihn, "Semiconductors Nanostructures", World Scientific, 2010.
- [44] J. Karthikeyan, C.C. Berndt, J. Tikkanen, S. Reddy and H. Herman, "Plasma spray synthesis of nanomaterial powders and deposits", Materials Science and Engineering, Vol. 238, pp. 275-286. 1997.
- [45] J. A. Rodríguez, and M. Fernández-García, "Synthesis, properties, and applications of oxide nanomaterials", John Wiley and Sons, Inc, 2005.

## References

---

- [46] J. K. Patra and K. H. Baek, "Green Nanobiotechnology: Factors Affecting Synthesis and Characterization Techniques", *Journal of Nanomaterials*, Vol. 6, pp. 1-12, 2014.
- [47] B. C. Dave, X. Hu and Y. Devaraj, "Sol-Gel-Derived Corrosion-Protection Coatings", *Journal of Sol-Gel Science and Technology*, Vol.32, PP. 143-147, 2004.
- [48] S. Tabesh, F. Davar and M. R. Loghman-Estarki, "Preparation of  $\gamma$ - $\text{Al}_2\text{O}_3$  nanoparticles using modified sol-gel method and its use for the adsorption of lead and cadmium ions", *Journal of Alloys and Compounds*, vol. 730, PP. 441-491, 2018.
- [49] Qi Zhang, D. Sando and V. Nagarajan, "Chemical Route derived Bismuth Ferrite Thin films and Nanomaterials", *Journal of Materials Chemistry C*, PP. 1-88, 2016.
- [50] A. V.Gómez, J. Molina, S. Pradas, M. J. Tendero, and F. Bosch, "Microencapsulation of cerium and its application in sol-gel coatings for the corrosion protection of aluminum alloy AA2024", *Journal of Sol-Gel Science and Technology*, Vol. 93, PP. 36-51, 2020.
- [51] K. Tadanaga, "Preparation and Application of Alumina- and Titaniananocrystals- Dispersed Thin Films via Sol-Gel Process with Hot Water Treatment", Springer Science, *Sol-Gel Sci Techn*, Vol. 40, PP. 281-285, 2006.
- [52] J.D Wright and N. Sommerdijk, "Sol-gel materials: chemistry and applications", *Advanced chemistry texts*, Vol. 4, 2001.
- [53] M. I. Sahri, N. K. Othman, Z. Samsu and A. R. Daud, "Investigation of High Temperature Corrosion Behavior on 304L Austenite Stainless Steel in Corrosive Environments", *AIP Conference Proceedings* Vol. 1614, pp. 152-157, 2014.
- [54] N. Arivazhagan, S. Singh, S. Prakash and G. M. Reddy, "An assessment of hardness, impact strength, and hot corrosion behaviour of friction-welded dissimilar weldments between AISI 4140 and AISI 304", *The International Journal of Advanced Manufacturing Technology*, Vol. 39, pp. 679-689, 2014.
- [55] Q. Hu, G. Zhang, Y. Qiu and X. Guo, "The crevice corrosion behaviour of stainless steel in sodium chloride solution", *Corrosion Science*, Vol. 53, pp. 4065-4072, 2011.
- [56] G.X. Shen, Y.C. Chen and C.J. Lin, "Corrosion protection of 316L stainless steel by a  $\text{TiO}_2$  nanoparticle coating prepared by sol-gel method", *Thin Solid Films*, Vol. 489, pp. 130 - 136, 2005.

## References

---

- [57] R. L. Klueh and A.T. Nelson, "Ferritic/martensitic steels for next-generation reactors", *Journal of Nuclear Materials*, Vol. 371, pp. 37–52, 2007.
- [58] T. Daisuke, and T. Nobuhiro, "Effect of strain rate on hydrogen embrittlement in low-carbon martensitic steel", *International Journal of Hydrogen Energy*, Vol. 42, pp. 3371-3379, 2017.
- [59] R. Pampuch, "An Introduction to Ceramics ", Springer International Publishing, Vol. 95, 2014.
- [60] M. Kaur, S. Ishii, Satoshi, S.L. Shinde, Nagao and T. Tadaaki, "All-Ceramic Solar-Driven Water Purifier Based on Anodized Aluminum Oxide and Plasmonic Titanium Nitride", *Advanced Sustainable Systems* , pp. 1-8, 2018.
- [61] V. D. Kingery, H. K. Bowen and D. R. Uhlmann, "Introduction to Ceramics", 2<sup>nd</sup> ed, Wiley Series on the Science and Technology of Materials, 1975.
- [62] R. Septawendar, Suhandi and F. Edwin, "Nanocrystalline  $\alpha$ -Al<sub>2</sub>O<sub>3</sub> powder preparation with sucrose as a template through a chemical route", *Journal of Ceramic Processing Research*, Vol. 12, No. 4, pp. 365-370, 2011.
- [63] M. H. Zare , N. Hajilary and M. Rezakazemi, "Microstructural modifications of polyethylene glycol powder binder in the processing of sintered alpha alumina under different conditions of preparation", *Materials Science for Energy Technologies*, Vol. 2, pp. 89-95, 2019.
- [64] H. H. Mert and M. S. Mert, "Preparation and characterization of encapsulated phase change materials in presence of gamma alumina for thermal energy storage applications", *Thermochimica Acta*, Vol. 681, pp. 1-10, 2019.
- [65] S. N. Grigoriev, S. V. Fedorov , and K. Hamdy, "Materials, properties, manufacturing methods and cutting performance of innovative ceramic cutting tools a review", *Manufacturing Review*, Vol. 6, pp. 1-27, 2019.
- [66] Z. Yin , C. Huang , J. Yuan , B. Zou , H. Liu and H. Zhu "Cutting performance and life prediction of an Al<sub>2</sub>O<sub>3</sub>/TiC micro–nano-composite ceramic tool when machining austenitic stainless steel", *Ceramics International*, Vol. 41 , pp. 7059-7065, 2015.
- [67] S. Kalsi, T.S.Sidhu and H. Singh, "Characterisation of NiCrAlY Coatings on Ni- and Fe- Based Superalloys By the Cold Spray Process", *Journal on Material Science*, Vol. 1, pp. 19-25, 2013.

## References

---

- [68] K. A. Habib, M. S. Damra, J. J. Carpio, I. Cervera, and J. J. Saura, "Performance of NiCrAlY Coatings Deposited by Oxyfuel Thermal Spraying in High Temperature Chlorine Environment", *Journal of Materials Engineering and Performance* Vol. 23, pp. 3511-3522, 2014.
- [69] L. Bo, M. Shengqiang, G. Yimin, L. Cong, G. Hongjian, Z. Qiaoling, K. Yunchuan and J. Junhong, " Mechanical, Tribological, and Oxidation Resistance Properties of NiCrAlY Coating by Atmosphere Plasma Spraying", *Frontiers in Materials*, Vol. 6, pp. 1-6, 2019.
- [70] G. Bolelli, A. Candeli, L. Lusvarghi, A. Ravaux, K. Cazes, A. Denoirjean, S. Valette, C. Chazelas, E. Meillot and L. Bianchi, " Tribology of NiCrAlY+Al<sub>2</sub>O<sub>3</sub> composite coatings by plasma spraying with hybrid feeding of dry powder suspension", *Wear* , Vol. 344-345, pp. 69-85, 2015.
- [71] J. Gao, Y. He and D. Wang, "Fabrication and high temperature oxidation resistance of ZrO<sub>2</sub>/Al<sub>2</sub>O<sub>3</sub> micro-laminated coatings on stainless steel", *Materials Chemistry and Physics*, Vol. 123, PP. 731–736, 2010.
- [72] F. Mirjalili, H. Mohamad and L. Chuah, " Preparation of nano- scale α-Al<sub>2</sub>O<sub>3</sub> powder by the sol-gel method" , *Ceramics – Silikáty*, Vol. 55, No. 4, pp. 378-383, 2011.
- [73] E. Marin, A. Lanzutti, L. Guzman and L. Fedrizzi, " Corrosion protection of AISI 316 stainless steel by ALD alumina/titania nanometric coatings", *J. Coat. Technol. Res*, Vol. 8, No. 5, pp. 655-659, 2011.
- [74] M. Daroonparvar, M. A. Mat Yajid, N. M. Yusof, H. R. Bakhsheshi-Rad, M. S. Hussain, and E. Hamzah, "Evaluation of Normal and Nanolayer Composite Thermal Barrier Coatings in Fused Vanadate-Sulfate Salts at 1000 °C", *Advances in Materials Science and Engineering*, Vol. 2013, pp. 1-13, 2013.
- [75] M. Nejati, M. R. Rahimipour and I. Mobasherpour, "Evaluation of hot corrosion behavior of CSZ, CSZ/micro Al<sub>2</sub>O<sub>3</sub> and CSZ/nano Al<sub>2</sub>O<sub>3</sub> plasma sprayed thermal barrier coatings", *Ceramics International*, Vol. 40, pp. 4579-4590, 2014.

## References

---

- [76] A. Keyvani, M. Saremi, M. H. Sohi, Z. Valefi, M. Yeganeh and A. Kobayashi, "Microstructural stability of nanostructured YSZ–alumina composite TB C compared to conventional YSZ coatings by means of oxidation and hot corrosion tests", *Journal of Alloys and Compounds*, Vol. 600 , pp. 151-158, 2014.
- [77] P. Doodman, M. A. Faghihi-Sani, N. Barati and A. Afshar, "Alumina nanostructured coating for corrosion protection of 316L stainless steel", *International Journal of Nano Dimension*, Vol. 5, No. 1, pp. 27-33, 2014.
- [78] A. Abdullah Khadom, A. A. Fadhil, A. A. Karim and H. liw, "Effect of hot corrosion on boiler pipes in north bagdad electric power plant station ", *Diyala Journal of Engineering Sciences*, Vol. 8, No. 4, pp776-784, 2015.
- [79] A. Ismardi, O. M. Rosadi, M. R. Kirom and D. G. Syarif, "Synthesis and thermal characterization of Al<sub>2</sub>O<sub>3</sub> nanoparticles", *Journal of Physics: Conference Series*, Vol. 776, pp. 1-6, 2015.
- [80] M. Farahmandjou and N. Golabiyani, " Synthesis and characterization of Alumina (Al<sub>2</sub>O<sub>3</sub>) nanoparticles prepared by simple sol-gel method", *International Journal of Bio-Inorganic Hybrid Nanomaterials*, Vol. 5, No. 1, pp. 37-77, 2016.
- [81] G. Rakesh, S. B. Singh and C. Vikas, " Characterization of plasma-sprayed carbon nanotube (CNT)-reinforced alumina coatings on ASME-SA213-T11 boiler tube steel", *The International Journal of Advanced Manufacturing Technology*, Vol. 92, pp. 9-12, 2017.
- [82] M. Karabaşa, E. Balb and Y. Taptik, "Hot Corrosion Behaviour of Plasma Sprayed Alumina + YSZ Particle Composite Coating", *Protection of Metals and Physical Chemistry of Surfaces*, Vol. 53, No. 5, pp. 859–863, 2017.
- [83] A.K. Rajeh, Z. N.. Al- Mohsen and K. Fenthel, "Inhibition Vanadic Corrosion by Using Magnesium Oxide in Oil Fired Boilers", *The Iraqi Journal For Mechanical And Material Engineering*, Special Issue (C), pp. 512-525, 2016.
- [84] F. Y. Najy, K. F. Al-Sultani and J. M. Al. Murshdy, "Study Addition Double Inhibitor Consist of MgO And SiO<sub>2</sub> to Residual Oil to Prevent Hot Corrosion of Stainless Steel (304 L) of Boilers Pipes in Power Generation Station". *Advances in Natural and Applied Sciences*, Vol. 11, No. 2, pp. 57- 67, 2017.

## References

---

- [85] M. J. Kadhim, M. H. Hafiz and M. A. Bash, "Hot corrosion of Ceria-Yttria stabilized Zirconia plasma sprayed thermal barrier coating by Eutectic Vanadium Pentoxide-Sodium Sulfate", *The Iraqi Journal For Mechanical And Material Engineering*, Vol. 18, No. 1, 2018 .
- [86] M. A. Hamood, R. H. Mahmood and E. E. Kidder, " The Use of  $Dy_2O_3$  as Thermal Barrier in Aluminide Coating on One Type of Stainless Steel", *Journal of Science Rafidain*, Vol. 27, pp 125-134, 2018.
- [87] F. B. Mainier and A. S. de Oliveira, " Hot corrosion Evaluation of Carbon Steel caused by Mixtures of Vanadium Oxide and Sodium Sulfate Simulating Ashes of Fuel Oils", *International Journal of Advanced Engineering Research and Science*, Vol. 6, No.1, pp . 147-150, 2019.
- [88] I. Singh , K. Goyal and R. Goyal, "Evaluations of Hot Corrosion Behavior of  $Al_2O_3$  Thermal Spray Coatings with  $ZrO_2$  Reinforcements on T-91 Steel", *Universal Journal of Mechanical Engineering* , Vol. 7, No. 4, pp. 224-230, 2019.
- [89] A. S. Praveen and A. Arjunan, " Effect of nano- $Al_2O_3$  addition on the microstructure and erosion wear of HVOF sprayed NiCrSiB coatings", *Mater. Res. Express*, Vol. 7, pp. 1-14, 2020.
- [90] G. Singh, K. Goyal and R. Goyal , "Comparative study of hot corrosion behavior of thermal sprayed alumina and titanium oxide reinforced alumina coatings on boiler steel", *Materials Research Express*, Vol. 7, pp.1-12, 2020.
- [91] O. J. Yopez, "On the Mechanism of High Temperature Corrosion On the Mechanism of High Temperature Corrosion", 2018.
- [92] C. Wang, S. Ai, and D. Fang, "Effect of Oxidation-Induced Material Parameter Variation on the High Temperature Oxidation Behavior of Nickel," *Acta Mech. Solida Sin*, Vol. 29, No. 4, pp. 337–344, 2016.
- [93] X. Dong, X. Feng, and K. C. Hwang, "Stress-diffusion interaction during oxidation at high temperature", *Chemical Physics Letters*, Vol. 614, pp. 95–98, 2014.
- [94] J. Barroso, F. Barreras, and J. Ballester, "Behavior of a high-capacity steam boiler using heavy fuel oil: Part I. High-temperature corrosion," *Fuel Process. Technol.*, Vol. 86, No. 2, pp. 89–105, 2004.
- [95] E. Rocca, P. Steinmetz, and M. Moliere, "Revisiting the inhibition of vanadium-induced hot corrosion in gas turbines", *J. Eng. Gas Turbines Power*, Vol. 125, No. 3, pp. 664–669, 2003.

## References

---

- [96] H. Singh, D. Puri, and S. Prakash, "An overview of Na<sub>2</sub>SO<sub>4</sub> AND/OR V<sub>2</sub>O<sub>5</sub> induced hot corrosion of Fe- and Ni-Based superalloys", *Rev. Adv. Mater. Sci*, Vol. 16, pp. 27–50, 2007.
- [97] A. A. Khadom, A. S. Yaro, A. A. H. Kadum, A. S. Altaie, and A. Y. Musa, "The effect of temperature and acid concentration on corrosion of low carbon steel in hydrochloric acid media," *American Journal of Applied Sciences*, Vol. 6, No. 7, pp. 1403–1409, 2009.
- [98] D. A. Pantony and K. I. Vasu, "Studies in the corrosion of metals under melts-III" ,*J. Inorg. Nucl. Chem*, Vol. 30, No. 3, pp. 755–779, 1968.
- [99] R. A. Rapp, "Hot corrosion of materials: A fluxing mechanism" , *Corrosion Science*, Vol. 44, No. 2, pp. 209–221, 2002.
- [100] F. Pettit, "Hot corrosion of metals and alloys", *Oxidation of Metals*, Vol. 76, , pp. 1–21, 2011.
- [101] J. De Deus and R. S. Pinheiro, "Fouling of Heat Transfer Surfaces", *Heat Exch Sourceb*, pp. 721–743, 1986.
- [102] D. R. Mumm and G. A. Evans, "Mechanisms controlling the performance and durability of thermal barrier coatings", *Key Engineering Materials*, Vol. 197, pp. 199–230, 2001.
- [103] A. C. Fox and T. W. Clyne, "Oxygen transport by gas permeation through the zirconia layer in plasma sprayed thermal barrier coatings", *Surface and Coatings Technology*, Vol. 184, pp. 311–321, 2004.
- [104] R. A. Wessel, N. Mahinpey, D. Kuhn, and H. Tran, "Effect of particle composition on carryover deposition in recovery boilers", *TAPPI Fall Tech. Conf. Trade Fair*, No. January 2002, pp. 315–328, 2002.
- [105] U. Kleinhans, C. Wieland, F. J. Frandsen, and H. Spliethoff, "Ash formation and deposition in coal and biomass fired combustion systems: Progress and challenges in the field of ash particle sticking and rebound behavior", *Progress in Energy and Combustion Science*, Vol. 68, pp. 65–168, 2018.
- [106] W. R. Chen, X. Wu, B. R. Marple, and P. C. Patnaik, "Oxidation and crack nucleation/growth in an air-plasma-sprayed thermal barrier coating with NiCrAlY bond coat," *Surface Coatings Technolgy* , Vol. 197, No. 1, pp. 109–115, 2005.
- [107] A. Abdul-Aziz, "Durability modeling review of thermal- and environmental-barrier-coated fiber-reinforced ceramic matrix composites part I", *Materials*, Vol. 10, No. 7, pp.1-6, 2018.

## References

---

- [108] L. Y. Lim and S. A. Meguid, "Temperature dependent dynamic growth of thermally grown oxide in thermal barrier coatings", *Materials and Design*, Vol. 164, pp. 1-27, 2019.
- [109] Teknos Oy, "Handbook for Corrosion Protection," 2013.
- [110] Y. Qian, Y. Li, S. Jungwirth, N. Seely, Y. Fang, and X. Shi, "The Application of Anti-Corrosion Coating for Preserving the Value of Equipment Asset in Chloride-Laden Environments: A Review", *Int. J. Electrochem. Sci*, Vol. 10, pp. 10756–10780, 2015.
- [111] W. Aperador, J. Bautista-Ruiz, and E. Delgado, "Hot corrosion resistance of Al<sub>2</sub>O<sub>3</sub> coating produced by thermal spray", *Int. J. Electrochem. Sci*, Vol. 11, No. 11, pp. 9424–9437, 2016.
- [112] E. Zhang et al., "Numerical simulation for erosion effects of three-phase flow containing sulfur particles on elbows in high sour gas fields", *Petroleum*, Vol. 4, No. 2, pp. 158–167, 2018.
- [113] B. Veith, F. Werner, D. Zielke, R. Brendel, and J. Schmidt, "Comparison of the thermal stability of single Al<sub>2</sub>O<sub>3</sub> layers and Al<sub>2</sub>O<sub>3</sub>/SiN<sub>x</sub> stacks for the surface passivation of silicon", *Energy Procedia*, Vol. 8, pp. 307–312, 2011.
- [114] J. Musil and M. Jirout, "Toughness of hard nanostructured ceramic thin films", *Surface & Coatings Technology*, Vol. 201, pp. 5148–5152, 2007.
- [115] A. Górala, T. Czeppea and K. Berent, "Oxidation behaviour of thin Ni/Al<sub>2</sub>O<sub>3</sub> nanocomposite coatings electrodeposited on steel substrate", *Surface & Coatings Technology*, Vol. 369, pp. 95–104, 2019.
- [116] L. Pawlowski, "The Science and Engineering of Thermal Spray Coatings", 2<sup>nd</sup> ed., John Wiley and Sons, 2008.
- [117] P. Fauchais, and A. Vardelle, "Thermal Spray Coatings", *Wiley Encyclopedia of Electrical and Electronics Engineering*.
- [118] A. K. Farman, "A study of the physical properties of Ceramite coatings produced from (Ni-Al + Al<sub>2</sub>O<sub>3</sub>) by thermal spray method", PhD thesis, Physics Department - College of Science, 2005.
- [119] G. Mehboob, M. Jun Liu, T. Xu<sup>1</sup>, S. Hussain, G. Mehboob and A. Tahir, "A review on failure mechanism of thermal barrier coatings and strategies to extend their lifetime", *Ceramics International*, Vol. 46, pp. 8497–8521, 2019.

## References

---

- [120] D. H. James, " A review of experimental findings in surface preparation for thermal spraying", *Journal of Mechanical Working Technology*, Vol. 10, pp. 221–232, 1984.
- [121] J. Day, X. Huang, N. L. Richards, " Examination of a Grit Blasting Process for Thermal Spraying Using Statistical Methods", *Journal of Thermal Spray Technology*, Vol. 14, No. 4, pp. 471-47, 2005.
- [122] H. Lipson, " The Study of Metals and Alloys by X-ray Powder Diffraction Methods", *International Union of Crystallograph*, 1984.
- [123] S. A. Naayi, A. I. Hassan, and E. T. Salim, "FTIR and X-ray diffraction analysis of Al<sub>2</sub>O<sub>3</sub> nanostructured thin film prepared at low temperature using spray pyrolysis method", *International Journal of Nanoelectronics and Materials*, Vol. 11, pp. 1- 6, 2018.
- [124] S.R.Elliott, "Physics of amorphous materials", Wiley, 1990.
- [125] J. T. Richardson, R. M. Scates, and M. V. Twigg, "X-ray diffraction study of the hydrogen reduction of NiO/ $\alpha$ -Al<sub>2</sub>O<sub>3</sub> steam reforming catalysts," *Appl. Catal. A Gen.*, Vol. 267, pp. 35-46, 2004.
- [126] B. Joseph, P. K. Manoj, and V. K. Vaidyan, "Studies on preparation and characterization of indium doped zinc oxide films by chemical spray deposition", *Bull. Mater. Sci*, Vol. 28, No. 5, pp. 487-493, 2005.
- [127] Y. T. Prabhu, K. V. Rao, V. S. S. Kumar, and B. S. Kumari, "X-Ray Analysis by Williamson-Hall and Size-Strain Plot Methods of ZnO Nanoparticles with Fuel Variation", *World Journal of Nano Science and Engineering*, Vol. 4, pp. 21–28, 2014.
- [128] Z. T. Khodair, M. A. Al-Jubbori, A. M. Shano , F. I. Sharrad, " Study of Optical and Structural Properties of (NiO)<sub>1-x</sub>(CuO)<sub>x</sub> Nanostructures Thin Films", *Chemical Data Collections*, Vol. 28, pp. 1-7, 2020.
- [129] D. Stephens and W. J. Alford, "Dislocation Structures in Single-Crystal", 2000.
- [130] S. Kaneko, Y. Yamagami, H. Tochiara, and I. Hirasawa, "Effect of supersaturation on crystal size and number of crystals produced in antisolvent crystallization," *Journal of Chemical Engineering of Japan*, Vol. 35, No. 11, pp. 1219–1223, 2002.
- [131] M. E. Nielsen and M. R. Fisk, "Data report: specific surface area and physical properties of subsurface basalt samples from the east flank of Juan de Fuca Ridge", Vol. 301, 2008.

## References

---

- [132] J. Antony, J. Nutting, D. R. Baer, D. Meyer, A. Sharma, and Y. Qiang, "Size-dependent specific surface area of nanoporous film assembled by core-shell iron nanoclusters," *Journal of Nanomaterials.*, Vol. 2006, pp. 1–4, 2006.
- [133] W. Pabst and E. Gregorová, "Characterization of particles and particle systems", Pabst and Gregorova, 2007.
- [134] S. Bates, G. Zografi, D. Engers, K. Morris, K. Crowley, and A. Newman, "Analysis of amorphous and nanocrystalline solids from their X-ray diffraction patterns," *Pharmaceutical Research*, Vol. 23, No. 10, pp. 2333–2349, 2006.
- [135] K. Užarevi, V. Strukil, C. Mottillo, P. A. Julien, A. Puškari, T. Friscic, and I. Halasz, "Exploring the effect of temperature on a mechanochemical reaction by in situ synchrotron X-ray powder diffraction", *Crystal Growth and Design*, 2016. DOI: 10.1021/acs.cgd.6b00137.
- [136] J. Zhao, G. R. Hearne and M. Maaza, "Compressibility of nanostructured alumina phases determined from synchrotron x-ray diffraction studies at high pressure," *Jornale Apply Physics*, Vol. 90, No. 7, pp. 3280–3285, 2001.
- [137] R. R. Chaves and R. Caram, "Influence of the Nb and Al Content on the Mechanical Properties of Ti-Al-Nb Alloys", *Materials for Medical Engineering*, pp. 126–131, 2005.
- [138] W. Soboyejo, "Mechanical Properties of Engineered Materials", Marcel Dekker, 2003.
- [139] A. A. Nadia, S. I. Hussein, M. K. Jawad, and I. A. Al-Ajaj, "Effect of Al<sub>2</sub>O<sub>3</sub> and SiO<sub>2</sub> Nanoparticle on Wear, Hardness and Impact behavior of Epoxy composites", *Chemistry and Materials Research*, Vol. 7, No. 4, pp. 34–40, 2015.
- [140] B.W. McEnerney, G. Quinn, V.A. Greenhut, R.K. Sadangi, V. Shukla, B. Kear and D.E. Niesz, "Processing and Hardness of a Al<sub>2</sub>O<sub>3</sub> - MgAl<sub>2</sub>O<sub>4</sub> Nanocomposite", *Ceramic Engineering and Science Proceedings*, Vol. 25, No. 4, pp. 647-653, 2004.
- [141] J. Zygmuntowicz, A. Miazga, K. Konopka, and W. Kaszuwara, "Structural and mechanical properties of graded composite Al<sub>2</sub>O<sub>3</sub>/Ni obtained from slurry of different solid content", *Procedia Structural Integrity*, Vol. 1, pp. 305–312, 2016.

## References

---

- [142] A. Nastic, A. Merati, M. Bielawski, M. Bolduc, O. Fakolujo, and M. Nganbe, "Instrumented and Vickers Indentation for the Characterization of Stiffness, Hardness and Toughness of Zirconia Toughened  $\text{Al}_2\text{O}_3$  and SiC Armor", *Journal of Materials Science and Technology*, Vol. 31, No. 8, pp. 773–783, 2015.
- [143] H. Yang, W. Luan, and S. T. Tu, "Corrosion behavior and thermal conductivity of plasma sprayed AlN/ $\text{Al}_2\text{O}_3$  coating", *Materials Transactions*, Vol. 47, No. 7, pp. 1649–1653, 2006.
- [144] H. A. Kobulnicky, W. T. Chick, and M. S. Povich, "Demonstration of a Novel Method for Measuring Mass-loss Rates for Massive Stars," *The Astrophysical Journal*, Vol. 856, No. 1, p. 74, 2018.
- [145] N. Abu-warda, M. D. López, and M. V. Utrilla, "High temperature corrosion and wear behavior of HVOF-sprayed coating of  $\text{Al}_2\text{O}_3$ -NiAl on AISI304 stainless steel," *Surface and Coatings Technology*, Vol. 359, , pp. 35–46, 2019.
- [146] Q. C. Zhang, Y. Yin, and D. R. Mills, "High efficiency Mo- $\text{Al}_2\text{O}_3$  cermet selective surfaces for high-temperature application," *Solar Energy Materials and Solar Cells*, Vol. 40, No. 1, pp. 43–53, 1996.
- [147] L. Hanke, "Handbook of analytical methods for materials", *Materials Evaluation and Engineering*, pp. 1–50, 2001.
- [148] J. Pan, J. Öijerholm, A. B. Belonoshko, A. Rosengren, and C. Leygraf, "Self-diffusion activation energies in  $\alpha$ - $\text{Al}_2\text{O}_3$  below 1000°C - Measurements and molecular dynamics calculation," *Philosophical Magazine Letters*, Vol. 84, No. 12, pp. 781–789, 2004.
- [149] Ian W. M. Smith, "The temperature-dependence of elementary reaction rates: beyond Arrhenius", *Chemical Society Reviews*, vol. 37, pp. 812–826, 2008.
- [150] C. R. Che Hak, C. T. Foo, N. A. Othman, N. A. Shukri, M. S. Ripin, M. Y. Sulaiman and Y. Abdullah, "Field Emission Scanning Electron Microscope (FESEM) Facility in BTI, Inorganic, Organic, Physical and Analytical Chemistry, vol. 47, pp. 1–6, 2015.
- [151] R. Gauvin, "Field Emission Scanning Electron Microscopy- New Perspectives for Materials Characterization", *Springer Briefs in Applied Sciences and Technology*, 2017.
- [152] R. A. Fleck and B. M. Humbel, "Biological Field Emission Scanning Electron Microscopy", *Wiley Hoboken*, 2019.

## References

---

- [153] S. K. Sharma, "Handbook of Materials Characterization", Wiley Hoboken, Springer International, 1<sup>st</sup> ed., 2018.
- [154] B. Fultz and J. Howe, "Transmission Electron Microscopy and Diffractometry of Materials", Springer-Verlag Berlin Heidelberg, 4 ed, 2013.
- [154] J. W. Lee, S. K. Han, S. K. Hong, J. Y. Lee, and T. Yao, "Characterization of microstructure and defects in epitaxial ZnO (11 $\bar{2}$ 0) films on Al<sub>2</sub>O<sub>3</sub> (1 $\bar{1}$ 02) substrates by transmission electron microscopy," Journal of Crystal Growth, Vol. 310, No. 18, pp. 4102–4109, 2008.
- [156] B. Prabhu, C. Suryanarayana, L. An, and R. Vaidyanathan, "Synthesis and characterization of high volume fraction Al-Al<sub>2</sub>O<sub>3</sub> nanocomposite powders by high-energy milling," Materials Science and Engineering, Vol. 425, , pp. 192–200, 2006.
- [157] M. H. Bocanegra-Bernal, A. Garcia-Reyes, C. Dominguez-Rios, A. Reyes-Rojas, A. Aguilar-Elguezabal, and J. Echeberria, "Towards improving low-temperature degradation of zirconia/alumina ceramics via in-situ formation of an Al<sub>2</sub>O<sub>3</sub> functional surface layer through sintering in the presence of graphite powder," Journal of Alloys and Compounds, Vol. 818, pp. 1-8, 2020.
- [158] G. Busch, "Lectures on Solid State Physics", International Series in Natural Philosophy, 1<sup>st</sup> ed, 1976.
- [159] K. P. Sreekumar, Karthikeyan,P.V. Ananthapadmanabhan N. Venkatramani and U.K. Chatterjee, "Plasma spray technology and process parameters and applications", Materials Science, 1991.
- [160] R. B. Heimann, "Plasma- Spray Coating Principles and Applications", John Wiley & Sons, 2nd ed., 1996.
- [161] S. D. Anggraeni and F. Kurniawan, "Synthesis of Aluminium Nanoparticles Using Electrochemical Method", Journal of Physics: Conference Series, Vol. 1445, pp. 1-6, 2020.
- [162] R. Rogojan, E. Andronescu and C. D. Ghitulica, " synthesis and characterization of alumina nano-powder by Sol-Gel method", Chemistry and Materials Science, vol. 73, pp. 67-76, 2011.
- [163] V.D. Mote , Y Purushotham and B. N Dole, "Williamson-Hall analysis in estimation of lattice strain in nanometer-sized ZnO particles", Journal of Theoretical and Applied Physics, Vol. 6, p p. 1-8, 2012.

## References

---

- [164] H. Li, Z. Ke, J. Li, L. Xue, Y. Yan, " An effective low-temperature strategy for sealing plasma sprayed  $\text{Al}_2\text{O}_3$ - based coatings", *Journal of the European Ceramic Society*, Vol. 38, No. 4, pp. 1871-1877, 2018.
- [165] L. Lu, P. Sanxu, L. Yuhang, Z. Libin, M. Ji and L. Jiangong, " High-purity disperse  $\alpha$  - $\text{Al}_2\text{O}_3$  nanoparticles synthesized by highenergy ball milling", *Advanced Powder Technology*, Vol. 29, No.9, pp. 2194–2203, 2018.
- [166] B. Li, S. Ma, Y. Gao, C. Li, H. Guo, Q. Zheng, Y. Kang and J. Jia, "Mechanical, Tribological, and Oxidation Resistance Properties of NiCrAlY Coating by Atmospheric Plasma Spraying", *Frontiers in Materials*, Vol. 6, pp. 1–9, 2019.
- [167] F. Zhou, Z. Zhang, S. Liu, L. Wang, J. Jia, Y. Wang, X. Gong, J. Gou, C. Deng, M. Liu, " Effect of heat treatment and synergistic rare-earth modified NiCrAlY on bonding strength of nanostructured 8YSZ coatings", *Applied Surface Science*, Vol. 480, pp. 636 645, 2019.
- [168] R J Takahashi , J . Assis , F. Neto and D . Reis" Heat treatment for TGO growth on NiCrAlY for TBC application", *Materials Research Express*, Vol. 6, pp. 1–7, 2019.
- [169] M. S. Ahmadi , R. S. Razavi , Z. Valefi and H. Jamali, "Evaluatio of hot corrosion behavior of plasma sprayed and laser glaze YSZ– $\text{Al}_2\text{O}_3$  thermal barrier composite", *Optics and Laser Technology*, Vol. 111, pp. 687-695, 2019.
- [170] J.M. Shockley, S. Descartes, P. Vo, E. Irissou and R.R. Chromik, "The influence of  $\text{Al}_2\text{O}_3$  particle morphology on the coating formation and dry sliding wear behavior of cold sprayed Al- $\text{Al}_2\text{O}_3$  composites", *Surface and Coatings Technology*, Vol. 270, pp. 324-333, 2015.
- [171] M.I. Sahri, N.K. Othman, Z. Samsu and A.R. Daud, "Investigation of High Temperature Corrosion Behavior on 304L Austenite Stainless in Corrosive Environments", *AIP Conference Proceedings*, Vol. 1614, pp. 152-157, 2015.
- [172] V. Piriya Wong, V. Thongpoo, P. Asanithi, and P. Limsuwan, "Preparation and Characterization of Alumina Nanoparticles in Deionized Water Using Laser Ablation Technique", *Journal of Nanomaterials*, Vol. 2012, pp. 1-6, 2012.
- [173] S. Hannula, E. Turunen, J. Keskinen, T. Varis, T. Falt, T. Gustafson and R. Nowak, " Development of Nanostructured  $\text{Al}_2\text{O}_3$ - Ni HVOF Coatings", *Key Engineering Materials*, Vol. 317-318, pp. 539-544, 2006.

## References

---

- [174] R. Septawendar, A. Setiati and S. Sutardi, " Low-temperature calcination at 800°C of alumina–zirconia nanocomposites using sugar as a gelling agent", *Ceramics International*, Vol. 37, pp. 3747-3754, 2011.
- [175] J. Calderon, V.M. Bravo, R. Diaz and L. Gomez, " Effect of the NaVO<sub>3</sub>-V<sub>2</sub>O<sub>5</sub> Ratio on the High Temperature Corrosion of Chromium", *International Journal of Electrochemical Science*, Vol. 10, pp. 4928 - 4945, 2015.
- [176] Z. Chen , N.Q. Wu , J. Singh and S.X. Ma, " Effect of Al<sub>2</sub>O<sub>3</sub> overlay on hot-corrosion behavior of yttria-stabilized zirconia coating in molten sulfate-vanadate salt", *Thin Solid Films*, Vol. 443, pp. 46 - 52, 2003.
- [177] A. A. Khadom, H. Liu, A. A. Fadhil, A. A. Karim, "Retardation of High-Temperature Fuel Ash Corrosion of Fireside Boiler Tubes via Nanoparticles", *Oxidation of Metals*, Vol. 86, pp. 465-565, 2016.
- [178] A. Keyvani and M. Bahamirian, " Hot corrosion and mechanical properties of nanostructured Al<sub>2</sub>O<sub>3</sub>/CSZ composite TBCs", *Surface Engineering*, Vol. 86, pp. 553 - 565, 2016.
- [179] R. Horimizu, H. Inoue , I. Matsuyama and M. Katsumoto, "oxidation kinetics of acicular iron particles for magnetic recording media", *Journal of Magnetism and Magnetic Material*, Vol. 86, pp. 202 - 206, 1992.
- [180] H. T. Abuluwefa, " Kinetics of High Temperature Oxidation of High Carbon Steels in Multi-component Gases Approximating Industrial Steel Reheat Furnace Atmospheres", *International Multi Conference of Engineers and Computer Scientists*, Vol. II, pp. 1 - 5, 2012.

## الخلاصة

تم في هذه الدراسة تحضير حبيبات الألومينا النانوية ( $\alpha\text{-Al}_2\text{O}_3$ ) بنجاح بطريقة المحلول الغروي (Sol- Gel) في درجة حرارة الغرفة. أظهرت نتائج قياسات حيود الأشعة السينية (XRD) للحبيبات النانوية المحضرة أنها ذات تركيب متعددة التبلور ومن النوع السداسي. وتم حساب حجم البلوريات للحبيبات النانوية المحضرة باستخدام طريقة (Scherrer) وتحليل (Williamson Hall) وتبين أنها كانت بحدود (33.9 و 27.7 نانومتر) على التوالي. وكذلك أظهرت الصور للحبيبات النانوية أن لها أشكال بلورية بأحجام غير متجانسة وذات أشكال مختلفة ومنها كروية وشبه كروية، وأظهرت الصور كذلك أن معدل حجم الحبيبات النانوية كان تقريباً (29 نانومتر). أما صور TEM للحبيبات النانوية المحضرة بعد التحبيب قد بينت وجود تكتلات من الحبيبات النانوية، وشكلها داخل التكتلات شبه كروي كما تبين أن الحبيبات المحضرة تقع ضمن المقياس النانوي.

تم طلاء عينات الفولاذ منخفض الكربون بطبقتين، عبارة عن حبيبات (NiCrAlY) كطبقة رابطة والطبقة العليا هي جسيمات الألومينا النانوية ( $\alpha\text{-Al}_2\text{O}_3$ ) باستخدام تقنية الرش الحراري بالبلازما. كذلك تبين من صور (FESEM) لسطح العينات المطلية أنها كانت متجانسة ولا تحتوي على فجوات أو تشققات. هذا يثبت أن طلاء الرش بالبلازما يتمتع بجودة طلاء عالية. وان سمك طبقة المادة الرابطة حوالي ( $10 \pm 100$  مايكرومتر) اما سمك الطبقة العليا حوالي ( $5 \pm 37$  مايكرومتر).

تم دراسة وتحليل عينات الفولاذ منخفض الكربون غير المطلية والمطلية بعد اختبارها في درجات الحرارة (600، 700، 800 و 900 درجة مئوية) وبنوبت الزمن لمدة (20 ساعة) وذلك بغياب وجود وسط التآكل (الرماد) الذي يتكون من ( $57 \text{ wt}\% \text{ V}_2\text{O}_5$  and  $43 \text{ wt}\% \text{ Na}_2\text{SO}_4$ ).

أظهرت نتائج (XRD) للعينات المطلية وبدون رماد بعد اختبار الأكسدة أنه لا توجد قمم حيود لعناصر ومركبات أخرى، فقط لعنصري الاوكسجين والالمنيوم، ولكن في حالة وجود الرماد ظهرت قمم جديدة لمركبات أخرى مثل مركبات الفناديوم.

أظهرت صور (FESEM) للعينات المطلية وبدون رماد أنه لا يوجد تأثير لدرجة الحرارة على سطح العينات وأنه لم يلاحظ أي تشققات أو تآكل في طبقة الطلاء، وهذا يتفق مع الصور الفوتوغرافية للعينات بعد الاختبار انه لم يتغير لون العينات، اما في حالة العينات المطلية وبوجود الرماد، كشفت الصور عن تأثير كبير على سطح العينة بسبب تفاعل مركبات الرماد مع حبيبات الألمنيوم النانوية في درجات الحرارة العالية، ولوحظت تشققات

ومسامات نتيجة لانصهار مكونات الرماد وتفاعله مع طبقة الطلاء. كما أظهرت صور (FESEM cross-section) للعينات بعد الطلاء ووجود الرماد عند (600 و 900 درجة مئوية) عن وجود تشققات بين طبقة الترابط والركيزة.

أظهرت نتائج التآكل الساخن أن معدل التآكل يزداد مع زيادة درجة الحرارة ورماد الوقود. إذ وجد أن أدنى معدل للتآكل كان للعينات غير المطلية وبدون الرماد ، وأعلى معدل للتآكل للعينات غير المطلية هو وجود الرماد. تمت دراسة كفاءة الطلاء للعينات المطلية بالرماد أو بدونه ، حيث كانت تتراوح بين (44-84%). أما العينات المطلية بالرماد فتتراوح الكفاءة بين (84-88%). كما تم حساب طاقة التنشيط للعينات وكانت ذات قيمة عالية بدون طلاء ، وانخفضت طاقة التنشيط مع الرماد. أما بالنسبة للعينات المطلية وبدون وجود الرماد قد ازدادت طاقة التنشيط لكنها انخفضت بوجود الرماد.



جمهورية العراق  
وزارة التعليم العالي والبحث العلمي  
جامعة ديالى – كلية العلوم  
قسم الفيزياء



تأثير ترسيب الاغشية نانوية التركيب على المعادن  
للحماية من التآكل عند درجات الحرارة العالية

أطروحة مقدمة إلى  
مجلس كلية العلوم - جامعة ديالى  
وهي جزء من متطلبات نيل درجة دكتوراه فلسفة  
في علوم الفيزياء

تقدم بها

**عدنان علي محمد**

بكالوريوس علوم في الفيزياء 1993  
ماجستير علوم في الفيزياء 2016

إشراف

أ.د. انيس عبدالله كاظم

أ.د. زياد طارق خضير

1442 هـ

2020 م